Physical processes that determine the clustering of different types of galaxies on large scales

Mohammadreza Ayromlou

München 2021

Physical processes that determine the clustering of different types of galaxies on large scales

Mohammadreza Ayromlou

Dissertation
an der Fakultät für Physik
der Ludwig–Maximilians–Universität
München

vorgelegt von
Mohammadreza Ayromlou
aus dem Iran

München, den 15/12/2020

Contents

List of Figures

List of Tables

Zusammenfassung

In dieser Arbeit studieren wir die Rolle der Umgebung in der Galaxieentwicklung sowohl von theoretischer als auch beobachtungsgestützter Perspektive. Zuerst vergleichen wir Ergebnisse zwischen dem Münchner semi-analytischen Modell, L-GALAXIES, und den hydrodynamischen IllustrisTNG Simulationen – sowohl auf individueller als auch statistischer Ebene. Durch Anwendung von L-GALAXIES auf die Verschmelzungsbäume der dunklen Materie in IllustrisTNG identifizieren wir die gleichen Galaxien innerhalb der beiden Modelle. Wir finden, dass sowohl die stellare Massenfunktionen als auch die stellaren Massen einzelner Galaxien mit einer Genauigkeit besser als ~ 0.2 dex übereinstimmt. Andererseits können sich die spezifischen Sternentstehungsraten und die Menge an Gas in größerem Maße unterscheiden. Bei $z = 0$ liegt der Übergang zwischen sternformenden Galaxien mit geringer Masse und Galaxien mit gedämpfter Sternentstehung und hoher Masse bei ~ 0.5 dex geringer in IllustrisTNG als in L-GALAXIES. IllustrisTNG produziert zudem signifikant mehr Galaxien mit gedämpfter Sternentstehung bei höheren Rotverschiebungen. Beide Modelle ermitteln für Galaxiehaufen innerhalb der Halos einen Bayronenanteil ähnlich dem kosmischen Wert, wobei IllustrisTNG geringere Bayronenanteile in der Umgebung von Galaxiegruppen voraussagt. Diese Unterschiede sind primär den Differenzen der Feedback-Mechanismen von Sternen und supermassiven schwarzen Löchern geschuldet. Der Gasanteil und die Sternentstehungsraten von Galaxien in und um Galaxienhaufen unterscheiden sich substanziell, wobei in IllustrisTNG Satellitengalaxien weniger Sternentstehung zeigen und weniger Gas haben. Wir zeigen, dass die umgebungsbedingten Prozesse wie die Abtragung durch Staudruck in IllustrisTNG stärker sind. Weiterhin wirken sie auf größeren Distanzen und für breitere Bereiche von Halomassen. Daher muss die Behandlung der Galaxieentwicklung in dem semi-analytischen Modell derart verbessert werden, dass die lokalen umgebungsbedingten Effekte besser berücksichtigt werden.

Um die Behandlung der umgebungsbedingten Effekte in L-GALAXIES zu verbessern, führen wir eine "Local Background Environment" (LBE) Schätzfunktion ein. Diese Funktion kann innerhalb und um jede Galaxie oder ihres Subhalos dunkler Materie in hochauflösenden kosmologischen Simulationen gemessen werden kann. Die LBE Schätzfunktion wurde so entworfen, dass sie den Einfluss der umgebungsbedingten Effekte wie der Abtragung durch Staudruck auf die Formation und Entwicklung von Galaxien in semi-analytischen Modellen erfassen kann. Wir definieren das LBE direkt auf Grundlage der Partikeldaten innerhalb einer adaptiven sphärischen Schale und entwerfen eine Gauss'sche Mischungsschätzfunktion um Hintergrundpartikel von zuvor unidentifizierten Subhalo-Partikeln zu unterscheiden.

Bei Analyse der LBE Eigenschaften zeigt sich, dass sich das LBE von Satellitengalaxien relativ zu den beherbergenden Halos bewegt, was im Widerspruch zu üblichen Annahmen steht. Die Orientierungen der Geschwindigkeiten von Subhalos und ihrer LBEs stimmen gut in den äußeren Regionen von Halos mit positiven Einfallgeschwindigkeiten überein. Demgegenüber sind diese Orientierungen unkorreliert nahe der Halozentren. Es gibt jedoch keine abrupte Veränderung der LBE Geschwindigkeit oder Dichte beim Virialradius der Halos. Dies impliziert, dass Abtragung auch außerhalb jener Distanz erfolgen sollte.

Mit Anwendung der LBE Messungen aktualisieren wir L-Galaxies durch Formulierung einer genaueren Behandlung von Abtragung durch Staudruck für alle Galaxien. Wir kalibrieren das modifizierte L-Galaxies Modell erneut mithilfe des Markov-Chain-Monte-Carlo-Verfahrens (MCMC) unter Berücksichtigung der stellaren Massenfunktion und des Anteils gedämpfter Galaxien bei Rotverschiebungen zwischen $0 \leq z \leq 2$. Durch diese erneute Kalibrierung bleiben globale Relationen von Galaxiepopulationen, wie etwa der stellaren Massenfunktion, der HI Massenfunktion und des Galaxieanteils mit gedämpfter Sternentstehung als Funktion der Masse, größtenteils unverändert und sind weiterhin kompatibel mit Beobachtungsdaten. Mit dem Vergleich zu Beobachtungsdaten von SDSS und HSC bezüglich der Galaxieeigenschaften in verschiedenen Umgebungen können wir zeigen, dass unser modifiziertes Modell die Übereinstimmung mit den Beobachtungen in verschiedenen Statistiken erhöht. Verbesserungen zeigen sich im Speziellen bezüglich des Anteils gedämpfter Galaxien und der Sternentstehungsraten von Galaxien als Funktion der Umgebung, der stellaren Masse und der Rotverschiebung. Insgesamt produziert unser neues Modell im Umfeld von Halos mit Gesamtmassen zwischen 10^{12} bis $10^{15}\mathrm{M}_\odot$ bei $z = 0$ höhere Anteile gedämpfter Galaxien und stärkere Abhängigkeiten der Umgebung, was die beobachteten Tendenzen bei halozentrischen Distanzen von einigen Vielfachen der Virialradien besser wiedergibt. Durch Analyse der tatsächlichen Menge des von Galaxien abgetragenen Gases in unserem Modell zeigen wir dass jene Galaxien in der Umgebungen von massiven Halos einen großen Anteil ihres heißen Halogases verlieren *bevor* sie zu Satellitengalaxien werden. Wir zeigen dass sich dies auf die Dämpfung der Sternentstehung in Galaxien sowohl innerhalb und als auch außerhalb der Halogrenze auswirkt. Dies beeinflusst wahrscheinlich die Korrelationen zwischen Galaxien auf Distanzen bis zu einigen zehn Megaparsecs.

Summary

In this thesis, we study the role of environment in galaxy evolution both from theory and from observations. We first perform a comparison, object-by-object and statistically, between the Munich semi-analytical model, L-Galaxies, and the IllustrisTNG hydrodynamical simulations. By running L-Galaxies on the IllustrisTNG dark matter-only merger trees, we identify the same galaxies in the two models. We find that both the stellar mass functions and the stellar masses of individual galaxies agree to better than ~ 0.2 dex. On the other hand, specific star formation rates and gas contents can differ more substantially. At $z = 0$ the transition between low-mass star-forming galaxies and high-mass, quenched galaxies occurs at a stellar mass scale ~ 0.5 dex lower in IllustrisTNG than in L-Galaxies. IllustrisTNG also produces substantially more quenched galaxies at higher redshifts. Both models predict a halo baryon fraction close to the cosmic value for clusters, but IllustrisTNG predicts lower baryon fractions in group environments. These differences are due primarily to differences in modelling feedback from stars and supermassive black holes. The gas content and star formation rates of galaxies in and around clusters and groups differ substantially, with IllustrisTNG satellites less star-forming and less gas-rich. We show that environmental processes such as ram-pressure stripping are stronger and operate to larger distances and for a broader host mass range in IllustrisTNG. As a result, the treatment of galaxy evolution in the semi-analytic model needs to be improved by prescriptions which capture local environmental effects more accurately.

To improve L-Galaxies treatment of environmental processes, we introduce a Local Background Environment (LBE) estimator that can be measured in and around every galaxy or its dark matter subhalo in high-resolution cosmological simulations. The LBE is designed to capture the influence of environmental effects such as ram-pressure stripping on the formation and evolution of galaxies in semi-analytical models. We define the LBE directly from the particle data within an adaptive spherical shell, and devise a Gaussian mixture estimator to separate background particles from previously unidentified subhalo particles. Analyzing the LBE properties, we find that the LBE of satellite galaxies is not at rest with respect to their host halo, in contrast to typical assumptions. The orientations of the velocities of a subhalo and its LBE are well aligned in the outer infall regions of haloes, but decorrelated near halo center. Significantly, there is no abrupt change in LBE velocity or density at the halo virial radius. This suggests that stripping should also happen beyond this radius.

Employing the LBE measurements, we update L-Galaxies by formulating a more

accurate treatment of ram-pressure stripping for all galaxies. We fully re-calibrate the modified L-GALAXIES model using a Markov Chain Monte Carlo (MCMC) method with the stellar mass function and quenched fraction of galaxies at $0 \leq z \leq 2$ as constraints. Due to this re-calibration, global galaxy population relations, including the stellar mass function, quenched fractions versus galaxy mass and HI mass function are all largely unchanged and remain consistent with observations. By comparing to data on galaxy properties in different environments from the SDSS and HSC surveys, we demonstrate that our modified model improves the agreement with the quenched fractions and star formation rates of galaxies as a function of environment, stellar mass, and redshift. Overall, in the vicinity of haloes with total mass 10^{12} to $10^{15} \mathrm{M}_\odot$ at $z = 0$, our new model produces higher quenched fractions and stronger environmental dependencies, better recovering observed trends with halocentric distance up to several virial radii. By analysing the actual amount of gas stripped from galaxies in our model, we show that those in the vicinity of massive haloes lose a large fraction of their hot halo gas *before* they become satellites. We demonstrate that this affects galaxy quenching both within and beyond the halo boundary. This is likely to influence the correlations between galaxies up to tens of megaparsecs.

To the only one who never left me behind.

Chapter 1

Introduction

The expanding Universe is well described by the standard model of cosmology, ΛCDM, on large scales. The modern theory of galaxy formation and evolution is based on the theory of gravity with initial conditions well-specified by cosmic microwave background observations (Spergel et al. 2003; Komatsu et al. 2011; Ade et al. 2014; Aghanim et al. 2018). One of the critical assumptions of ΛCDM is that cold dark matter interacts at best only very weakly with other matter except gravitationally, which has formed the basis of a number of projects that have simulated a gravity only (dark matter only) universe (e.g. Davis et al. 1985; Springel et al. 2005; Boylan-Kolchin et al. 2009; Klypin et al. 2011; Riebe et al. 2011; Angulo et al. 2012; Skillman et al. 2014; Wang et al. 2020b). Above all, these simulations have shown that galaxy formation within ΛCDM can successfully reproduce the observed patterns of galaxy clustering within the cosmic web.

However, the Universe is observed in light coming from stars and gas, which make up galaxies. These are all made of baryonic matter, which interacts in much more complicated ways than weakly interacting gravity-only cold dark matter. In the standard paradigm of how galaxies form in a Universe where dark matter clusters hierarchically (White & Rees 1978), baryonic matter accretes into the gravitational potential wells of dark matter haloes. In the form of primordial diffuse gas, this baryonic matter shock-heats and then cools and contracts to form stars. The death of stars releases energy, mass, and heavy elements into the interstellar medium. This energy reheats the cold gas, redistribute it, and pushes it into the hot halo atmosphere. A fraction of the heated gas can itself be ejected out of the halo boundary. Black hole feedback is the major mechanism for quenching star formation in massive galaxies. Black holes grow by cold gas accretion and during mergers. Galaxies can accrete gas from the hot gas of their host subhaloes, producing AGN feedback, which releases energy and momentum into the surrounding environment, which can reheat and redistribute the gas, and, as a result, quench star formation in massive galaxies. Furthermore, halo mergers and galaxy mergers play a critical role in galaxy evolution. Depending on their formation and evolution, galaxies appear in different shapes. A flow chart illustrating some physical processes involved in galaxy evolution, especially regarding galaxies' morphology, is shown in Fig. 1.1. Overall, baryons evolve under the influence of a complex set of physical processes beyond gravity alone, producing a rich phenomenology

in the study of galaxy formation (see Mo et al. 2010 for a full discussion).

In addition to intrinsic physical processes, galaxy evolution is also strongly influenced by environment (Hubble & Humason 1931; Boselli & Gavazzi 2006). In other words, the properties of galaxies/subhaloes are strongly correlated with their local density (Yan et al. 2013). For example, galaxies have different local densities when they are within clusters (Boselli et al. 2016; Pallero et al. 2019), filaments (Sarron et al. 2019) and voids (Tavasoli et al. 2013; Mosleh et al. 2018). Well known examples of these phenomena are the morphology-density relation (Oemler 1974; Dressler 1980) and higher fraction of quenched galaxies within massive clusters (Kauffmann et al. 2004; Peng et al. 2010; Davies et al. 2019). Environmental processes such as ram-pressure stripping (Gunn & Gott 1972) and tidal stripping (Binney & Tremaine 1987) can strip the gas out of galaxies, affecting their gas reservoirs (Wang et al. 2020a), star formation (Donnari et al. 2020a,b), stellar properties (Webb et al. 2020), morphology (Joshi et al. 2020), and so on. As a result, we cannot understand galaxy evolution without understanding environmental processes properly. In this thesis, we investigate the role of environment in galaxy evolution both from theory and from observation.

1.1   Modelling galaxy formation and evolution

The complex interplay of the physical phenomena imply that it is impossible to derive the properties of galaxies with a purely analytical approach. As a result, numerical and semi-numerical approaches such as semi-analytical modelling (Kauffmann et al. 1993, 1999; Somerville & Primack 1999; Cole et al. 2000; Springel et al. 2001b; De Lucia et al. 2006; Guo et al. 2011; Lacey et al. 2016; Henriques et al. 2020) or hydrodynamical simulations (Hernquist & Katz 1989; Gottlöber & Yepes 2007; Schaye et al. 2015; Davé et al. 2017; Springel et al. 2018; Pillepich et al. 2018a; Nelson et al. 2019b) are required.

A semi-analytical model (SAM) is a phenomenological tool that uses a set of simplified equations to account for the key baryonic physical processes involved in the formation and evolution of galaxies. Early SAMs that were coupled to merger trees derived using analytical approaches such as Press-Schechter (PS, Press & Schechter 1974) and extended PS formalism (Bond et al. 1991; Sheth et al. 2001) were able to produce galaxy populations with properties comparable with observations (Kauffmann et al. 1993, 1999; Somerville & Primack 1999; Cole et al. 2000). A semi-analytical model was performed by Kauffmann et al. (1999) on halo merger trees detected based on the Friends of Friends (FOF) algorithm (Davis et al. 1985). Improved simulation techniques (Springel et al. 2001a; Springel 2005) and the completion of larger dark matter only (DMO) simulations such as Millennium (Springel et al. 2005) enabled new generations of modern SAMs to run on subhalo merger trees from those DMO simulations (De Lucia et al. 2006; Croton et al. 2006). Today, some SAMs run on top of merger trees generated from simulations and implement a wide variety of physical processes, including gas cooling, disc and bulge formation, stellar and black hole feedback, and environmental effects (Guo et al. 2013; Lacey et al. 2016; Croton et al. 2016; Lagos et al. 2018; Cora et al. 2018; Henriques et al. 2020).
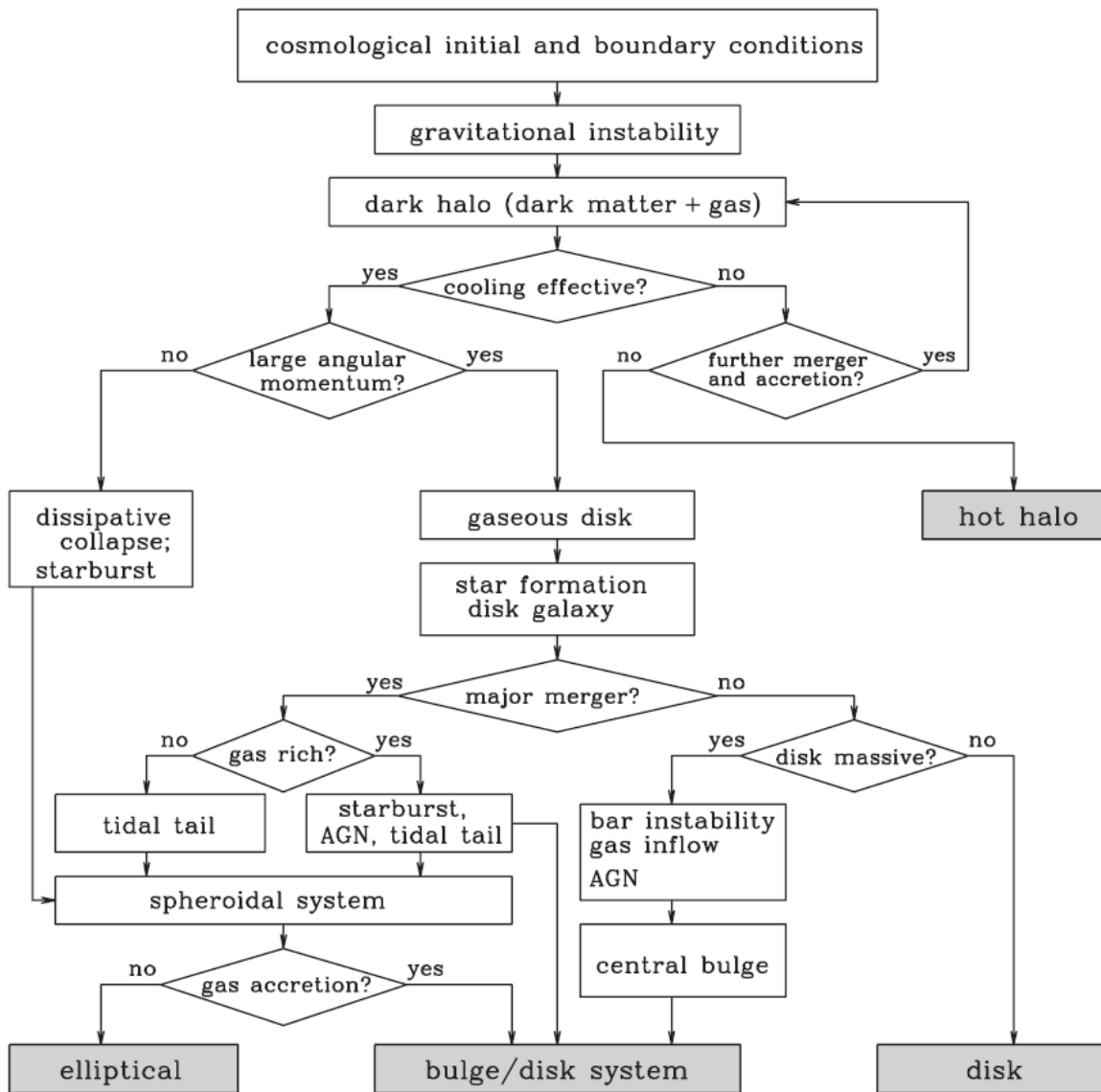
Figure 1.1: A flow chart illustrating some relevant physical processes involved in galaxy formation and evolution, especially regarding galaxies' morphology. This figure is taken from Mo et al. (2010).

Hydrodynamical simulations offer a sophisticated methodology to model galaxy formation and evolution. They solve the equations of gravity, (magneto)hydrodynamics, and thermodynamics for dark matter, gas, and stars (Teyssier 2002; Springel 2010; Bryan et al. 2014; Hopkins 2015; Wadsley et al. 2017). In §1.2 of this chapter we describe the treatment of physical processes in the Munich semi-analytical model, L-Galaxies. Moreover, in §1.3 we provide a brief description of the IllustrisTNG hydrodynamical simulation. Both of these galaxy formation models are used in this thesis.

1.2 L-Galaxies semi-analytical model

1.2.1 Overview of the galaxy formation model

The "Munich" model of galaxy formation is a semi-analytical model that uses a set of equations to model baryonic physics on top of dark matter halo merger trees and has been continually developed for many years (White 1989; White & Frenk 1991; Kauffmann et al. 1993, 1999; Springel et al. 2001b, 2005). More recent versions of the Munich model, L-Galaxies, are designed to run on a dark matter only simulation, traditionally the Millennium (Springel et al. 2005) and Millennium-II (Boylan-Kolchin et al. 2009) simulations, resulting in a number of model branches and updates (Springel et al. 2005; Croton et al. 2006; De Lucia et al. 2006; Bertone et al. 2007; Guo et al. 2011; Yates et al. 2013; Henriques et al. 2015; Henriques et al. 2020)[1].

The model we have developed in this thesis is based on the Henriques et al. (2020) model (H20 hereafter). Following previous versions, we also run the model on top of the Millennium and Millennium-II simulations. Both simulations are re-scaled to the Planck cosmology (Planck Collaboration 2016) from their original older cosmologies, applying the method introduced by Angulo & White (2010) as updated by Angulo & Hilbert (2015).

The H20 model improved on the Henriques et al. (2015) model (H15 hereafter) by adding a radially resolved treatment of formation and evolution of galaxy discs, while H15 itself improved on the Guo et al. (2011) model (G11 hereafter). H15 presented an updated implementation of gas recycling processes and feedback processes to fit high redshift galaxy populations more accurately. H15 and H20 also limited ram-pressure stripping to satellite galaxies within the halo virial radius of massive clusters, a merely numerical fix to avoid predicting too many low-mass quenched satellite galaxies. One of the goals of this thesis is to fully remove this artificial threshold and extend gas stripping to all galaxies, regardless of their local environment.

Before H15, Guo et al. (2011) updated earlier models with more accurate treatment of physical processes, including photo-ionization heating, supernova feedback, and galaxy mergers to better model the low-mass galaxy population. In order to follow the size evolution of discs and bulges, G11 implemented accurate tracking of angular momentum

---

[1]The outputs of the Millennium and Millennium-II simulations, and also different versions of L-Galaxies are publicly available at http://gavo.mpa-garching.mpg.de/MyMillennium/. The L-Galaxies code and also output catalogues are publicly available at https://lgalaxiespublicrelease.github.io/.

of different galaxy components.

In the version of L-Galaxies used in this thesis, baryonic matter bound to each galaxy/subhalo is divided into seven main components: hot gas, cold gas (partitioned into HI and H_2), stellar disc, bulge stars, halo stars, the supermassive black holes, and ejected material. The model initiates baryonic physics for every subhalo by seeding it with the expected fraction of diffuse hot (non-star-forming) gas at its formation time. This gas radiates energy and cools to form cold gas, containing neutral and molecular hydrogen components. Once the H_2 surface mass density exceeds a certain limit, stars are born. Both the cold gas and stellar components in the galactic disc are followed in twelve concentric rings and all the relevant physical processes happen within these rings.

Galaxy mergers play a key role in starbursts and the formation and growth of supermassive black holes at the centres of galaxies. Feedback processes such as stellar and black hole feedback quench star formation for low-mass and massive galaxies, respectively. The energy released by supernova feedback heats the cold gas and pushes it out of the galactic disc into the hot gas component. The remaining energy is able to drive the material of the hot gas component out of the subhalo into a reservoir of ejected material where it is no longer available for cooling. The timescale for the reincorporation of the ejected gas is assumed to be proportional to $1/M_{200}$. As a result, gas returns to massive haloes quickly, while a fraction of the gas ejected out of low-mass haloes may never return. Moreover, environmental effects such as tidal and ram-pressure stripping can remove gas out of galaxies in dense environments and quench star formation.

In this section, we describe the L-Galaxies treatment of physical processes most relevant to this thesis. A more comprehensive, detailed description is given in the Supplementary material of Ayromlou et al. (2021b) who updated previous model descriptions from Guo et al. (2011); Henriques et al. (2015); Henriques et al. (2020).

1.2.2 Dark Matter Simulations

In this thesis, we use the particle and halo merger tree data of the Millennium and Millennium-II simulations (Springel et al. 2005; Boylan-Kolchin et al. 2009). Both simulations are re-scaled to the Planck cosmology (Planck Collaboration 2016) from their original older cosmology, applying the method introduced by Angulo & White (2010) as updated by Angulo & Hilbert (2015). The properties of the simulations are given in Table 1.1. In addition, Fig. 1.2 shows the dark matter distribution in the Millennium simulation. In all simulation snapshots, dark matter haloes are identified using a Friends Of Friends (FOF) algorithm (Davis et al. 1985). Each FOF halo has one central subhalo and its other subhaloes are categorised as satellites.

All subhaloes are detected using the SubFind algorithm (Springel et al. 2001b). The algorithm sets a minimum of 20 particles for each subhalo to be included in the simulation catalogue. For every FOF halo, there is a virial radius, R_{200}, defined as the radius in which the matter density is 200 times the critical density of the Universe. The mass within R_{200} is known as the virial mass, M_{200}. Although it is common to consider R_{200} as the halo boundary, the FOF halo can extend beyond R_{200}. Therefore, satellite subhaloes of a FOF

Table 1.1: Parameters used in the Millennium (Springel et al. 2005) and Millennium-II (Boylan-Kolchin et al. 2009) simulations in their original (WMAP1, Spergel et al. 2003) and re-scaled cosmology (Planck1, Planck Collaboration 2016) based on Angulo & White (2010); Angulo & Hilbert (2015).

Parameter	MS (WMAP1)	MS (Planck1)	MS-II (WMAP1)	MS-II (Planck1)
Ω_{m}	0.25	0.315	0.25	0.315
Ω_{b}	0.045	0.049	0.045	0.049
Ω_{Λ}	0.75	0.685	0.75	0.685
$\mathrm{H}_0[\mathrm{km/s/Mpc}]$	73	67.3	73	67.3
n_{s}	1	0.96	1	0.96
σ_8	0.9	0.826	0.9	0.826
$N_{\mathrm{particles}}$	2160^3	2160^3	2160^3	2160^3
$m_{\mathrm{particle}}[\mathrm{M}_\odot]$	1.18×10^9	1.43×10^9	9.42×10^6	1.14×10^7
$l_{\mathrm{box}}[\mathrm{Mpc}]$	684	714	137	143
N_{snapshot}	64	64	68	68
z_{initial}	127	56	127	56

halo can exist beyond this scale as well. The FOF algorithm links particles at fixed inter-particle separation and the resulting FOF system can have a non-spherical shape, meaning that there is no strict correspondence requiring satellite subhaloes to be within R_{200}.

Different types of galaxies

In L-Galaxies there are three types of galaxies: (i) central galaxies, also known as type 0 galaxies, which reside in the central subhalo of each FOF halo. (ii) Satellite galaxies with an identified subhalo, i.e. detected by the subhalo finder algorithm (here Subfind), which comprise all other subhalos in a FOF besides the central. These are called type 1 galaxies. (iii) Satellite galaxies without an identified subhalo, i.e. their subhaloes have been tidally disrupted below the simulation resolution and are no longer detectable. These are called orphan, or type 2, galaxies. The model tracks the position and velocity of type 2 galaxies by following the most bound particle of their former subhalo. This way, L-Galaxies continues the evolution of orphan galaxies even when their subhaloes are no longer detectable. In the rest of this thesis, we use the phrases "subhalo" and "galaxy" interchangeably with the exception of "orphan galaxies".

1.2.3   Infall and reionization

The model initiates baryonic physics for every subhalo by seeding it with the expected fraction of diffuse hot (non-star-forming) gas at its formation time, which follows the approach of White & Frenk (1991). For every halo, the infall of gas continues at later times. The L-Galaxies infall recipe is that the gas accretion rate onto haloes is equal to
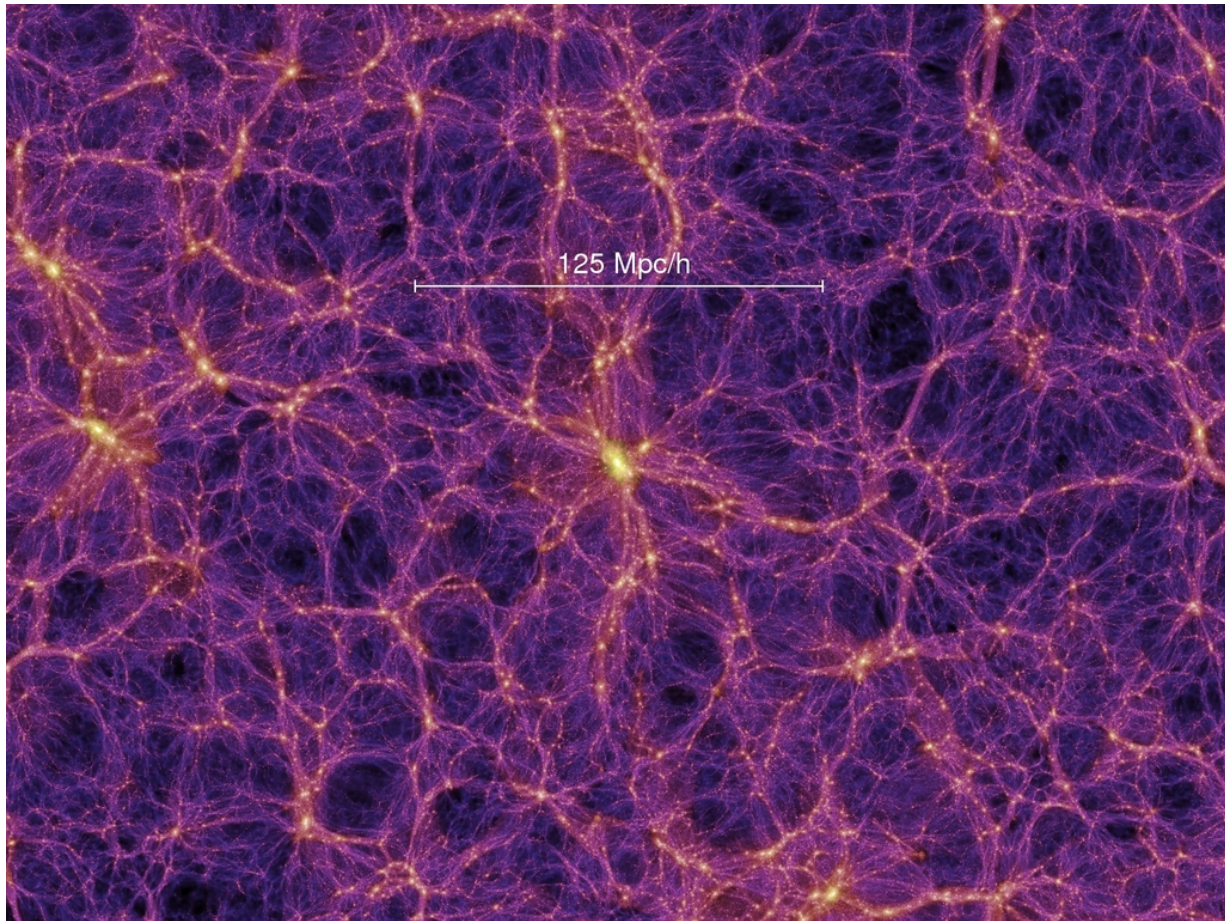
Figure 1.2: Dark matter distribution in the Millennium simulation, taken from the webpage of the Millennium simulation.

the accretion rate of total matter times $f_{\rm b}$. Except for low-mass haloes, $f_{\rm b}$ is very close to the cosmic baryon fraction. However, for low-mass haloes, photo-heating by the UV background field increases the temperature of diffuse halo gas, and the gas pressure effects decrease the gas infall rate (Efstathiou 1992). This causes $f_{\rm b}$ to decrease significantly for very low-mass haloes. In L-GALAXIES, the approach of Gnedin (2000) is used for deriving $f_{\rm b}$ in haloes less massive than a characteristic mass $M_F(z)$:

$$f_b(z, M_{\rm 200c}) = f_b^{\rm cos} \left(1 + (2^{\alpha/3} - 1) \left[\frac{M_{\rm 200c}}{M_F(z)} \right]^{-\alpha} \right)^{-3/\alpha}. \tag{1.1}$$

Here $\alpha = 2$ and $M_F(z)$ is taken from Okamoto et al. (2008).

The total halo mass can decrease with time because of changes in morphology or halo concentration (see De Lucia et al. 2004 for discussions about subhalo mass fluctuations). At the same time, in L-GALAXIES the halo baryonic mass within R_{200} remains unchanged by construction, which could cause an increase in the baryon fraction. Following the prescription of Yates et al. (2017), in this thesis we correct the input halo merger trees to prevent M_{200} from decreasing with time. This accounts for any artificial decrease in M_{200} measured when determining R_{200} based on the assumption of spherical symmetry.

1.2.4   Gas cooling and star formation

Gas Cooling

In §1.2.3, we explained how diffuse gas is given to dark matter haloes. For low-mass haloes and at early times, this gas cools onto the disc of their central galaxies at a short time-scale. On the other hand, for more massive haloes and at later times, the gas is added to a quasi-static hot atmosphere that does not immediately cool onto the disc but accretes at a slower rate through a cooling flow. The characteristic halo mass at which these two regimes are separated is about $M \sim 10^{12} M_\odot$ (White & Rees 1978; White & Frenk 1991; Forcada-Miro & White 1997; Birnboim & Dekel 2003).

To model this, an isothermal density profile is assumed for the hot halo gas:

$$\rho_{\rm hot}(r) = \frac{M_{\rm hot}}{4\pi R_{\rm 200c} r^2}, \tag{1.2}$$

where $M_{\rm hot}$ is the hot gas mass of the halo. The cooling time, $t_{\rm cool}(r)$, is then calculated as the ratio of the thermal energy of the gas to its cooling rate density (i.e. per unit volume):

$$t_{\rm cool}(r) = \frac{3\mu m_{\rm H} k T_{\rm 200c}}{2\rho_{\rm hot}(r) \Lambda(T_{\rm hot}, Z_{\rm hot})}. \tag{1.3}$$

Here, $\Lambda(T_{\rm hot}, Z_{\rm hot})$ is the equilibrium cooling function (Sutherland & Dopita 1993) and $\rho_{\rm hot}(r)$ is given by Eq. 1.2. $\mu m_{\rm H}$ is the mean particle mass, k is the Boltzmann constant,

and $Z_{\rm hot}$ is the hot gas metallicity. Moreover, $T_{\rm hot}$ is the hot gas temperature, assumed to be the same as the halo virial temperature:

$$T_{\rm 200c} = 35.9\,(V_{\rm 200c}/{\rm km\,s^{-1}})^2\,{\rm K}. \tag{1.4}$$

For central subhaloes, the halo virial temperature is calculated at each simulation snapshot. For satellite subhaloes, however, the model simply takes $T_{\rm 200c}$ at infall time.

The radius where the cooling time equals the halo dynamical time is the cooling radius:

$$r_{\rm cool} = \left[\frac{t_{\rm dyn,h}M_{\rm hot}\Lambda(T_{\rm hot},Z_{\rm hot})}{6\pi\mu m_{\rm H}kT_{\rm 200c}R_{\rm 200c}}\right]^{\frac{1}{2}}. \tag{1.5}$$

Here, $t_{\rm dyn,h}$ is the halo dynamical time, given by $R_{\rm 200c}/V_{\rm 200c} = 0.1H(z)^{-1}$ (De Lucia et al. 2004).

Depending on the halo virial mass (or equivalently virial radius), the halo is assumed to be in either cooling from quasi-static hot atmosphere ($r_{\rm cool} < R_{\rm 200c}$) or rapid infall regime ($r_{\rm cool} > R_{\rm 200c}$), with a smooth transition between the two regimes (Guo et al. 2011). When $r_{\rm cool} < R_{\rm 200c}$:

$$\dot{M}_{\rm cool} = M_{\rm hot}\frac{r_{\rm cool}}{R_{\rm 200c}}\frac{1}{t_{\rm dyn,h}}. \tag{1.6}$$

On the other hand, when $r_{\rm cool} > R_{\rm 200c}$ rapid infall occurs, and the accretion of material onto the central galaxy happens on the halo dynamical time (i.e. in free fall):

$$\dot{M}_{\rm cool} = \frac{M_{\rm hot}}{t_{\rm dyn,h}}. \tag{1.7}$$

Gas infall into galaxies

Once the hot gas cools, it is added to the disc, following an exponential profile:

$$\Sigma_{\rm gas}(r) = \Sigma_{\rm gas}^0 \exp(-r/r_{\rm infall}), \tag{1.8}$$

where

$$\Sigma_{\rm gas}^0 = \frac{m_{\rm cool}}{2\pi r_{\rm infall}^2}. \tag{1.9}$$

Here, $r_{\rm infall}$ is given by the equation below:

$$r_{\rm infall} = \frac{j_{\rm halo}}{2V_{\rm c}}, \tag{1.10}$$

which is based on the assumption of angular momentum conservation during the cooling and infall of the gas (Mo et al. 1998). $j_{\rm halo}$ and $V_{\rm c}$ are the halo specific angular momentum and circular speed, respectively.

Given that the disc and halo size increase with time (i.e. larger at low redshifts), the radial extent of infalling material is smaller at high redshifts and becomes larger at low redshfits. This results in an inside-out growth of discs, which is consistent with several disc formation models (e.g. see Kauffmann 1996; Dalcanton et al. 1997; Avila-Reese et al. 1998; Dutton 2009; Fu et al. 2009; Pilkington et al. 2012).

Star formation

Following the prescription of Fu et al. (2010, 2012, 2013), the cold gas is partitioned into neutral and molecular hydrogen components (see also Krumholz et al. 2009; McKee & Krumholz 2010). Based on Fu et al. (2013) and Henriques et al. (2020), star formation surface density is given by:

$$\Sigma_{\mathrm{SFR}} = \alpha_{\mathrm{H_2}} \Sigma_{\mathrm{H_2}} / t_{\mathrm{dyn}}, \tag{1.11}$$

where $t_{\mathrm{dyn}} = R_{\mathrm{cold}}/V_{\mathrm{max}}$ is the dynamical time of the disc and $\alpha_{\mathrm{H_2}}$ is a model parameter which is derived in our MCMC model calibration (see §1.2.7 and §4.2.3).

In the $\mathrm{H_2}$ based star formation prescription given above, star formation efficiency decreases with time (i.e. more efficient at high redshifts), which is consistent with observations (e.g. see Genzel et al. 2015; Scoville et al. 2017).

In addition, stars can form during merges. In the current L-GALAXIES, this is formulated employing the "collisional starburst" approach of Somerville et al. (2001):

$$M_{\star,\mathrm{burst}} = \alpha_{\mathrm{SF,burst}} \left(\frac{M_1}{M_2} \right)^{\beta_{\mathrm{SF,burst}}} M_{\mathrm{cold}}, \tag{1.12}$$

where M_1 and M_2 are the total baryonic masses of the two merging galaxies ($M_1 < M_2$), and M_{cold} is the sum of their cold gas masses. Moreover, $\alpha_{\mathrm{SF,burst}}$ and $\beta_{\mathrm{SF,burst}}$ are model parameters which are derived in our model calibration.

1.2.5 Supernova feedback

Supernova feedback in central galaxies

In L-GALAXIES, supernova feedback injects energy into the cold star-forming gas, heating some fraction through transfer to the hot gas. The remaining energy, if any, is able to drive the material of the hot gas component out of the subhalo into a reservoir of ejected material where it is no longer available for cooling. Gas in the ejected reservoir can return to the hot gas on a reincorporation timescale, thus becoming available for cooling again.

The available energy from supernova feedback is:

$$\Delta E_{\mathrm{SN}} = \epsilon_{\mathrm{halo}} \times \Delta M_{\star,R} \eta_{\mathrm{SN}} E_{\mathrm{SN}}, \tag{1.13}$$

where E_{SN} represents the amount of the energy released by a single supernova and equals 10^{51}erg. $\Delta M_{\star,R}$ is the mass returned to the interstellar medium (i.e. via supernovae or stellar winds), and η_{SN} is the number of supernovae per solar mass of $\Delta M_{\star,R}$. Assuming a universal Chabrier (2003) IMF, $\eta_{\mathrm{SN}} = 0.0149\,\mathrm{M_\odot}^{-1}$. Moreover, ϵ_{halo} is a model efficiency parameter and is defined as:

$$\epsilon_{\mathrm{halo}} = \eta_{\mathrm{eject}} \times \left[0.5 + \left(\frac{V_{\mathrm{max}}}{V_{\mathrm{eject}}} \right)^{-\beta_{\mathrm{eject}}} \right], \tag{1.14}$$

where η_{eject}, V_{eject}, and β_{eject} are all free parameters which are derived in our model calibration (see §1.2.7 and §4.2.3).

The energy released by supernovae is first used to reheat cold gas and add it to the hot gas component. The mass of the reheated gas is

$$\Delta M_{\mathrm{reheat},i} = \epsilon_{\mathrm{disc}}\Delta M_{\star,R_i}, \tag{1.15}$$

where $M_{\star,R_i}$ refers to the mass of stars returned to the ISM from the ith disc ring. Furthermore, ϵ_{disc} is another model parameter given by:

$$\epsilon_{\mathrm{disc}} = \epsilon_{\mathrm{reheat}} \times \left[0.5 + \left(\frac{V_{\mathrm{max}}}{V_{\mathrm{reheat}}} \right)^{-\beta_{\mathrm{reheat}}} \right]. \tag{1.16}$$

Here, $\epsilon_{\mathrm{reheat}}$, V_{reheat}, and β_{reheat} are again free parameters which are derived in our MCMC model calibration (see §1.2.7 and §4.2.3).

After heating the cold gas, the remaining energy, if any, drives material of the hot gas component into the ejected reservoir, where it is no longer available for cooling. The amount of the ejected gas is given by:

$$\frac{1}{2}\Delta M_{\mathrm{eject}}V_{\mathrm{200c}}^2 = \Delta E_{\mathrm{SN}} - \Delta E_{\mathrm{reheat}}, \tag{1.17}$$

where E_{reheat} is the energy required to reheat the whole cold gas and move it to the hot gas component. If $E_{\mathrm{SN}} < E_{\mathrm{reheat}}$, no hot gas will be moved to the ejected reservoir.

Supernova feedback in satellite galaxies

The supernova feedback prescription we take for satellite galaxies (i.e. type 1 and type 2 galaxies) is rather similar to our approach for central galaxies, with a few differences that are explained here. First of all, when deriving the supernova efficiency parameters for satellite galaxies (i.e. Eqs. 1.14 and 1.16), the V_{max} at infall time is employed.

Type 2 satellite galaxies (orphan galaxies) are empty of hot gas due to tidal stripping (see 3.2.2). As a result, in orphan galaxies, the reheated gas is directly added to the hot gas component of their host subhalo, either a type 1 satellite subhalo or a central subhalo, and the remaining energy ejects material from the hot gas component of their host subhaloes. In type 1 satellite galaxies, the reheating process is similar to the reheating processes in central galaxies. However, tidal stripping immediately removes a fraction of the reheated gas.

Reincorporation of gas ejected in winds

The gas in the ejected reservoir is not available for cooling. However, it can return to the hot gas on a reincorporation timescale, thus becoming available for cooling again. Following Henriques et al. (2013), the rate at which ejected gas returns to the hot gas component is given by:

$$\dot{M}_{\mathrm{ejec}} = -\frac{M_{\mathrm{ejec}}}{t_{\mathrm{reinc}}}, \tag{1.18}$$

where t_{reinc} is the reincorporation time-scale and is is inversely proportional to the total halo mass M_{200c}:

$$t_{\mathrm{reinc}} = \gamma_{\mathrm{reinc}} \frac{10^{10}\,\mathrm{M_\odot}}{M_{\mathrm{200c}}}. \tag{1.19}$$

As a result of the above implementation, gas returns to massive haloes quickly, while a fraction of the gas ejected out of low-mass haloes may never return. This is qualitatively consistent with the results of numerical simulations (Oppenheimer & Davé 2008; Oppenheimer et al. 2010).

1.2.6   Black hole growth and feedback

The current version of L-Galaxies follows the implementation of Henriques et al. (2015), which is based on Croton et al. (2006), for black hole relevant processes. In L-Galaxies, there are two modes of black hole accretion; quasar mode and radio mode. These two accretion modes can coexist. In the quasar mode, black holes grow by cold gas accretion, and during mergers. The amount of mass added to black hole in the quasar mode is:

$$\Delta M_{\mathrm{BH,Q}} = \frac{f_{\mathrm{BH}}(M_{\mathrm{sat}}/M_{\mathrm{cen}})\,M_{\mathrm{cold}}}{1 + (V_{\mathrm{BH}}/V_{\mathrm{200c}})^2}, \tag{1.20}$$

where M_{cen} and M_{sat} are the total baryonic mass of the two merging galaxies (i.e. the central and the satellite galaxy), M_{cold} is the sum of their cold gas masses, and V_{200c} corresponds to the virial velocity of their host halo. Moreover, f_{BH} and V_{BH} are model parameters which we derive from our MCMC model calibration (see §1.2.7 and §4.2.3).

Based on the prescription given in Eq. 1.20, the accretion rate depends on the total cold gas mass of both merging galaxies and the ratio of their total baryonic masses. This accretion mode is therefore more efficient for major mergers and less efficient for minor mergers. The final mass of the central black hole of the merged galaxy is the sum of the total black hole mass of the two merging galaxies and the accreted mass. No explicit feedback mechanism is attributed to the quasar mode.

In the radio mode, galaxies can accrete gas from the hot gas of their host subhaloes, producing radio-mode AGN feedback. In this state black holes inject energy into the hot gas, which suppresses cooling and as a result, star formation. The amount of energy injected into the hot gas in the radio mode is given by:

$$\dot{E}_{\mathrm{radio}} = \eta \dot{M}_{\mathrm{BH}} c^2, \tag{1.21}$$

where c is the speed of light and η is a model parameter set to 0.1. In addition $\dot{M}_{\mathrm{BH}}$ is:

$$\dot{M}_{\mathrm{BH}} = k_{\mathrm{AGN}} \left(\frac{M_{\mathrm{hot}}}{10^{11}\,\mathrm{M_\odot}} \right) \left(\frac{M_{\mathrm{BH}}}{10^8\,\mathrm{M_\odot}} \right). \tag{1.22}$$

Here, M_{BH} is the black hole mass, M_{hot} is its host subhalo hot gas mass, and k_{AGN} is a model parameter which we derive from our MCMC model calibration (see §1.2.7 and §4.2.3).

Given that the amount of energy injected into the hot gas in the radio mode is proportional to the black hole mass and the host subhalo hot gas mass, the radio mode is most effective for massive galaxies, whose black holes reside in high-mass haloes where hot gas dominates the baryon budget. The effective cooling rate after the injection of energy into the hot gas atmosphere equals:

$$\dot{M}_{\text{cool,eff}} = \max \left[\dot{M}_{\text{cool}} - 2\dot{E}_{\text{radio}}/V_{200c}^2, \ 0 \right]. \tag{1.23}$$

The "max" ensures that the cooling rate does not become negative. For satellite galaxies within the virial radius, if $2\dot{E}_{\text{radio}}/V_{200c}^2 > \dot{M}_{\text{cool}}$, the remaining energy is used to suppress cooling of the hot gas of their host haloes.

1.2.7 Model Calibration: Monte Carlo Markov Chains

Like all galaxy formation models and simulations, L-Galaxies has a number of parameters (e.g. the star formation efficiency) that need to be fit. Therefore, we calibrate our new model against a set of observational constraints using the Markov Chain Monte Carlo (MCMC) approach developed by Henriques et al. (2009) based on the Metropolis-Hastings method (Metropolis et al. 1953; Hastings 1970). This approach is also used by previous L-Galaxies versions (Henriques et al. 2013; Guo et al. 2013; Henriques et al. 2015; Henriques et al. 2020). To speed up the model calibration, the MCMC approach runs the model on a representative set of halo merger trees (see Henriques et al. 2013) instead of on the full simulations, a scheme we also adopt. In addition, we extend the previous MCMC method to also incorporate our new treatment of environmental effects. More details about our model calibration is given in §4.2.3.

1.2.8 Environmental processes

Modern versions of L-Galaxies, since Guo et al. (2011), have gradual hot gas stripping which influences satellite galaxies within the halo virial radius. The latest version of the model (Henriques et al. 2020) implements tidal stripping for satellite galaxies within the halo boundary, R_{200}, and limits ram-pressure stripping to satellites within R_{200} of massive clusters with $M_{200} > M_{\text{r.p.}}$, where $\log_{10}(M_{\text{r.p.}}/\text{M}_{\odot}) = 14.7$. This ram-pressure stripping threshold, $M_{\text{r.p.}}$, was a free parameter in the H15 and H20 model calibrations, and the resulting value was found necessary in order to avoid having too many low-mass, red galaxies. Although this results in good agreement with the observed quenched fraction, the approach is merely a numerical fix and is not physical. Completely removing this mass threshold, in this thesis we aim to improve L-Galaxies treatment of environmental stripping processes by introducing a new method to capture environment and model ram-pressure stripping for all galaxies (i.e. all satellite and central galaxies), regardless of their environment. The method and its implementation in L-Galaxies is fully explained in Chapter 3 and Chapter 4.

1.3 IllustrisTNG hydrodynamical simulation

1.3.1 Overview of the simulation

The next generation of the Illustris simulation is the IllustrisTNG project (TNG; Nelson et al. 2018; Springel et al. 2018; Pillepich et al. 2018b; Marinacci et al. 2018; Naiman et al. 2018), a set of graveto-magnetohydrodynamical simulations that model the physical processes most relevant to the formation and evolution of galaxies in cosmological volumes. The TNG model is described in Weinberger et al. (2017) and Pillepich et al. (2018a) and is based on the original Illustris model (Vogelsberger et al. 2013; Torrey et al. 2014), which uses the AREPO code (Springel 2010) to solve the coupled equations of self-gravity and magnetohydrodynamics (Pakmor et al. 2011; Pakmor & Springel 2013). The TNG model implements key physical processes for galaxy formation, including gas cooling, star formation, stellar evolution, and stellar feedback (Pillepich et al. 2018a). Processes pertinent to supermassive black holes (SMBH) include seeding/formation, accretion, mergers and thermal and kinetic feedback (Weinberger et al. 2017).

The TNG model has been used to run three different simulation volumes to date. The largest, TNG300, has a volume of $\sim (300\,\mathrm{Mpc})^3$ with a dark matter resolution of $m_{\mathrm{DM}} = 5.9 \times 10^7 \mathrm{M}_\odot$ and average gas cell mass of $m_{\mathrm{gas}} \simeq 1.1 \times 10^7 \mathrm{M}_\odot$. The intermediate, TNG100, has a volume of $\sim (100\,\mathrm{Mpc})^3$ and dark matter and average gas resolutions of $m_{\mathrm{DM}} = 7.5 \times 10^6 \mathrm{M}_\odot$ and $m_{\mathrm{gas}} \simeq 1.4 \times 10^6 \mathrm{M}_\odot$. We use the publicly available data from both TNG100 and TNG300 (Nelson et al. 2019a). In this thesis, we do not employ the TNG50 simulation, with the highest resolution but smallest volume (Pillepich et al. 2019; Nelson et al. 2019b).

For every TNG hydrodynamic simulation, there is a companion dark matter only (gravity only) simulation which has the same initial conditions, box size and resolution. Comparisons between these dark matter only simulations (hereafter TNG-DMO) and the full hydrodynamical runs can shed light on baryonic effects on the underlying dark matter structure (Springel et al. 2018). The DMO simulations can also be used as input to semi-analytic models, as we do in Chapter 2 of this thesis. All the TNG and TNG-DMO simulations start at $z = 127$ with initial conditions consistent with a Planck ΛCDM cosmology (Planck Collaboration 2016, $h = 0.673$). Haloes are identified using the friends-of-friends (FOF) algorithm (Davis et al. 1985). Bound objects and substructures, i.e. subhaloes and galaxies, are identified and characterised using the SUBFIND algorithm (Springel et al. 2001b), with a minimum of 20 total particles/cells per object.

The TNG model is calibrated using a number of observations of the galaxy population, including the observed star formation rate density, stellar mass function (SMF), and stellar to halo mass ratio at $z = 0$; in addition, the black hole-stellar mass relation, halo gas fraction, and the stellar sizes of galaxies are considered. This calibration is carried out at the fiducial TNG100-1 resolution (Pillepich et al. 2018a). Model parameters are kept fixed between different boxes (resolutions), the only exception being gravitational softening lengths. As a result, the TNG model has non-trivial numerical convergence behaviours, which must be assessed between different resolution levels as a function of the galaxy

property of interest.

1.3.2 Physical processes most relevant to this thesis

Supermassive black hole feedback

In IllustrisTNG, supermassive black hole (SMBH or AGN) feedback is invoked as the physical mechanism for quenching massive galaxies. TNG's black hole feedback scheme has two modes, thermal and kinetic, depending on the accretion rate of the SMBH; these do not operate at the same time. At high accretion rates, black holes heat the surrounding gas thermally. This thermal energy is injected in a small local environment around the black hole which initially increases the temperature of neighbouring gas cells. This will affect the future evolution and thermodynamical properties of gas. At low accretion rates, on the other hand, black holes inject kinetic energy. These randomly oriented, high-velocity outflows displace interstellar star-forming gas (Nelson et al. 2019b) as well as circumgalactic medium gas (Truong et al. 2020; Davies et al. 2020). They are also preventative (Terrazas et al. 2020), modulating the cooling properties of the hot halo (Zinger et al. 2020) and effectively suppressing star formation (Weinberger et al. 2018). SMBH driven outflows can also push gas entirely beyond the halo R_{200}, which both prevents re-accretion and suppresses the halo baryon fraction. Black hole feedback switches from thermal to kinetic mode as a function of the BH accretion rate, which is proportional to the black hole mass (see §2.1 of Weinberger et al. 2017).

Supernova feedback

The other key process which affects star formation, particularly for lower mass star-forming galaxies, is supernova feedback. In the TNG model, supernovae launch galactic winds from the dense interstellar medium (ISM), and these winds are modelled as collisionless particles ejected from star-forming gas cells, where the rate of total energy released from each cell is proportional to its instantaneous star formation rate (Pillepich et al. 2018a). Wind particles are ejected in random directions and take their properties from the gas cell from which they are ejected. These outflows remove mass from the ISM (Nelson et al. 2019b), and as we show below, they can also push gas out of the dark matter halo itself, suppressing the halo baryon fraction.

Environmental effects

Hydrodynamical simulations such as IllustrisTNG self-consistently capture gas-dynamical processes including tidal and ram-pressure stripping, to the degree allowed by the numerical resolution. The strength of ram-pressure stripping, for instance, depends on the background gas density and so the efficiency of the process is modulated by the halo gas fraction. In contrast, these processes need to be explicitly added to semi-analytic models.

1.4   Environmental processes in galaxy evolution

As we discussed earlier, one fundamental aspect affecting the formation and evolution of galaxies is their environment (Boselli & Gavazzi 2006). Tidal and ram-pressure forces can strip both star-forming gas in the disk and the hot halo gas around galaxies in dense environments (Gunn & Gott 1972; Binney & Tremaine 1987). The impact of stripping on the star formation rates, colours, stellar masses, and gas contents of galaxies as a function of environment can now be quantified in large galaxy samples as well as in highly resolved data across a range of observational tracers (Jaffé et al. 2015; Poggianti et al. 2017; Boselli et al. 2018).

On the theoretical side, the treatment of many of these environmental processes in hydrodynamical simulations occurs as a result of solving the equations of gravity, (magneto)hydrodynamics, and as heating and cooling together, allowing the direct modelling of both dark and baryonic matter (Hernquist & Katz 1989; Springel 2010; Crain et al. 2015). The strength of ram-pressure stripping, for instance, depends on the background gas density and so the efficiency of the process is modulated by the halo gas fraction. These processes have been studied with idealized hydrodynamical simulation of satellite galaxies (Roediger & Brüggen 2007; Bekki 2009; Tonnesen & Bryan 2009; Vijayaraghavan & Ricker 2017). It is also now possible to directly study gas stripping phenomena in the full cosmological context with simulations such as IllustrisTNG (Yun et al. 2019), in addition to the environmental impact on the gas contents of satellite galaxies more generally (Sales et al. 2015; Bahé et al. 2017; Wang et al. 2018b; Stevens et al. 2019).

As there is no hydrodynamical interaction in the DMO simulations on which semi-analytical models are implemented, baryonic environmental processes do not occur naturally in SAMs. Therefore, they need to be modelled explicitly using analytical approximations. Early semi-analytic models assumed that hot gas was stripped out of galaxies immediately after infall into the parent halo (Kauffmann et al. 1993; De Lucia et al. 2006). The GALFORM (Lacey et al. 2016) and SHARK (Lagos et al. 2018) SAMs also include instantaneous stripping for the hot gas component of satellite galaxies, whereas Font et al. (2008) formulated a gradual ram-pressure stripping (RPS) process informed by hydrodynamical simulations for GALFORM. In such models there is no post-infall gas accretion onto satellites, although cold star-forming gas can continue to form stars until the galaxy eventually exhausts this reservoir (Larson et al. 1980).

In addition to ram-pressure stripping, SAMs including SAGE (Croton et al. 2016) and DARK SAGE (Stevens et al. 2016a) have also applied tidal stripping to the hot gas of satellite galaxies, an effect which we note is usually weaker than ram-pressure. Tecce et al. (2010) implemented a method using gas particle data from a matched hydrodynamic simulation to estimate ram-pressure using the local density and velocity of the intracluster medium (ICM) environment through which satellite galaxies move. The SAG semi-analytical model (Cora et al. 2018) has both tidal and ram-pressure stripping for hot gas. They use the RPS method introduced in McCarthy et al. (2008) and a fit to ram-pressure in a particular hydrodynamic simulation based on the work of Tecce et al. (2010) as a function of halo-centric distance, halo mass and redshift for satellite galaxies. Comparing

to the RPS method of Cora et al. (2018), the method we will introduce in this thesis makes fewer model assumptions and can be applied uniformly and locally to all galaxies, not just satellites, but at the expense of the strong assumption that the background gas and dark matter parallel each other. Some SAMs also consider RPS of the cold gas content of galaxies (Luo et al. 2016; Stevens et al. 2016a; Cora et al. 2018).

Recent versions of the L-Galaxies model have prescriptions for both time-evolving tidal and ram-pressure stripping of the gas within subhaloes (Guo et al. 2011). An accurate model for the tidal and ram-pressure stripping of satellite galaxies requires accurate dark matter and gas profiles, such that background gas densities, as well as the velocities of satellite galaxies relative to the background gas, can be estimated. The two latter quantities are usually approximated using the properties of the satellite galaxy's host halo (Henriques et al. 2017). Although correct to first order, this precludes a treatment of gas stripping effects which depends on local gas inhomogeneities and structure within a host halo, as well as the stripping of central galaxies passing through cosmic environments such as filaments or sheets (Aragon-Calvo et al. 2016; Kraljic et al. 2018).

The scales over which environment influences the properties of galaxies are also still a matter of discussion. Most semi-analytical models of galaxy formation and evolution, including L-Galaxies, adopt R_{vir}, the virial radius, or R_{200}, the radius within which the matter density equals 200 times the critical density of the Universe, as the boundary for the dark matter halo and its hot gas component. In the modelling, this spatial edge acts as a sharp threshold for cutting-off environmental effects, which is clearly an oversimplified assumption. It has been noted for instance that the 'splashback radius' may be a more physical boundary for a dark matter halo, as it corresponds to the radius at which accreted matter reaches its first orbital apocenter after turnaround. Depending on the accretion rate, the splashback radius ranges from slightly smaller than R_{vir} to $\approx 1.5R_{\mathrm{vir}}$ (Diemer & Kravtsov 2014; Adhikari et al. 2014; More et al. 2015). Hydrodynamical simulations suggest that the shock-heated gas of a dark matter halo extends beyond its virial radius, up to $2-3R_{\mathrm{vir}}$ depending on halo mass (Nelson et al. 2016; Zinger et al. 2018).

There have been several observational (Hansen et al. 2009; von der Linden et al. 2010; Lu et al. 2012) and theoretical (Balogh et al. 1999; Bahé et al. 2012) studies showing that the environmental effects might extend well beyond the virial radius or similar halo boundaries. A large scale correlation between the star formation of neighboring galaxies out to distances as large as 10 Mpc has also been observed, known as the problem of galactic conformity (Weinmann et al. 2006; Kauffmann et al. 2013; Kauffmann 2015; Hearin et al. 2016; Hatfield & Jarvis 2017; Treyer et al. 2018). To capture such physical effects, a realistic semi-analytic galaxy model needs to contain prescriptions for environmental effects which are *local*, and which avoid artificial boundaries.

In this thesis we measure local properties in the immediate vicinity of galaxies, namely background density and bulk velocity. We use this local background environment (LBE) to devise a more realistic treatment of ram-pressure stripping in the L-Galaxies Semi-analytical model. We also investigate a variety of background properties using our LBE technique and particle data from the Millennium and Millennium-II simulations.

1.5   This Thesis

This study aims to improve our understanding of the environmental dependency of galaxy evolution, especially the extension of environmental processes to large-scales. This thesis is based on three papers (Ayromlou et al. 2019, 2021a,b) and is structured as follows: In Chapter 2, we perform a comparison, object-by-object and statistically, between the Munich semi-analytical model, L-Galaxies, and the IllustrisTNG hydrodynamical simulations. By running L-Galaxies on the IllustrisTNG dark matter-only merger trees, we identify the same galaxies in the two models. This allows us to compare the stellar mass, star formation rate, and gas content of galaxies, as well as the baryonic content of subhaloes and haloes in the two models. Particularly, we focus on the environmental dependency of galaxy evolution. We study the gas content and star formation rates of galaxies in and around clusters and groups, and investigate the influence of environmental processes such as ram-pressure stripping on galaxy evolution in the two models.

In Chapter 3, we introduce a Local Background Environment (LBE) estimator that can be measured in and around every galaxy or its dark matter subhalo in high-resolution cosmological simulations. The LBE is designed to capture the influence of environmental effects such as ram-pressure stripping on the formation and evolution of galaxies in semi-analytical models. We define the LBE directly from the particle data within an adaptive spherical shell, and devise a Gaussian mixture estimator to separate background particles from previously unidentified subhalo particles. We then analyse the LBE properties and use the LBE measurements to model ram-pressure within the L-Galaxies semi-analytical model.

In Chapter 4 we present a variation of the recently updated Munich semi-analytical galaxy formation model, L-Galaxies, with our new gas stripping method. We fully re-calibrate the modified L-Galaxies model using a Markov Chain Monte Carlo (MCMC) method with the stellar mass function and quenched fraction of galaxies at $0 \leq z \leq 2$ as observational constraints. On the observational side, we undertake a new analysis inferring the quenched fraction versus halocentric distance out to $R_{\mathrm{proj}} = 10R_{200}$ with a methodology consistent between simulations and data. Finally, we compare our model's predictions with observations and conclude our study.

Chapter 2

Comparing galaxy formation models

2.1   Introduction

The treatment of gas is one of the fundamental differences between hydrodynamical simulations and semi-analytical models (SAMs). In a hydrodynamical simulation the cosmic baryon fluid is modelled through a numerical, discretised solution to the equations of (magneto)hydrodynamics. Therefore, the distribution of gas mass and its thermodynamical properties is a direct outcome of the simulation.

On the other hand, in a semi-analytical model, gas is partitioned into several discrete components such as the hot, cold and ejected reservoirs. Mass is exchanged between these components, but its spatial distribution (and other properties, such as temperature or kinematic structure) is unspecified, and must be derived from simplified models if required (Henriques et al. 2013; Yates et al. 2017). Recently, semi-analytical models have begun to spatially resolve galaxies by discretising their gas and stellar discs into radial rings (Henriques et al. 2020), probing down to sub-kpc scales (see also Stringer & Benson 2007; Fu et al. 2013; Stevens et al. 2016b).

The drawback of hydrodynamical simulations is their computational expense, and large projects such as IllustrisTNG can take tens of millions of CPU cores hours to complete (see e.g. Nelson et al. 2019b). In contrast, SAMs are computationally much less expensive, typically orders of magnitude faster than hydrodynamical simulations. Given their relative strengths and weaknesses, it is useful to compare and contrast their results in order to make simultaneous improvements on both techniques.

These two approaches to modelling galaxies have been compared in the past. Yoshida et al. (2002) contrast the cooling of gas and its condensation into galaxies between a SAM and a hydrodynamic simulation using the smoothed particle hydrodynamics (SPH) technique (see also Helly et al. 2003). In addition, Saro et al. (2010) compare galaxies formed within a massive cluster using both the semi-analytic and hydrodynamic approaches, finding statistically similar results, but significant differences on an object-by-object level, particularly for the star formation history of the central galaxy.

Most similar to our study, Guo et al. (2016) (hereafter G16) compare global statistical

properties of the Guo et al. (2013) version of L-Galaxies, and the Gonzalez-Perez et al. (2014) version of the Galform SAM, with the Eagle hydrodynamical simulation (Schaye et al. 2015). They find that statistical properties such as stellar mass functions and star formation rates are similar while galaxy sizes are significantly different. Mitchell et al. (2018) (hereafter M18) continue this work by comparing Galform with Eagle, focusing on baryon cycling, angular momentum and feedback. They also perform an object-by-object study of the stellar masses of galaxies between these models, as a function of stellar mass and star formation history. They find that overall, Eagle produces more realistic results when compared to observations, motivating key improvements to Galform.

Similarly, Wang et al. (2018a) compare the star formation quenching from observations with the Henriques et al. (2015) version of the L-Galaxies SAM and the Eagle hydrodynamical simulation. In addition, Wang et al. (2019) compare galaxy morphologies between the Illustris simulation (Vogelsberger et al. 2014; Genel et al. 2014) and the Guo et al. (2011) version of L-Galaxies, finding that late type galaxies are broadly similar, whereas early types exhibit larger differences. Finally, Renneby et al. (2020) compare galaxy-galaxy lensing profiles and clustering between the L-Galaxies SAM (Henriques et al. 2015) and the IllustrisTNG simulation.

In this chapter, we perform a comparison between the Henriques et al. (2015) version of the L-Galaxies semi-analytical model and IllustrisTNG magnetohydrodynamic simulation. We run the L-Galaxies model on merger trees taken from the IllustrisTNG simulation and our analysis is based on the comparison of physical quantities of the same, matched set of haloes and subhaloes. This enables us to understand their similarities and differences not only statistically, but also on an object-by-object basis. This chapter focuses on implications for the physical processes and methods employed in the L-Galaxies and IllustrisTNG models, rather than on a detailed comparison to observational data. Our comparison is divided into two parts: (i) a study of the general properties of galaxies and (ii) an investigation of their environmental dependence. Previous papers have compared the general properties of galaxies in other semi-analytical and hydrodynamical model pairings (see e.g. Guo et al. 2016; Mitchell et al. 2018). The study we present here is novel in its focus on the environmental dependence of galaxy evolution.

This chapter is structured as follows: In §2.2 we describe our method to match galaxies and haloes between the two models. In §2.3 we compare, object-by-object and statistically, several properties of galaxies and haloes produced by L-Galaxies and IllustrisTNG. Section §2.4 is dedicated to a comparison of the role of environment in galaxy evolution in the two models. Finally, we summarise and discuss our results in §2.5.

2.2 Matching galaxies between the models

Object-by-object matching

We aim to make an object-by-object comparison between L-Galaxies and TNG by running L-Galaxies on the TNG-DMO simulations. These have the same initial conditions

Table 2.1: The numbers of subhaloes, galaxies and the fraction of systems matched between the IllustrisTNG simulations and the L-Galaxies runs on the corresponding DMO volumes. Subhaloes in our mass range of interest are almost always matched. On the other hand, orphan galaxies in the L-Galaxies do not reside in subhaloes, and we do not attempt to match these to existent TNG subhaloes, bringing down the matched percentages for less luminous galaxies.

Model	L-GALAXIES (TNG300-DMO)	TNG300 (Hydrodynamic)	L-GALAXIES (TNG100-DMO)	TNG100 (Hydrodynamic)
N_{sub} (SUBFIND)	154469 ($M_{\mathrm{s}}/\mathrm{M}_\odot > 10^{11.5}$)	145451 ($M_{\mathrm{s}}/\mathrm{M}_\odot > 10^{11.5}$)	61263 ($M_{\mathrm{s}}/\mathrm{M}_\odot > 10^{10.5}$)	52335 ($M_{\mathrm{s}}/\mathrm{M}_\odot > 10^{10.5}$)
Matched Fraction	$\sim 98.4\%$	$\sim 98.1\%$	$\sim 97.3\%$	$\sim 97.3\%$
N_{gal}	211511 ($M_\star/\mathrm{M}_\odot > 10^{9.5}$)	158112 ($M_\star/\mathrm{M}_\odot > 10^{9.5}$)	28196 ($M_\star/\mathrm{M}_\odot > 10^{8.5}$)	33677 ($M_\star/\mathrm{M}_\odot > 10^{8.5}$)
Matched Fraction	$\sim 81.3\%$	$\sim 83.7\%$	$\sim 77.5\%$	$\sim 76.4\%$

(i.e. phases) as the full hydrodynamical simulations, producing very nearly the same dark matter halo populations.

We then match subhaloes between the baryonic and DMO simulations following Nelson et al. (2015), using the LHALOTREE algorithm. By comparing unique dark matter particle IDs, matched subhaloes are defined as those with the highest fractions of common particles. The match must be bidirectional, i.e. the same starting from either of the two runs. When necessary, FOF haloes are matched based on their central subhalo[1].

The subhalo matching catalogue also provides, by definition, a matching of the galaxies which reside in those subhaloes. The notable exception is for orphan galaxies, which are not hosted by identifiable dark matter subhaloes. However, unmatched galaxies/subhaloes are usually low mass and form a small fraction of the objects in our stellar mass range of interest. The number of subhaloes, galaxies and the corresponding matched fractions are given in Table 2.1; the great majority of subhaloes are successfully matched. We perform two kinds of analysis in this chapter: i) statistical and ii) object-by-object. For the statistical analyses (e.g. stellar mass functions) we use all subhaloes/galaxies, while for the object-by-object analyses (e.g. the ratio of the stellar masses) we consider only successfully matched objects.

Combining the 100 Mpc and 300 Mpc boxes

We have analysed both the $(300\,\mathrm{Mpc})^3$ and $(100\,\mathrm{Mpc})^3$ simulation boxes, although we often focus on just the one most appropriate for the aspect of the galaxy population being studied. In practice, we compare TNG300 with L-GALAXIES run on TNG300-DMO

---

[1]The catalogue of L-Galaxies run on TNG-DMO is publicly available at www.tng-project.org/ayromlou20.

(hereafter LGal300) and we compare TNG100 with L-GALAXIES run on TNG100-DMO (hereafter LGal100). The 300 Mpc box provides better statistics for massive dark matter haloes, while the 100 Mpc box has a higher resolution. When we combine the results of these two boxes, we have verified that the resolution difference does not introduce any biases in our interpretation.

The quantitative results of the TNG model depend on resolution. In particular, the stellar masses of galaxies at $z = 0$ are roughly 40% higher, at fixed total halo mass, in the higher resolution TNG100 as compared to TNG300 (Pillepich et al. 2018b). It can be useful to re-scale stellar masses to compensate for the lower resolution of the TNG300 simulation (labelled 'rTNG300'). We do so only in Fig. 2.2, for stellar mass functions and stellar mass to halo mass ratios. We follow the method of Pillepich et al. (2018b) and derive a correction factor equal to the ratio of TNG100 to TNG100-2[2] stellar mass in bins of fixed halo mass. On average this multiplicative correction factor is ~ 1.4 at $z = 0$, and lower at higher redshifts. For simplicity, we avoid re-scaling stellar masses in any other case, and likewise do not re-scale any other properties of galaxies. A similar step is not required for L-GALAXIES since stellar masses are converged over the mass range of interest (see Guo et al. 2011).

Deriving galaxy properties

Because of finite numerical resolution, care is needed to compare some galaxy properties. We enforce a minimum for the star formation rates (SFR) of galaxies, choosing $\mathrm{SFR_{min}} = 10^{-3} \mathrm{M_\odot yr^{-1}}$. This allows us to analyse galaxies with zero star formation rate, which occurs in hydrodynamical simulations below some resolution-dependent threshold (Donnari et al. 2019). The value of $\mathrm{SFR_{min}}$ ensures that for galaxies with $\log_{10}(M_\star/\mathrm{M_\odot}) > 8$ the quenched fraction is unaffected, as galaxies with $\log_{10}(\mathrm{sSFR/yr^{-1}}) < -11$ are considered as quenched at $z = 0$. A limit is also imposed for gas masses at $\log_{10}(M_{\mathrm{gas,min}}/\mathrm{M_\odot}) = 5$ which similarly allows us to include very gas-poor objects without biasing our results.

In the L-GALAXIES model calibration, a random Gaussian centred at zero with $\sigma = 0.08\,(1 + z)$ is added to all the logarithmic stellar masses when comparing to data (see Fig. 2 of Henriques et al. 2015). This accounts for the uncertainties in observational stellar mass determinations (also see D'Souza et al. 2015; Ilbert et al. 2013). In this chapter, we apply this modification when plotting the stellar mass functions both for L-GALAXIES and TNG in the top panel of Fig. 2.2 in order to facilitate comparison with the observations. Elsewhere in this chapter we use stellar masses as given by the theoretical models without modification.

Throughout, unless stated otherwise, we take the stellar mass definition to be the subhalo stellar mass (in the case of L-GALAXIES) or the stellar mass within twice the stellar half-mass radius (for TNG). The M_{200} (M_{500}) of a FOF halo is the total mass within the R_{200} (R_{500}) of the halo, the radius within which the matter density equals 200 (500) times the critical density of the Universe.

---

[2]The TNG100-2 is a TNG simulation with resolution equal to TNG300 but performed in a 100 Mpc box.

Complications with orphan galaxies

As discussed in §1.2.2, in many semi-analytical models, including L-GALAXIES, an 'orphan' galaxy is defined to be one without an identified subhalo, i.e., it previously had a subhalo, which has dropped below the simulation resolution due to tidal disruption. L-GALAXIES traces the evolution of orphan galaxies, and their positions and velocities using the current positions and velocities of the most bound particle of their former subhaloes. This requires giving those positions and velocities as an input to the model. These were traced and stored for the Millennium and Millennium-II simulations but not for the TNG-DMO. Therefore, in our analysis, wherever we need the positions of orphan galaxies, we use L-Galaxies run on the Millennium simulation. This is only the case for the top panels of Figures 2.11 and 2.13. In all other cases L-Galaxies run on TNG-DMO is employed and orphans can be included as normal since their positions and velocities are not required. We note that the Millennium simulation used here is re-scaled to the Planck cosmology (see Angulo & White 2010; Angulo & Hilbert 2015; Henriques et al. 2015).

2.3 General properties of galaxies and haloes

We begin by comparing the properties of galaxies and haloes[3] between TNG and L-GALAXIES. To give a visual overview, Fig. 2.1 illustrates the distribution of galaxies in a 10 Mpc thick slice of the 100 Mpc box, as simulated by the L-GALAXIES (left column) and TNG (right column) models. Qualitatively, the overall cosmic web structure is nearly identical in the two plots and the predicted stellar masses are very similar (the top panels). On the other hand, the specific star formation rates (sSFR = SFR/$M_\star$, bottom panel) start to exhibit differences. Particularly in nodes where filaments come together, the sites of massive groups and clusters, galaxies are overall less star-forming in TNG.

2.3.1 Comparing stellar masses

We start with a quantitative comparison of the stellar content of galaxies in L-GALAXIES and TNG. The top panels of Fig. 2.2 show stellar mass functions from the two models at redshifts $z = 0$ and $z = 2$. We consider two definitions of galaxy stellar mass for the TNG galaxies at $z = 0$. The first is the stellar mass within twice the half-stellar-mass-radius, $R < 2R_{\rm star,1/2}$, and the second is the stellar mass within 30 physical kiloparsecs, $R < 30$ pkpc. For L-GALAXIES, we show both galaxy and subhalo stellar masses.

Regardless of the redshift, the stellar mass functions of L-GALAXIES and TNG agree relatively well with each other and with observations. Both models attempt to calibrate their free parameters to fit the observed stellar mass function at $z = 0$ (L-GALAXIES also

---

[3]We note that baryonic physics leads to small changes in the total mass of subhaloes, but this has a negligible impact on our analyses. For instance, Springel et al. (2018) shows that halo masses (M_{200}) are up to 20 per cent lower in baryonic versus DMO runs. We similarly find that subhalo masses are usually smaller in the hydrodynamical run, by twenty percent or less, depending on the subhalo mass, with a typical scatter of $0.1 - 0.2$ dex.
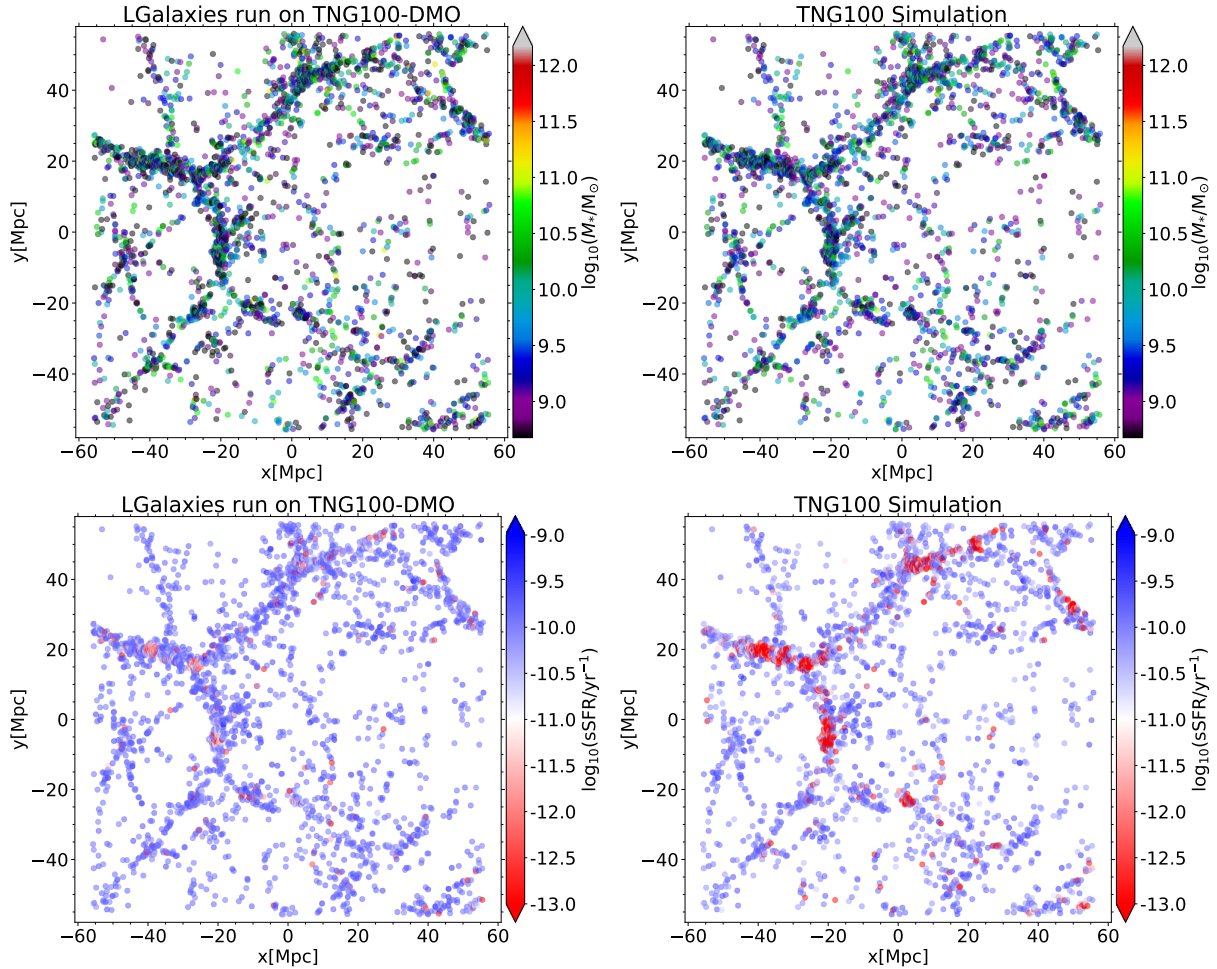
Figure 2.1: Visual overview of galaxy properties, comparing the results of L-Galaxies (left columns) versus TNG100 (right columns) at $z = 0$. We project the 100 Mpc simulation volume through a depth of 10 Mpc, and each circle corresponds to a galaxy. The colour shows galaxy stellar mass (top panels) or specific star formation rate (bottom panels). In the bottom panel, systems are separated based on sSFR, where galaxies with $\log_{10}(\mathrm{sSFR}/\mathrm{yr}^{-1}) > -11$ are considered as star-forming and are shown in blue, while galaxies with $\log_{10}(\mathrm{sSFR}/\mathrm{yr}^{-1}) < -11$ are considered to be quenched and are shown in red.
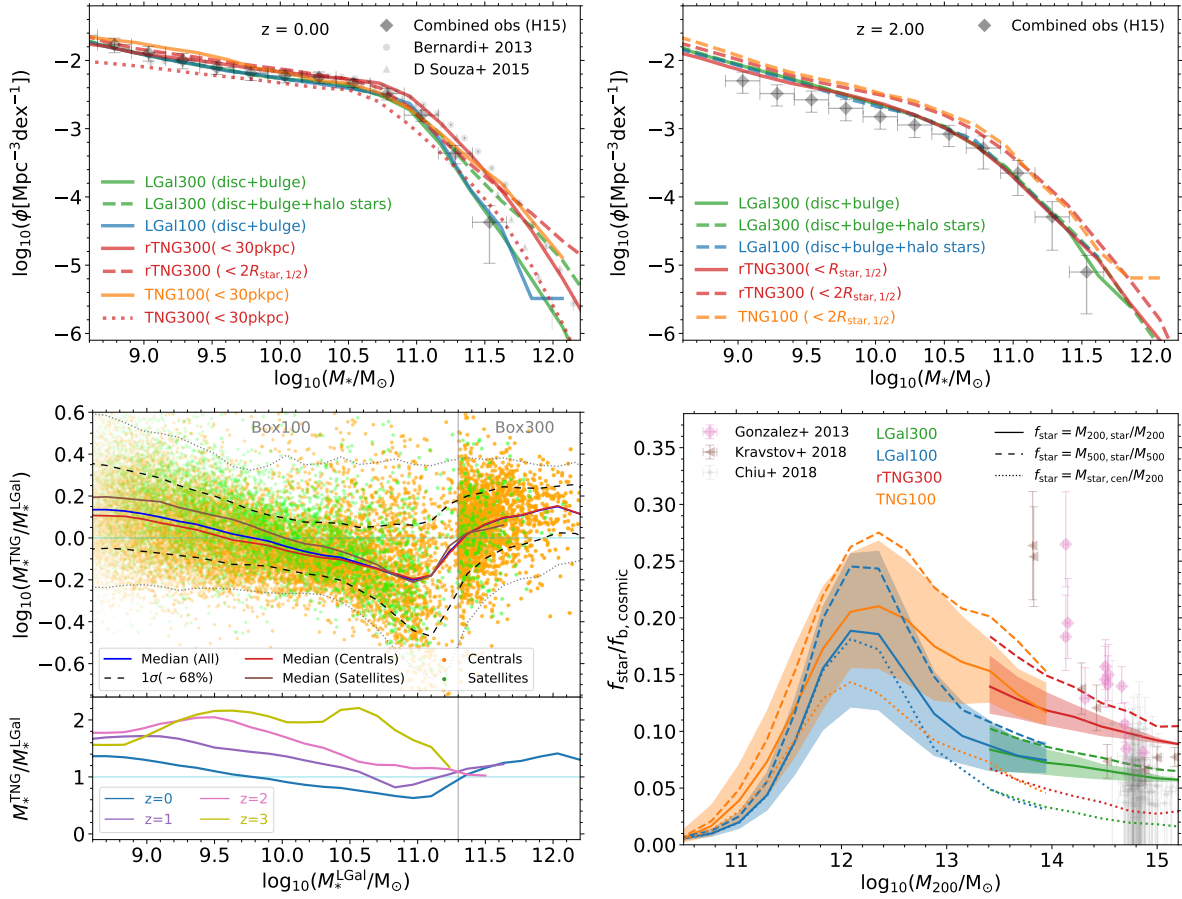
Figure 2.2: The top panels show the stellar mass functions from L-GALAXIES and TNG at $z = 0$ and $z = 2$. Observational data are taken from Baldry et al. (2008, 2012); Li & White (2009) (together labelled as "Combined obs", used in H15), and Bernardi et al. (2013); D'Souza et al. (2015) for $z = 0$ and Marchesini et al. (2009, 2010); Ilbert et al. (2010, 2013); Domínguez Sánchez et al. (2011); Muzzin et al. (2013); Tomczak et al. (2014) (together labelled as "Combined obs", used in H15) for $z = 2$. Solid, dashed and dotted lines correspond to different definitions of stellar mass (see the legends). The bottom left panel shows the object-by-object ratio of TNG stellar masses to L-GALAXIES stellar masses. Here we use the subhalo stellar mass for L-GALAXIES and the stellar mass within twice the half stellar mass radius in TNG (dashed lines in the top panel). Each dot corresponds to one galaxy, where centrals and satellites are orange and green, respectively. The dashed and dotted lines show the 1σ and 2σ scatter of the distribution. The lower sub-panel shows the median relations at different redshifts. The bottom right panel shows the ratio of stellar mass to halo mass (normalised by the cosmic baryon fraction). The solid and dashed lines correspond to SMHM ratio within R_{200} and R_{500}, respectively. The dotted line shows the ratio of the stellar mass of the central galaxy to its host halo M_{200}. The shaded regions correspond to the 1σ scatter for the SMHM ratio within R_{200}. Observational data are taken from Gonzalez et al. (2013); Kravtsov et al. (2018); Chiu et al. (2018) and show f_{star} within R_{500} (to be compared with dashed lines). The 'rTNG300' curves are re-scaled TNG values (see §2.2).

uses data at $z = 0, 1, 2, 3$). As a result, it is not surprising that they are broadly consistent with the data at $z = 0$, and the agreement at other redshifts is similarly good. At the high mass end, $\log_{10}(M_\star/\mathrm{M}_\odot) \gtrsim 11$, the definition of stellar mass starts to become critical, as galaxy sizes increase and more stars are found in the extended intracluster component of haloes. In all models, definitions which integrate to larger apertures produce a shallower high-mass end of the SMF (red dashed line above red solid; green dashed above green solid). Whereas L-Galaxies SMFs are consistent between resolutions, modulo box volume effects (green versus blue solid lines), the TNG100 SMF is above the TNG300 due to resolution convergence (orange solid line versus red dotted line), but in agreement with rTNG300 (red dotted line; see Pillepich et al. 2018b). Overall, the agreement between the two models is statistical, and does not necessarily imply that the stellar masses of individual objects also agree.

We therefore compare at the object-by-object level, contrasting model predictions for the stellar masses of individual galaxies. The results are given in the bottom left panel of Fig. 2.2, where we show the ratio of stellar masses between the two models, for matched galaxies, at $z = 0$. Each dot corresponds to a galaxy; centrals and satellites are shown with orange and green dots, respectively. The sub-panel shows the redshift evolution of the median relation since $z = 3$, in linear units. There is remarkably good agreement between the stellar masses of individual objects since $z = 3$. At $z = 0$, the median rarely differs from unity by more than 40%, which is relatively small considering the wide range of stellar masses we consider and the differences in the physical recipes and general approach used in each model. In addition, the 1σ scatter of the distributions (dashed lines) is typically smaller than $0.2 - 0.3$ dex. We find that the scatter decreases with redshift, from ~ 0.1 dex at $z = 3$ to ~ 0.2 dex by $z = 0$ (not shown). The median line at $z = 0$ shows that for both low and high stellar mass ranges, i.e. $\log_{10}(M_\star/\mathrm{M}_\odot) \lesssim 10$ and $\log_{10}(M_\star/\mathrm{M}_\odot) \gtrsim 11.5$ TNG predicts higher stellar masses, while for the intermediate stellar mass range, $10 \lesssim \log_{10}(M_\star/\mathrm{M}_\odot) \lesssim 11.5$, L-Galaxies produces more stars.

We have also plotted medians of central (red solid lines) and satellite galaxies (brown solid lines). Satellite galaxies are more sensitive to the difference in physical prescriptions between models, and in general their ratio $M_\star^{\mathrm{TNG}}/M_\star^{\mathrm{LGal}}$ is larger than for centrals.

To compare the star formation efficiency between L-Galaxies and TNG haloes, the bottom right panel of Fig. 2.2 shows the fraction of stars within haloes – the stellar mass to halo mass (SMHM) ratio. Solid lines indicate the median stellar-to-total mass ratio within R_{200}, normalised by the cosmic baryon fraction, while the 1σ scatter is shown as shaded regions. The dashed lines correspond to the same quantity, measured with respect to R_{500} and M_{500} instead. Finally, the ratio of the stellar masses of central galaxies (i.e. excluding halo stars) to M_{200} are shown as dotted lines.

In general, for haloes with $\log_{10}(M_{200}/\mathrm{M}_\odot) \gtrsim 10.5$, TNG has a higher $f_{\mathrm{star}}/f_{\mathrm{b,cosmic}}$ than L-Galaxies, and this is true both within R_{200} and R_{500}. Nevertheless, the difference between TNG and L-Galaxies is always less than a factor of two. The model predictions fall on top of each other at low-mass, but are much more discrepant at high mass. They overlap at $\log_{10}(M_{200}/\mathrm{M}_\odot) \lesssim 13$, but even the 2σ scatter is disjoint for clusters with $\log_{10}(M_{200}/\mathrm{M}_\odot) \gtrsim 14$.

In this panel we also include several observational datasets for comparison. Gonzalez et al. (2013) and Kravtsov et al. (2018) provide the total stellar mass within R_{500}, and so are comparable with the dashed lines from the simulations. In addition, Chiu et al. (2018) measures the ratio of stellar mass of the central galaxy versus host halo M_{500}, and should be compared with the dotted lines. As we report SMHM ratio as a function of M_{200}, any M_{500} values are converted to M_{200} using the ratio of these two quantities from TNG. This only shifts the x-axis values, leaving the SMHM ratios on the y-axis unchanged. The results from L-GALAXIES are in better agreement with Kravtsov et al. (2018), while the results from TNG are in a better agreement with Gonzalez et al. (2013). Both models agree reasonably well with Chiu et al. (2018). We note that the scatter between different observations is much larger than the intrinsic scatter in either model.

In previous work, G16 compared the stellar mass functions of the EAGLE simulation with the GALFORM and L-GALAXIES SAMs, finding relatively good agreement at $z \leq 2$. M18 compared stellar masses in EAGLE and GALFORM, object-by-object, finding that they agree with a scatter of $1\sigma \sim 0.37$ dex in the ratio between the stellar masses of the two models at $z = 0$ (and with smaller scatter at higher redshifts). This is larger than the 1σ scatter of about 0.2 dex that we found for the ratio between the stellar masses of TNG and L-GALAXIES in the bottom left panel of Fig. 2.2. Finally, both G16 and M18 analyse the stellar mass (of central galaxies) to halo mass relation, finding that EAGLE, GALFORM and L-GALAXIES are in agreement but GALFORM has a larger scatter due to the particulars of its black hole feedback recipe.

2.3.2 Galaxy star formation activity

Although L-GALAXIES and TNG galaxies have similar stellar masses, these models have different star formation rates at $z = 0$. Fig. 2.3 shows the density of galaxies in terms of star formation rate as a function of stellar mass, for L-GALAXIES (top panel) and TNG (bottom panel). The star formation main sequence can be seen in both models, in qualitative agreement with observations (Elbaz et al. 2007). Overall, main-sequence TNG galaxies are somewhat less star-forming than in L-GALAXIES, by a factor of ~ 0.1 dex. TNG also has more rare and outlying systems, such as low mass galaxies with high star formation rates, and very massive galaxies with remaining, residual star formation.

Specific star formation rates

The upper panel of Fig. 2.4 illustrates the ratio of sSFR between TNG and L-GALAXIES for individual galaxies, as a function of stellar mass at $z = 0$. The lower sub-panel again shows the redshift evolution of the median relations, for $0 < z < 3$. At $z = 0$, there are three distinct regimes: low-mass galaxies with $\log_{10}(M_\star/\mathrm{M}_\odot) \lesssim 10.5$, intermediate-mass galaxies with $10.5 \lesssim \log_{10}(M_\star/\mathrm{M}_\odot) \lesssim 11.2$, and massive galaxies with $\log_{10}(M_\star/\mathrm{M}_\odot) \gtrsim 11.2$. The sSFRs of the first and the third sets of galaxies, i.e. low-mass and high-mass, are in reasonable agreement at a level of better than 0.3 dex, depending on the stellar mass. The
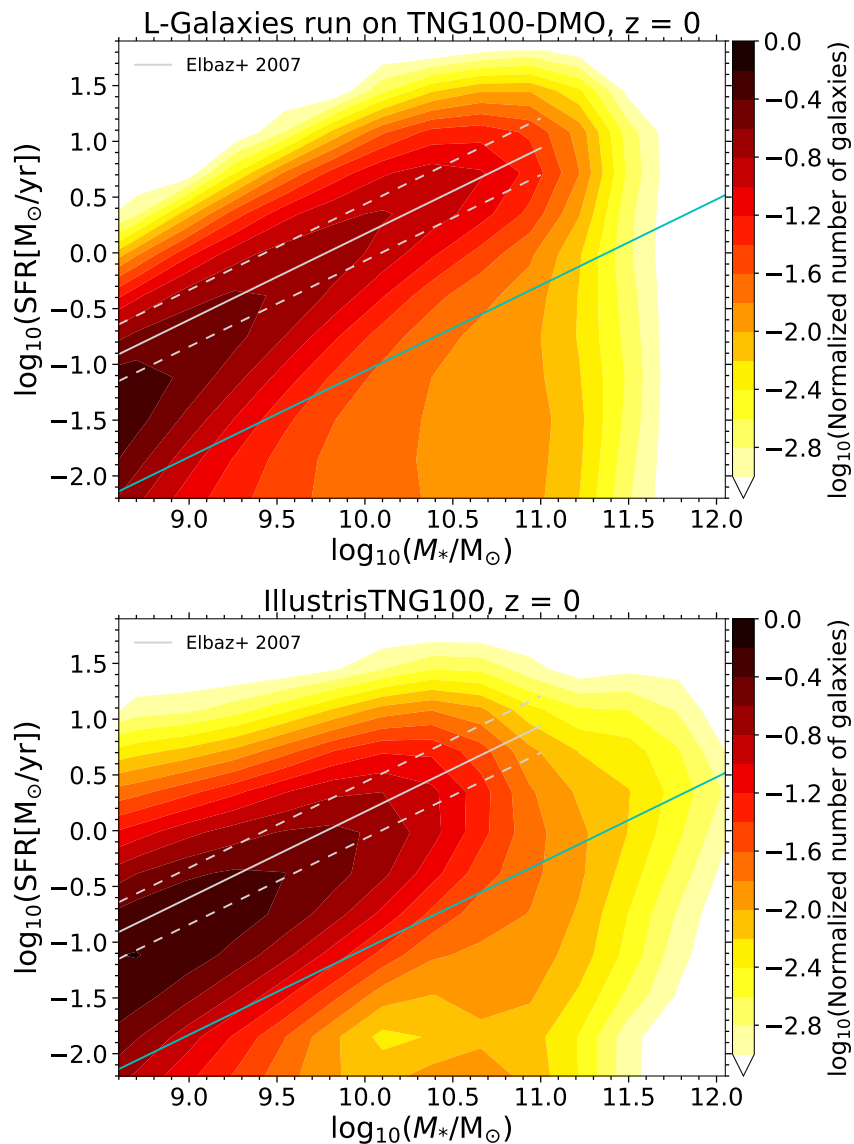
Figure 2.3: Occupation of the SFR-stellar mass plane by galaxies produced in L-Galaxies (top) and TNG100 (bottom) at $z = 0$. Colours illustrate contour levels, normalised to the maximum number of galaxies found in a bin. The solid and dashed gray lines correspond to the median and 1σ scatter of the main sequence of star-forming galaxies by Elbaz et al. (2007) from SDSS data. For reference, the solid green lines are 1 dex below the main sequence, a possible definition of quiescence.
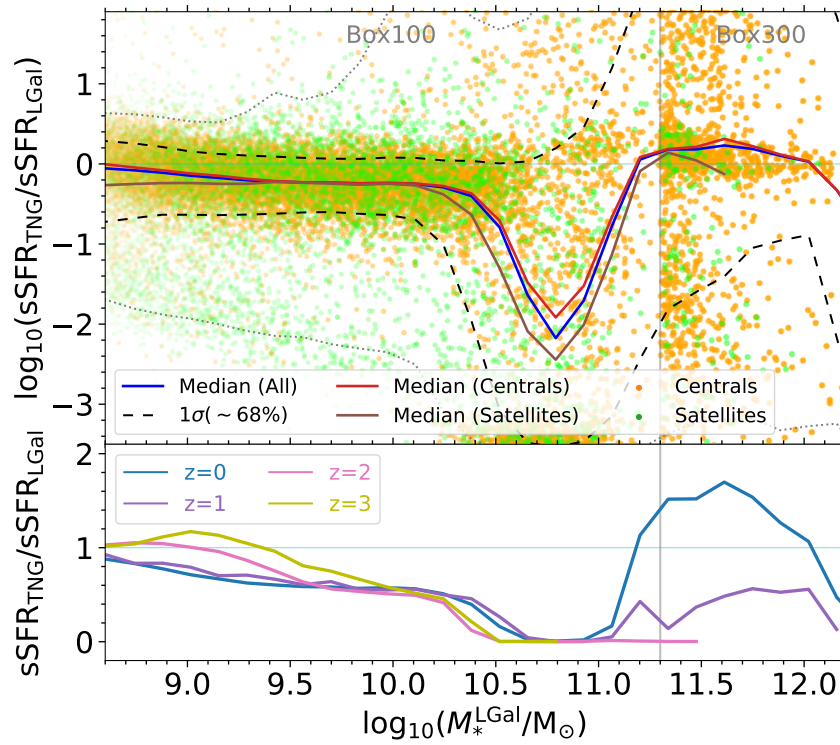
Figure 2.4: The ratio of specific star formation rates for galaxies in TNG and L-Galaxies. The top panel shows the object-by-object ratio at $z = 0$. Each dot corresponds to one galaxy, where centrals and satellites are shown as orange and green dots, respectively. The blue solid line gives the median relation for all galaxies, while red and brown solid lines show medians for central and satellite galaxies alone. In addition, the dashed and dotted lines indicate the 1σ and 2σ scatter. The lower sub-panel shows median lines at different redshifts in linear units.

1σ of scatter of the distribution (dashes lines) is $0.2 - 0.3$ dex for the low-mass galaxies but larger for the massive systems.

On the other hand, the sSFRs of intermediate-mass galaxies differ substantially between L-Galaxies and TNG. Intermediate-mass galaxies are mostly quenched in TNG while a large fraction of them are still star-forming in L-Galaxies. This is caused primarily by differences in the implementation of SMBH feedback in the two models, namely the mass scale where strong feedback begins to quench galaxies. In TNG this occurs at $\log_{10}(M_\star/M_\odot) \sim 10.5$, while in L-Galaxies quenching via AGN happens at characteristically higher stellar masses, $\log_{10}(M_\star/M_\odot) \sim 11$.

The sSFR ratio between the models has a weak trend with redshift, as seen in the lower part of Fig. 2.4. The ratio $\mathrm{sSFR}^{\mathrm{TNG}}/\mathrm{sSFR}^{\mathrm{LGal}}$ decreases with cosmic time for galaxies with $\log_{10}(M_\star/M_\odot) \leq 10$. This implies that low-mass TNG galaxies are initially slightly more star-forming and their star formation rates decrease with time more rapidly than in L-Galaxies. The same is not true for massive galaxies, which have lower SFRs in TNG at $z = 1$ but higher SFRs by $z = 0$.

To understand the star formation activity of galaxies in more detail, Fig. 2.5 shows sSFR histograms in six different stellar mass ranges, compared with observations from SDSS DR7 (Brinchmann et al. 2004). Observed galaxies with no emission lines are assigned a value of SFR based on SED fitting which brings uncertainties, especially when comparing with simulations (Donnari et al. 2020b). Some works modify the intrinsic SFRs of simulated galaxies to account for this issue (Henriques et al. 2015; Henriques et al. 2020), where the sSFRs of simulated galaxies with $\log_{10}(\mathrm{sSFR}/\mathrm{yr}^{-1}) < -12$ are modelled by a random Gaussian. However, since our focus here is to compare models with each other rather than with observations, we leave the SFRs of simulated galaxies unchanged but show the approximate region in which the observed sSFRs are uncertain (dashed black lines in Fig. 2.5, representing the SDSS sSFR histograms).

The joint distribution of $(\mathrm{SFR}, M_\star)$ is a stringent constraint on theory. Both models qualitatively reproduce trends seen in the SDSS data, where the main difference is in the transition from mostly star-forming to mostly quenched galaxies, which happens at lower mass in TNG than in L-Galaxies. More than half the galaxies in L-Galaxies are still actively star-forming at $10.5 < \log_{10}(M_\star/M_\odot) < 11$ and the population only becomes mostly quenched at $11 < \log_{10}(M_\star/M_\odot) < 11.5$. In contrast, there is a transition from star-forming to quenched in TNG over the range $10.0 < \log_{10}(M_\star/M_\odot) < 11$. In the middle of this regime the distribution of sSFRs becomes strongly bi-modal, as also seen in SDSS. The star-forming main sequence is narrower, spanning a smaller range of SFRs, in L-Galaxies than in TNG or in the observations, both of which favour a broader main sequence shifted to somewhat lower values of sSFR [4].
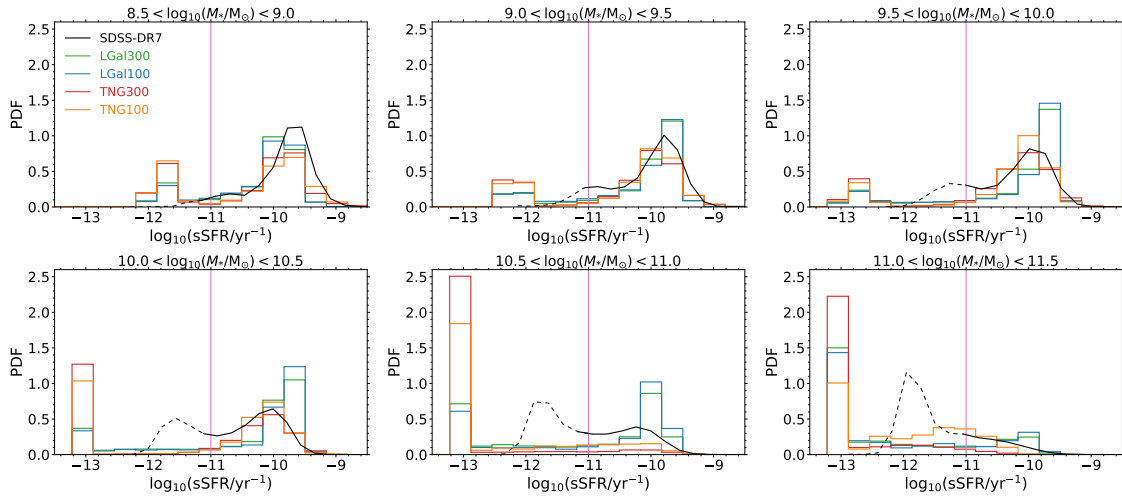
Figure 2.5: Histograms of sSFR for galaxies in L-GALAXIES, TNG, and observations. Each panel corresponds to a particular stellar mass interval. Note that a minimum value of SFR = 10^{-3}M$_\odot$/yr is enforced for the star formation rates of simulated galaxies (see §2.2 for more detail). SDSS data are taken from Henriques et al. (2015); Henriques et al. (2020) based on Brinchmann et al. (2004) with the corrections of Salim et al. (2007). The SDSS values for galaxies with low sSFR are shown with dashed lines, because observed galaxies with no emission lines are assigned a value for SFR based on SED fitting which cause uncertainties in the values of sSFR (see text). Galaxies with $\log_{10}(\text{sSFR/yr}^{-1}) < -11$ are quenched and this limit is shown by the vertical magenta lines. In every panel, all galaxies with zero SFR or with $\log_{10}(\text{sSFR/yr}^{-1}) < -13$ are assigned to the leftmost bin.
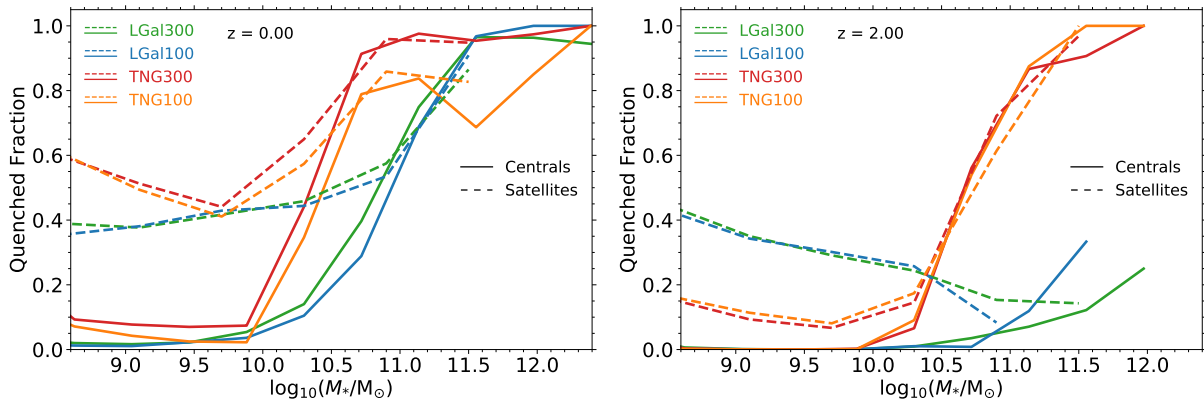
Figure 2.6: Fraction of quenched galaxies from L-GALAXIES and TNG simulations as a function of stellar mass, at $z = 0$ (left) and $z = 2$ (right). We adopt the definition that galaxies with $\log_{10}(\text{sSFR/yr}^{-1}) < -11$ and $\log_{10}(\text{sSFR/yr}^{-1}) < -10$ are considered as quenched at $z = 0$ and $z = 2$, respectively.

Fraction of quenched galaxies

Adopting definitions for quiescence based on galaxy sSFR, Fig. 2.6 shows the quenched fraction of galaxies as a function of stellar mass, at $z = 0$ (left) and $z = 2$. At $z = 0$ we consider galaxies quenched if $\log_{10}(\text{sSFR}/\text{yr}^{-1}) < -11$, while for $z = 2$ the threshold moves to $\log_{10}(\text{sSFR}/\text{yr}^{-1}) < -10$ to account for the redshift evolution of the star-forming main sequence. We show quenched fractions for central galaxies (solid lines) and satellites (dashed lines) separately. At $z = 0$, low mass central galaxies are mostly star-forming, whereas massive galaxies are predominantly quenched. At the same time, a large fraction of low mass satellite galaxies (about 40-50%) are quenched at all masses. At all redshifts, satellite galaxies are more quenched than centrals of the same stellar mass, reflecting the strong impact of environmental effects.

In TNG, regardless of redshift, the transition from star-forming to quenched happens at $\log_{10}(M_\star/\text{M}_\odot) \sim 10 - 11$ for both central and satellite galaxies. Indeed, more than 90% of the TNG massive galaxies with $\log_{10}(M_\star/\text{M}_\odot) \gtrsim 11$ are quenched. TNG has almost no quenched centrals with $\log_{10}(M_\star/\text{M}_\odot) \lesssim 9.5$, while about 40-50% (10-15%) of its satellites are quenched in this mass range at $z = 0$ ($z = 2$). In L-GALAXIES, on the other hand, central quiescence is a strong function of redshift. At $z = 2$, roughly 20-30% of massive centrals, $\log_{10}(M_\star/\text{M}_\odot) \gtrsim 11$, are quenched, dropping to less than 5% for lower mass galaxies. More than 20% of satellites are quenched at all masses. At $z = 0$, quenched fractions for both centrals and satellites in L-GALAXIES are much more similar to TNG, except shifted to higher stellar masses.

The transition from predominantly star-forming to predominantly quenched galaxies for both TNG and L-GALAXIES is caused by supermassive black hole feedback, producing similar trends of quenched fraction versus stellar mass. In TNG, the transition point where the quenched fraction equals 50% occurs at a stellar mass roughly 0.5 dex lower than in L-GALAXIES. The most significant difference is at $z = 2$, where effective black hole feedback in TNG produces a population of quenched galaxies even at early times (see Donnari et al. 2019). In contrast, the quenching mechanism in L-GALAXIES does not operate as strongly at high redshifts, which results in a much lower abundance of massive quenched galaxies (see Martis et al. 2016, for an observational perspective).

Comparing our results with other studies, G16 find that the median sSFR of star-forming galaxies in the EAGLE simulation is in agreement with the GALFORM and L-GALAXIES (Guo et al. 2013 version) SAMs apart from small differences caused by feedback processes. They also find that the distribution of sSFR of galaxies with $10 < M_\star/\text{M}_\odot < 11$ is similar for EAGLE, GALFORM and L-GALAXIES. In contrast, in Fig. 2.5, we showed that L-GALAXIES and TNG are rather different in that particular stellar mass range. G16 also show that the fraction of quenched galaxies is rather similar between EAGLE, GALFORM and L-GALAXIES at $z = 2$, but is considerably different at $z = 0$, in particular for lower mass galaxies ($M_\star/\text{M}_\odot < 9.5$). Nevertheless, in the same stellar mass range, we show that there is a relatively good agreement between L-GALAXIES and TNG (see Fig. 2.6).

---

[4]We note that recent developments in Henriques et al. (2020) have lead to improvements to the sSFRs and HI-to-stellar mass ratios.
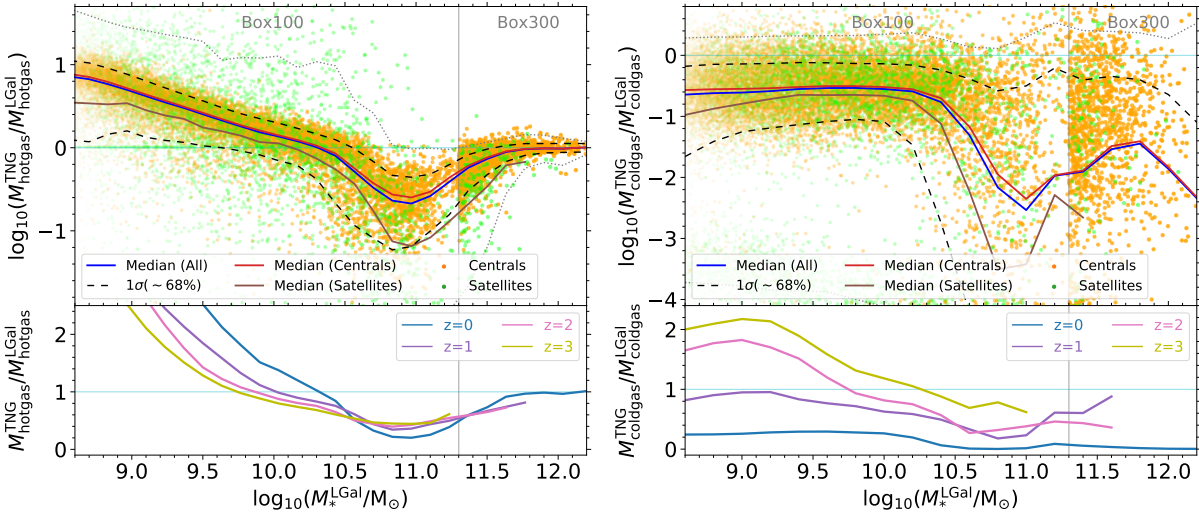
Figure 2.7: The ratios of hot gas mass (left panel) and cold gas mass (right panel) for individual objects between the two models. Each dot corresponds to a single galaxy; centrals and satellites are shown in orange and green, respectively. Solid lines show medians, while dotted and dashed lines show 1σ and 2σ scatter. The bottom sub-panels emphasise the redshift evolution of the median relations, from $0 < z < 3$. While low-mass TNG galaxies have overall more hot gas, the trend is reversed at high masses. On the other hand, TNG galaxies of all masses have less cold (star-forming) gas than in L-GALAXIES, by a factor of a few at low masses, with a maximal difference at $\log_{10}(M_\star/M_\odot) \sim 11$ of > 1 dex, due to a combination of feedback and environmental effects.

2.3.3 Gas content of galaxies and subhaloes

The way in which cosmic gas is treated is one of the principal differences between hydrodynamical simulations such as TNG and semi-analytical models, including L-GALAXIES. In L-GALAXIES, the gas bound to subhaloes is divided into non-star-forming and star-forming gas components, in addition to a third gas reservoir of ejected material that is not spatially localized, but for our current purposes we consider to be entirely outside the (sub)halo. In order to compare the gas contents of galaxies between L-GALAXIES and TNG models, we divide the gas cells in TNG subhaloes into two similar categories. For each subhalo, we consider the hot (not star-forming) gas to be the sum of all the bound gas cells with SFR = 0 and the cold (star-forming) gas to be the sum of the ones with SFR > 0. By definition, these two subsets are disjoint, and sum to the total gas mass.

The ratio of hot gas mass between matched galaxies is given in the left panel of Fig. 2.7. The median (blue solid line) relation shows that galaxies with $8.5 \lesssim \log_{10}(M_\star/M_\odot) \lesssim 10.5$ have more hot gas in TNG than in L-GALAXIES. This difference increases towards lower stellar masses, reaching nearly 1 dex by $\log_{10}(M_\star/M_\odot) \sim 8.5$. Across this stellar mass range a large fraction of the hot gas of L-GALAXIES subhaloes has been pushed into the ejected reservoir by supernova feedback. On the other hand, galaxies with $10.5 \lesssim \log_{10}(M_\star/M_\odot) \lesssim$

11.5 are more gas-rich in L-GALAXIES than in TNG, because much of the hot gas in TNG galaxies has been pushed out of the halo by AGN feedback. Finally for galaxies with $\log_{10}(M_\star/\mathrm{M}_\odot) \gtrsim 11.5$ the median ratio approaches unity. These trends are similar for centrals and satellites, although the satellite ratios are always lower than the central ratios by $\gtrsim 0.1$ dex. This shows that, in addition to differences in feedback/internal processes, there are also considerable differences in environmental effects which we will analyse in more detail in §2.4.

The left sub-panel of Fig. 2.7 depicts median individual hot gas ratios as a function of stellar mass at four different redshifts. A clear trend can be seen with time. The ratios are closer to unity at earlier cosmic times, particularly for low-mass galaxies.

Moving to the cold (star-forming) gas component, the ratios of cold gas mass between TNG and L-GALAXIES are shown in the right panel of Fig. 2.7. The median ratio of all galaxies (blue solid line) shows that galaxies have lower cold gas masses in TNG than in L-GALAXIES at $z = 0$, and this is true for all stellar masses. A rapid decrease in the median ratio occurs at $\log_{10}(M_\star/\mathrm{M}_\odot) \sim 10.5 - 11$ as many TNG galaxies become depleted or even devoid of cold star-forming gas. Note that in TNG, the smallest amount of cold gas detectable in a galaxy is roughly the mass of a single gas cell, $\log_{10}(m_{\mathrm{cell}}/\mathrm{M}_\odot) \sim 6 - 7$. In L-GALAXIES there is a cold gas mass threshold, M_{crit}, below which no star formation is allowed to occur (see Henriques et al. 2015, Eq. S15). As a side effect, quenched galaxies with no ongoing star formation can typically maintain a non-negligible amount of cold gas.

On average, the ratio for satellites (brown solid line) is below that for centrals (red solid line) by at least 0.1 dex. The right sub-panel of Fig. 2.7 shows median ratios for cold gas as a function of stellar mass at different redshifts. There is a strong trend with redshift: at higher redshifts ($z \sim 3$), low-mass TNG galaxies have more cold gas and $M_{\mathrm{coldgas}}^{\mathrm{TNG}}/M_{\mathrm{coldgas}}^{\mathrm{LGal}} > 1$, but this ratio decreases with time and drops below unity for $z < 1$. On the other hand, at the high mass end and $\log_{10}(M_\star/\mathrm{M}_\odot) \gtrsim 10.5$, cold gas masses are always smaller in TNG galaxies for $z < 3$, and this difference becomes slightly more pronounced towards redshift zero.

We note that it would be possible to use alternative approaches to separate the 'hot' and 'cold' gas components in a hydrodynamical simulation. For example, M18 enforce several conditions on temperature, density, rotational support, and spatial position, thereby comparing gas in the EAGLE simulation to the GALFORM semi-analytical model. Given our current methodology, we note that in TNG, gas cells with $T \lesssim 10^4$ k are star-forming. More than half of the TNG galaxies with $\log_{10}(M_\star/\mathrm{M}_\odot) > 9$ have more than 80% of their star-forming (cold) gas within twice the half-stellar-mass-radius and less than 20% of galaxies within that stellar mass range have more than half of their star-forming (cold) gas beyond twice the half-stellar-mass-radius. Similarly, for the non-star-forming (hot) gas, more than 80% of TNG subhaloes with $\log_{10}(M_\star/\mathrm{M}_\odot) > 9$ have less than 10% of their hot gas within twice the stellar half mass radius, and less than 1% of TNG subhaloes have more than half of their hot gas within that radius. In addition, in both L-GALAXIES and TNG, the hot and cold gas components are disjoint and sum to the total gas mass of the galaxy. We therefore have adopted the current approach as a robust and simple choice.
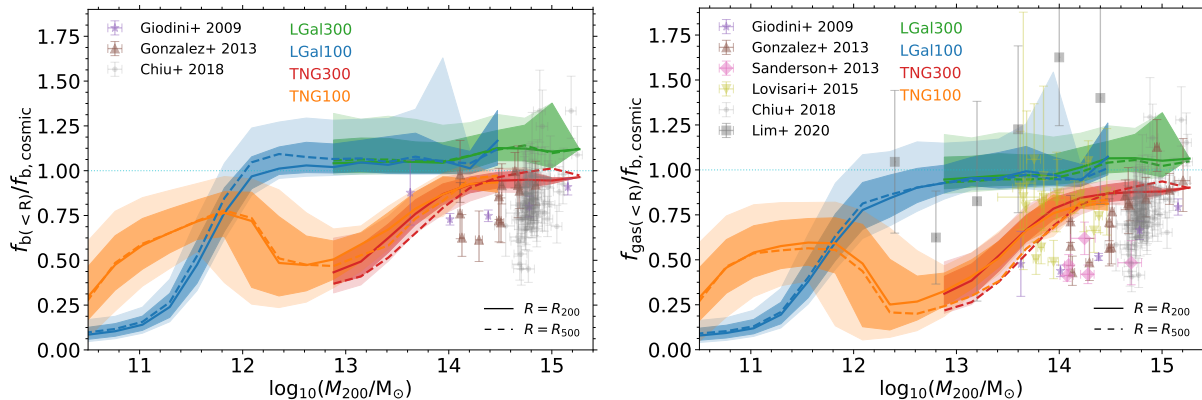
Figure 2.8: The baryon (left panel) and gas (right panel) fractions against halo M_{200}. The solid and dashed lines correspond to the median of the total baryon/gas to halo mass ratio within R_{200} and R_{500} respectively. The dark and light shaded regions illustrate 1σ and 2σ of the distribution for within R_{200} case. All the observations illustrate ratios within R_{500} except for Lim et al. (2020b) which corresponds to the gas ratio within R_{200}.

2.3.4 Halo baryon and gas fractions

Recent measurements of the cosmic microwave background show that the cosmic fraction of baryons is $f_{\rm b,cosmic} \sim 0.16$ (Planck Collaboration et al. 2018), and the baryon fraction in haloes is observed to be close to the cosmic value in massive galaxy clusters with $\log_{10}(M_{200}/{\rm M_\odot}) > 14$, (e.g. see Sanderson et al. 2013; Chiu et al. 2018). However, many studies have shown that the baryon fraction in lower mass haloes, $13 < \log_{10}(M_{200}/{\rm M_\odot}) < 14$, can be below this value (e.g. David et al. 2006; Lovisari et al. 2015), a manifestation of the 'missing baryons' problem.

Fig. 2.8 compares theoretical predictions for halo baryon fractions in L-Galaxies versus TNG at $z = 0$, and shows how these results stack up against available observations. The observational data are based on a number of different sample selection and gas detection techniques. Lim et al. (2020b) measures gas content within R_{200} using the kinematic Sunyaev-Zel'dovich effect (Sunyaev & Zeldovich 1972, hereafter SZE). All other datasets measure gas content within R_{500} based on X-ray emission: Giodini et al. (2009); Gonzalez et al. (2013); Lovisari et al. (2015) have X-ray selected samples, Sanderson et al. (2013) use an optically selected sample and Chiu et al. (2018) employ a sample of galaxy clusters selected based on SZE. In Fig. 2.8 we report baryon and gas fractions as a function of M_{200}, so we have converted any M_{500} values to M_{200} using the ratio of these two quantities from TNG. We note that this shifts the x-axis values, while baryon and gas fractions on the y-axis are unchanged.

For the models, we show baryon and gas fractions both within R_{200} (solid lines) and within R_{500} (dashed lines). The dark and light shaded regions correspond to the 1σ and 2σ scatter of the R_{200} measurements. We note that L-Galaxies only considers total gas within R_{200}, and we assume an isothermal $\rho \propto r^{-2}$ profile for hot gas to derive the mass

contained within R_{500} for consistency with the choice of profile assumed in the modelling of processes such as cooling and ram-pressure stripping. Other choices, such as a β profile, would change the gas and baryon fractions within R_{500} (e.g. see Fig. 6 of Yates et al. 2017, for groups and clusters).

For some haloes, L-GALAXIES baryon fractions are somewhat greater than $f_{\text{b,cosmic}}$. The reason is due to its implementation of environmental effects such as tidal and ram-pressure stripping, as well as its gas-infall recipe, as discussed in Yates et al. (2017). Due to tidal effects, galaxies in the infall regions lose dark matter in the DMO simulation on which L-GALAXIES run. However, as there is no gas stripping for those galaxies, they do not lose any gas, artificially increasing the baryon fraction of their host halo. This is resolved in Chapter 3 and Chapter 4 of this thesis with our new gas stripping implementation, which treats all galaxies based on measurements of their local environment. In addition, if the halo M_{200} decreases because of morphology or concentration changes, the gas mass remains unchanged, and this causes a spurious increase in baryon fraction. Yates et al. (2017) resolve this issue by correcting input halo merger trees to prevent M_{200} from decreasing with cosmic time. We will implement similar corrections in future work.

For clusters with $\log_{10}(M_{200}/\text{M}_\odot) \gtrsim 14$, both L-GALAXIES and TNG predict halo baryon fractions close to the cosmic value, in agreement with most observations. Both models have a relatively small scatter. Clusters are the only case where L-GALAXIES and TNG produce similar baryon fractions, while otherwise the outcomes are notably different. In lower mass haloes with $10 \lesssim \log_{10}(M_{200}/\text{M}_\odot) \lesssim 12$, L-GALAXIES baryon and gas fractions are lower than in TNG. This is mainly due to strong supernova feedback in L-GALAXIES, which pushes material, in particular hot gas, into an ejected reservoir for some time.

For haloes with $12 \lesssim \log_{10}(M_{200}/\text{M}_\odot) \lesssim 14$, the TNG baryon fraction is significantly lower than the cosmic value in contrast with L-GALAXIES, where these fractions are almost at the cosmic value for most haloes with $\log_{10}(M_{200}/\text{M}_\odot) \gtrsim 12$. This is primarily caused by different implementations of AGN feedback in the two models, as described in §1.2.6 and §1.3. Briefly, AGN feedback in TNG is able to push gas out of the halo, while in L-GALAXIES it only prevents cooling onto the central galaxy, without changing the total baryonic mass.

Comparing the group mass scale $13 \lesssim \log_{10}(M_{200}/\text{M}_\odot) \lesssim 14$ against observations, TNG baryon fractions agree better with Lovisari et al. (2015), while L-GALAXIES haloes are in a better agreement with Lim et al. (2020b). For lower mass haloes with $12 \lesssim \log_{10}(M_{200}/\text{M}_\odot) \lesssim 13$, L-GALAXIES predictions are in better agreement with Lim et al. (2020b) who find values close to the cosmic baryon fraction. We note that many subtleties exist in a proper comparison of these quantities. For example, the halo mass itself is computed in simulations using the three-dimensional spherical overdensity value given the total matter distribution, whereas in observations this quantity must be indirectly derived from an observable such as galaxy luminosity or stellar mass (e.g. see Yang et al. 2007). Detailed comparison of halo $f_{\text{gas}}(M_{200})$ trends would benefit from mock X-ray and/or SZE measurements from the simulations (see e.g. Lim et al. 2020a)

In a comparison between the GALFORM and EAGLE models, M18 show that at $z = 0$,
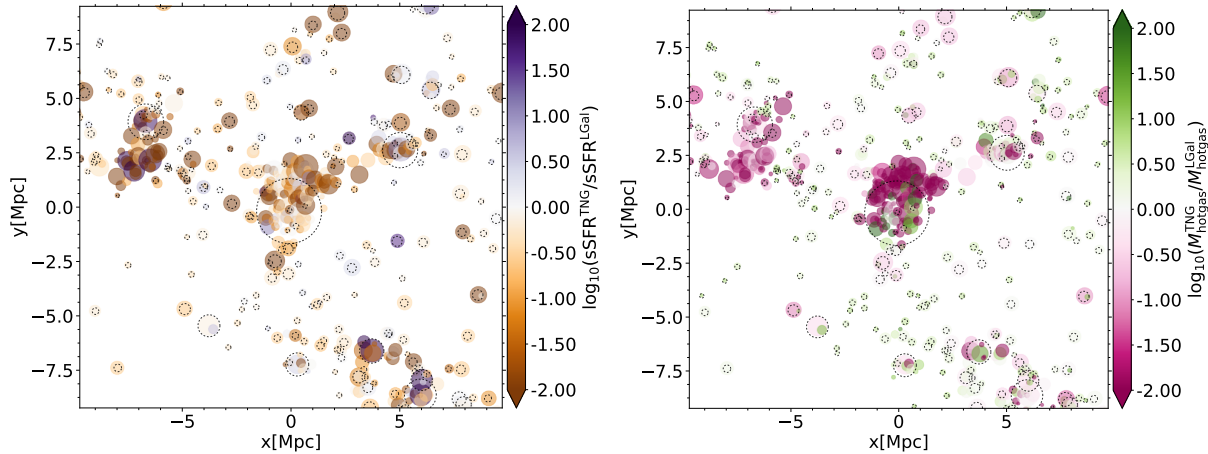
Figure 2.9: Galaxies within a region of size 8 Mpc centred on a massive cluster. Each circle shows a galaxy with its size reflecting the galaxy's stellar mass. Colours correspond to the ratio between predictions of TNG and L-Galaxies for sSFR (left panel) and hot gas mass (right panel). The dashed grey circles depict the boundaries, R_{200}, for various haloes. The galaxies shown are those matched in the two simulations and all have $\log_{10}(M_\star/\mathrm{M}_\odot) > 8.5$ in L-Galaxies.

Galform haloes have higher baryon fraction than Eagle and that the Galform halo baryon fractions increase with halo mass until they reach the cosmic value at $\log_{10}(M_{200}/\mathrm{M}_\odot) \sim$ 12, whereas Eagle haloes are on average at $\sim 40\%$ of the cosmic value at $\log_{10}(M_{200}/\mathrm{M}_\odot) \sim$ 12. We note that the halo baryon fraction vs. halo mass behaviour is very similar for the L-Galaxies and Galform semi-analytical models. On the other hand, the TNG and Eagle hydrodynamical simulations show quite different trends. Eagle baryon fractions increase monotonically with halo mass, while the baryon fractions of TNG haloes have a local minimum at $\log_{10}(M_{200}/\mathrm{M}_\odot) \sim 12$ where AGN feedback is efficient at removing gas from haloes (see Fig. 2.8).

2.4 Environmental dependency of galaxy evolution

As shown in §2.3, the differences between L-Galaxies and TNG are generally stronger for satellite galaxies than for centrals, due to the different treatment of key environmental processes, which we now study in more detail. We analyse properties of galaxies in and around haloes as a function of host halo mass, from low-mass groups to clusters. As our analysis is focused on more massive haloes, in this section we use the larger volume TNG300 simulation and the corresponding LGal300, unless stated otherwise.

Fig. 2.9 depicts galaxies surrounding a single cluster with $M_{200} \sim 10^{14}\mathrm{M}_\odot$, out to $\sim 6R_{200}$ in the 100 Mpc box. Several nearby haloes can also be seen in this region, and we mark their R_{200} with grey circles. Every galaxy is denoted by a circle, whose colour indicates the ratio of sSFR (left) or hot gas mass (right) between the TNG and L-Galaxies

models. Qualitatively, we see that both sSFR and hot gas mass can differ considerably, and that the differences are larger near massive groups and clusters. Broadly speaking, TNG galaxies in dense environments have less gas and lower star formation rates, showing that environmental effects play out differently in the two models.

2.4.1   Stellar masses

In §2.3.1 we demonstrated that the satellites in TNG tend to have higher stellar masses than in L-Galaxies. In the top row of Fig. 2.10 we show the ratio of TNG stellar mass to L-Galaxies stellar mass as a function of distance from halo centre. Solid lines show the median for all galaxies at that distance, regardless of whether they are centrals or satellites. We consider three central halo mass bins, with $\log_{10}(M_{200,\mathrm{host}}/\mathrm{M}_\odot)$ between 12 and 13, between 13 and 14, and above 14, as well as three galaxy stellar mass bins (using L-Galaxies masses), from $\log_{10}(M_\star/\mathrm{M}_\odot) = 9$ to $\log_{10}(M_\star/\mathrm{M}_\odot) = 12$. Dashed lines represent median ratios for each stellar mass bin for the simulation as a whole. Deviations from this global value can be interpreted as reflecting a difference in environmental effects between the two models.

A clear trend is present. Apart from massive galaxies (brown solid lines), the closer a galaxy is to halo centre, the larger its TNG stellar mass is compared to its L-Galaxies stellar mass. The effects are greatest for low-mass galaxies ($9 < \log_{10}(M_\star/\mathrm{M}_\odot) < 9.5$) close to the centre of low-mass groups with $12 < \log_{10}(M_{200}/\mathrm{M}_\odot) < 13$, where the enhancement of the ratio reaches 60%. Notice also that the effects extend out to several times the R_{200} of the central haloes.

2.4.2   Star formation

The bottom row of Fig. 2.10 shows the median $\mathrm{sSFR}^{\mathrm{TNG}}/\mathrm{sSFR}^{\mathrm{LGal}}$ ratio of galaxies as a function of halocentric distance. In the vicinity of clusters with $\log_{10}(M_{200}/\mathrm{M}_\odot) > 14$ (right panel), the local ratio of sSFR is lower than the global ratio out to a distance of at least $3R_{200}$. There is a local minimum at $R/R_{200} \sim 1.5-2$, which is close to the splashback radius indicating the most distant objects that have passed through the halo. We note that this radius likely also corresponds to the outermost extent of the hot gas halo, hence of the region within which environmental processes like ram pressure stripping of hot gas (RPS) can be significant. L-Galaxies assumes hot gas haloes to extend only to R_{200}, so environmental stripping effects are limited to satellites within this radius, whereas in TNG such effects can act to larger distances.

The ratio of sSFRs in the vicinity of groups with mass $13 < \log_{10}(M_{200}/\mathrm{M}_\odot) < 14$ (lower middle panel of Fig. 2.10) exhibits a different behaviour. Close to the centres of haloes, this ratio is more than 1 dex lower than its global value for low-mass (cyan line) and massive (brown line) galaxies, and by about 0.5 dex for intermediate mass galaxies (magenta line). The large differences between the two models in this halo mass bin arise from the fact that L-Galaxies only considers RPS for satellites within R_{200} of clusters, and no RPS is implemented for satellites within or around groups and lower mass haloes. In TNG, on the
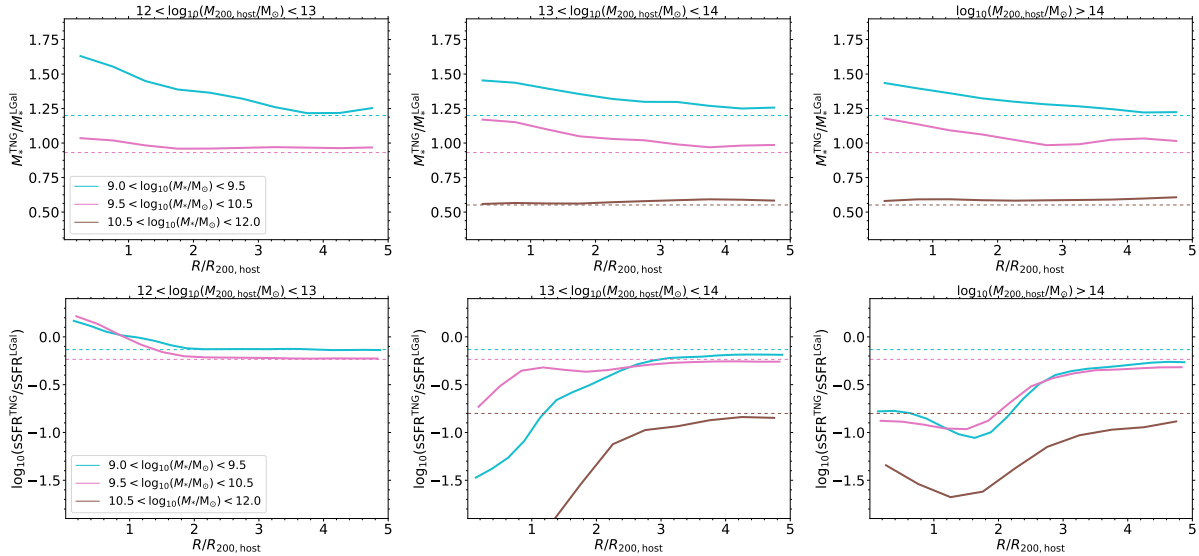
Figure 2.10: The ratio between the stellar mass (top row) and the sSFR (bottom row) of galaxies in TNG and L-Galaxies as a function of halocentric distance. Each panel refers to central haloes with masses in the range indicated. Each solid line shows the local median value of the ratio for galaxies with stellar mass (in L-Galaxies) in a specific mass range, as indicated by the legend. Dashed horizontal lines denote the corresponding global medians for the simulations as a whole. In the top row, the 300 Mpc box is used for the most massive stellar mass bin, while the 100 Mpc box is used for the other two bins. In the bottom row, all the results are taken from the 300 Mpc box.

other hand, RPS is included self-consistently according to the resolved gas dynamics in all objects. We note that $\text{sSFR}^{\text{TNG}}/\text{sSFR}^{\text{LGal}}$ is suppressed at all stellar masses to distances of $\sim 3R_{200}$, implying that RPS in TNG influences star formation both in and outside of the virialised region of galaxy groups.

The most massive galaxies with $\log_{10}(M_\star/\text{M}_\odot) > 10.5$ in the vicinity of clusters and groups are significantly less star-forming in TNG than in L-Galaxies (brown solid lines, lower right and middle panels). This is very likely the influence of AGN feedback prior to infall, rather than of environmental stripping effects. Intermediate mass galaxies within the groups (solid magenta line, lower middle panel), are much less affected by environment than massive galaxies, whereas the opposite would be expected if RPS was the dominant processes in these systems. Although the gas expelled by SMBH feedback in TNG could return to the halo at later epochs, this re-accretion would be inhibited for satellite sub-haloes, as the gas ejected from these objects is less bound and thus can be stripped by host halo. As a result, feedback in massive satellites enhances the influence of RPS, and this environmental suppression of star formation is stronger in TNG than in L-Galaxies.

The sSFR of galaxies in lower mass haloes with $12 < \log_{10}(M_{200}/\text{M}_\odot) < 13$ (lower left panel) has much smaller differences between the two models. The $\text{sSFR}^{\text{TNG}}/\text{sSFR}^{\text{LGal}}$ ratio is up to 0.5 dex above its global value for low-mass galaxies within R_{200}. We note that L-

GALAXIES does not include RPS processes within these low-mass haloes. In addition, tidal stripping processes may be different in the two models. Tidal stripping in L-GALAXIES depends on the gas and dark matter profiles of the satellite, both of which are assumed to be isothermal profiles with $\rho \propto r^{-2}$. This is an approximation that may not reflect the profiles of TNG satellites.

2.4.3   Environmental quenching

As discussed in §2.3.2, TNG galaxies are generally more quenched than in L-GALAXIES. Fig. 2.11 demonstrates that this also holds for galaxies in different environments, where we show the quenched fraction of galaxies versus halocentric distance (top row), and the quenched fraction of satellites in the two dimensional plane of stellar mass versus host halo mass (bottom row). In all clusters and groups, independent of distance from the centre, the majority of massive TNG galaxies are quenched (dashed red lines, top right and top middle panels). As discussed previously, AGN feedback rather than environment is the dominant effect. In contrast, the quenched fraction of similarly massive galaxies in L-GALAXIES near clusters show a clear trend with distance: galaxies closer to the centres of haloes are more quenched (dashed green line, top right panel). In general, the quenched fraction in L-GALAXIES clusters decreases with halocentric distance up to $R/R_{200} \sim 2$ until reaches a constant value (also see Henriques et al. 2017 for a comparison of L-GALAXIES with observations). [5]

The fraction of quenched intermediate and low-mass galaxies (solid lines) decreases with clustercentric distance up to $R \sim 1-3R_{200}$ in both models. Quenched fractions in TNG are usually higher than in L-GALAXIES. However, the difference between the models becomes smaller near the centres of clusters, implying that the environmental effects dominate over other general differences between the models. We see that the fraction of quenched galaxies around groups (top middle) is lower in both models compared to clusters (top right) and there is a clear trend with host halo mass.

The bottom panels of Fig. 2.11 show a two-dimensional view of quenched satellite fraction of haloes as a function of satellite stellar mass and host halo mass. The left panel illustrates this plane for L-GALAXIES, and the right panel for TNG. We observe a very strong horizontal feature in f_{quench} at $\log_{10}(M_\star/\text{M}_\odot) \sim 10.5$ in TNG (~ 11 in L-GALAXIES), which shows onset of the dominant, mass-dependent quenching mechanism of black hole feedback. The vast majority of galaxies above these stellar masses are quenched, regardless of environment (host halo mass). A second vertical feature in f_{quenched} occurs at host masses of $\sim 10^{14}\text{M}_\odot$ for L-GALAXIES. This feature is shifted to lower halo mass and also becomes diagonal in the case of TNG. This reflects the onset of environmental quenching processes. These two regimes are similar in spirit to those identified observationally by Peng et al. (2010). Interestingly, for given stellar mass the transition between mainly star-forming and mainly quenched occurs more sharply in TNG than in L-GALAXIES and at a halo mass

---

[5]We note that massive galaxies near lower mass haloes are excluded due to low number statistics (top left panel).
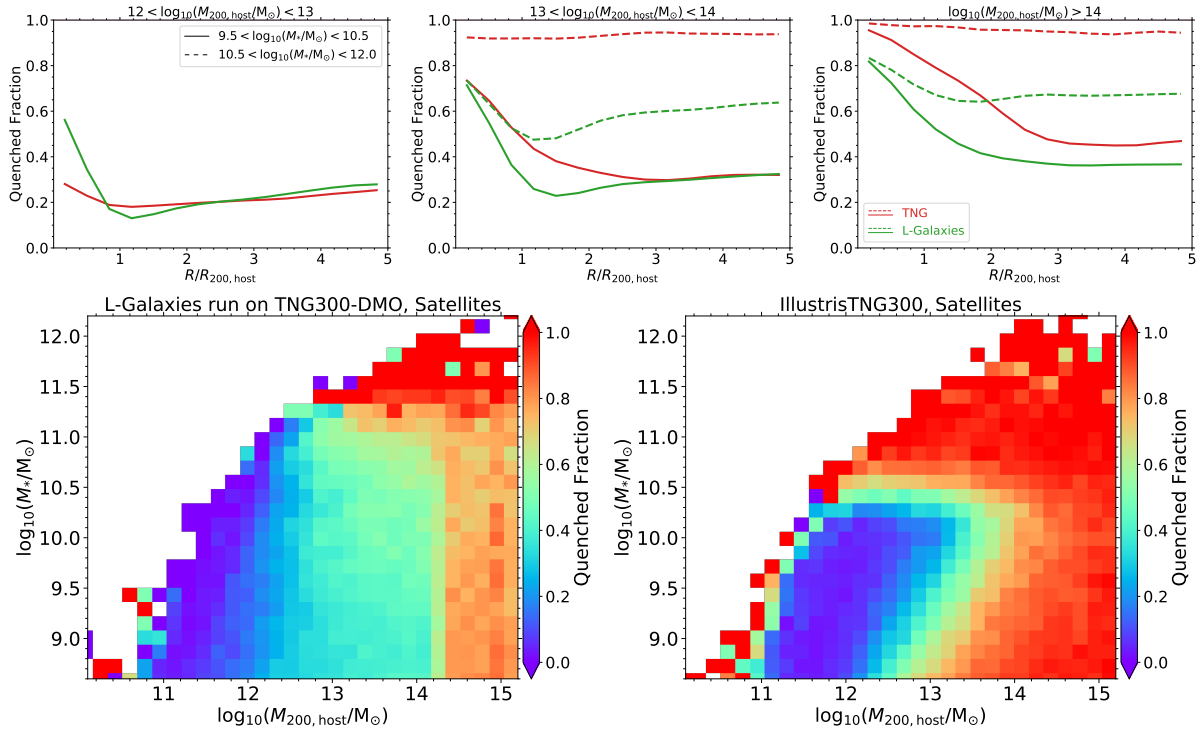
Figure 2.11: The top row shows the fraction of quenched galaxies in the vicinity of haloes in L-Galaxies and TNG as a function of halocentric distance. Each panel gives the quenched fraction around haloes in a particular mass range, from lower mass haloes (top left panel) to clusters (top right panel). The results in each panel are divided into two lines based on galaxy stellar masses (solid and dashed). The L-Galaxies results are from L-Galaxies run on the Millennium simulation with haloes more massive than the most massive TNG300 halo excluded for consistency. All neighbouring galaxies, both centrals and satellites, are included. The bottom panels illustrate the 2D plane of satellite galaxy stellar mass versus host halo mass, where the colour shows the fraction of quenched satellite galaxies. The left and right panels show the results for the L-Galaxies run on TNG300-DMO and the TNG300 simulation respectively. Galaxies with $\log_{10}(\mathrm{SSFR}[\mathrm{yr}^{-1}]) < -11$ are defined as quenched.

Figure 2.12: The ratio between hot gas masses in L-GALAXIES and in TNG for galaxies in the vicinity of haloes as a function of halocentric distance. Each panel is made for central haloes in the mass range indicated. Solid coloured lines show the median ratios for various stellar mass ranges. The dashed lines denote median ratios for the simulation as a whole.

which increases almost in proportion to the stellar mass.

In L-GALAXIES, satellite galaxies in massive haloes of $\log_{10}(M_{200}/\mathrm{M}_\odot) \gtrsim 14$, are significantly more quenched than those in lower mass groups, because RPS is assumed not to act below this mass threshold. At lower stellar masses, the fraction of quenched satellite galaxies still increases with the host mass, however, as a result of tidal stripping processes. In TNG, low-mass satellite galaxies in group environments experience environmental stripping and are generally more quenched than in L-GALAXIES.

2.4.4   Hot and cold gas content

In this section we carry out a similar analysis of environmental influences on the hot gas content of galaxies in L-Galaxies and TNG. The results shown in Fig. 2.12 are qualitatively very similar to those obtained above for sSFR. In and around clusters (right panel), the ratios (solid lines) are lower than their global values (dashed lines). There is a local minimum at $R \sim 1.5 - 2 R_{200}$, for all stellar mass ranges, similar to that seen for the ratio of sSFRs (Fig. 2.10) and this is likely caused by the same phenomenon.

In and around groups (middle panel), there is a clear trend with distance: the ratio increases from near zero to its global value with increasing distance away from the centres of haloes, reaching the average value by $R/R_{200} \sim 1 - 3$. The principal cause of this difference is again the lack of RPS in L-GALAXIES groups, and the lack of any kind of stripping beyond R_{200} in L-GALAXIES. In addition, as we showed in §2.3.4, the gas fraction of TNG groups is below the cosmic value, as the gas is ejected beyond the halo by AGN feedback. As a result, galaxies in the infall regions must pass through relatively dense gas. RPS then causes them to lose a fraction of their hot gas even while they are still outside the nominal halo boundary, R_{200}. Finally, within lower mass haloes (upper left panel) $M_{\mathrm{hotgas}}^{\mathrm{TNG}}/M_{\mathrm{hotgas}}^{\mathrm{LGal}}$ increases by up to 0.5 dex above its global value similar to the trend seen for sSFR. TNG satellites are able to retain hot gas more effectively than assumed by L-GALAXIES.

In Fig. 2.13 we show the hot gas to stellar mass ratio of galaxies as a function of distance

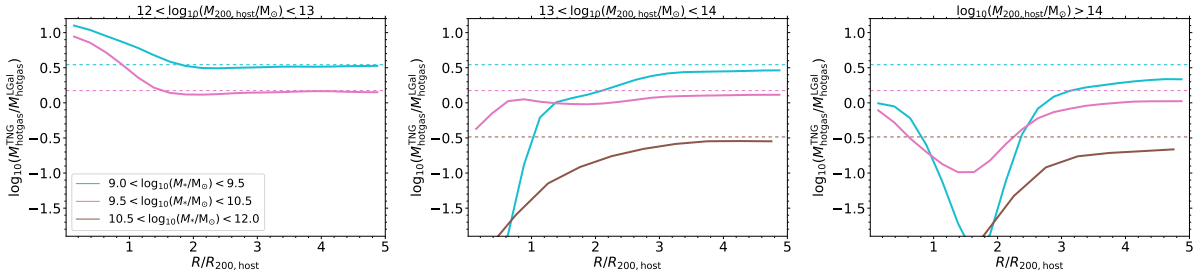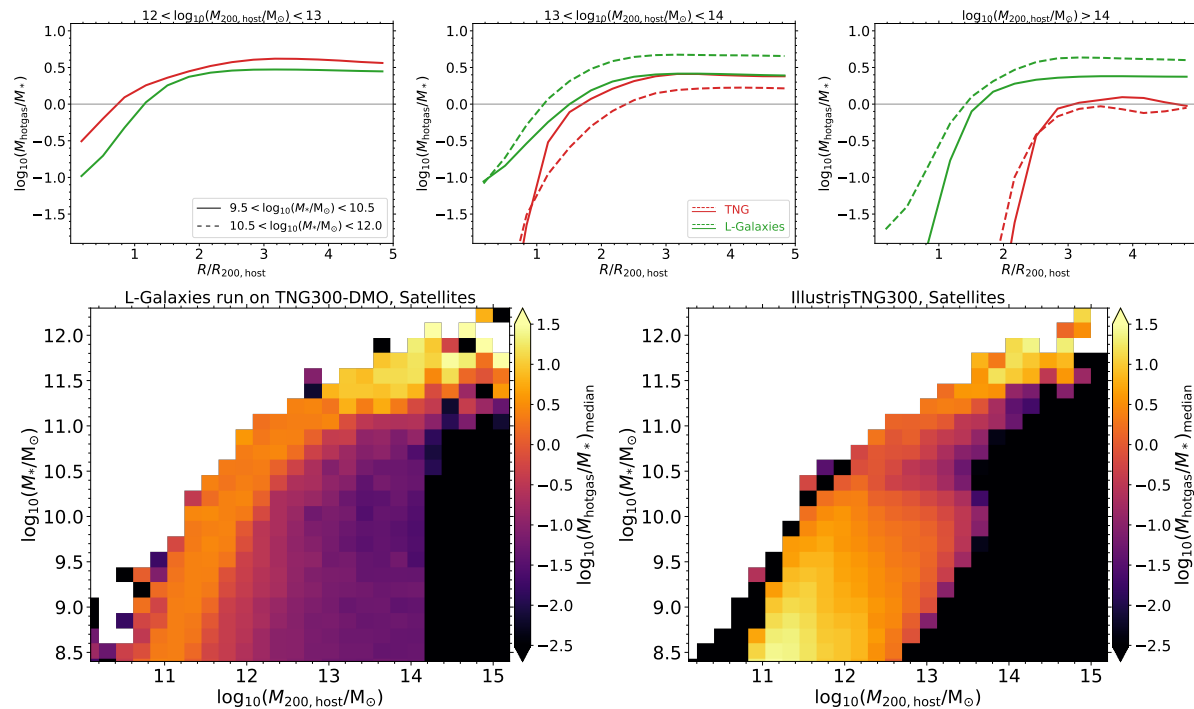Figure 2.13: The top row shows the hot gas to stellar mass ratio of galaxies in the vicinity of haloes in L-Galaxies (green) and TNG (red) as a function of halocentric distance. Each panel is made for central haloes within the given mass range, from lower mass systems (top left panel) to clusters (top right panel). The results are split based on galaxy stellar mass as indicated by the linestyle. The L-Galaxies results are from L-Galaxies run on the Millennium simulation with haloes more massive than the most massive TNG300 halo excluded for consistency. All neighbouring galaxies, both centrals and satellites, are included. The bottom panel shows the 2D plane of satellite galaxy stellar mass versus host halo mass, where the colour encodes the median hot gas to stellar mass ratio for satellite galaxies (left: L-Galaxies run on TNG300-DMO, and right: TNG300).

to halo centre (top row). Comparing the different host halo masses, the hot gas-to-stellar ratio decreases more strongly near more massive hosts. In both models, satellites within clusters (top right panel) have little remaining hot gas. At $R/R_{200} \sim 1 - 1.5$ a strong increase is visible in L-Galaxies, while a similar rise occurs in TNG at $R/R_{200} \sim 2 - 2.5$. Indeed, the local minimum that can be seen at $R/R_{200} \sim 1 - 2$ in the upper right panel of Fig. 2.12 is caused by the significant difference between the hot gas radii of TNG and L-Galaxies clusters. These correspond to the distance within which RPS environmental effects become significant. In L-Galaxies, this 'hot halo radius' is assumed to equal R_{200}, while in TNG it is determined by gas dynamics and is influenced by a variety of physical processes including feedback. Such a scale exists for groups (top middle panel) and lower mass haloes (top left panel) as well, but the transition between hot gas-poor and hot gas-rich galaxies is more gradual with distance.

The hot gas mass of massive galaxies (dashed lines) is more influenced by environment in TNG than in L-Galaxies. As the binding energy distribution of subhalo gas has been modified by baryonic feedback processes there is a larger fraction of gas weakly bound to the subhalo, where it can be more easily stripped. In contrast, gas is generally more strongly bound to subhaloes in L-Galaxies and thus harder to remove. As a result, RPS removes a considerable fraction of the hot gas from massive TNG galaxies in the vicinity of clusters and groups, leaving them significantly less gas-rich than the same objects in L-Galaxies.

The bottom panel of Fig. 2.13 shows the same 2D view of the stellar mass versus host halo mass plane as previously, but now coloured by the hot gas to stellar mass ratio of galaxies. For L-Galaxies there is a sharp transition in the ratio at a mass of $\log_{10}(M_{200}/M_\odot) \gtrsim 14.08$. This is due to RPS acting only in haloes above this mass. In TNG (right) a large fraction of galaxies in groups are gas-poor, as they are affected by stripping both within the haloes and in the infall regions beyond the halo boundary. There is, however, a sharp boundary between stripped and non-stripped satellites which occurs at the same stellar mass-dependent value of halo mass as the quenching boundary in Fig. 2.11.

Finally, Fig. 2.14 shows, in the same format as Fig. 2.12, the variation with halocentric distance of the ratio of the cold gas mass in TNG to that in L-Galaxies for galaxies in the vicinity of haloes. In and around TNG clusters, most galaxies have low to no star-forming gas, while galaxies in groups and lower mass haloes are able to keep a fraction of their cold gas. On the other hand, galaxies in the vicinity of L-Galaxies haloes remain much more cold-gas-rich [6]. In the vicinity of clusters (right panel), the ratio is below its global value even for galaxies which reside further than $5R_{200}$ from halo centre. The ratio is also suppressed for galaxies near groups (middle panel), but extending out only to $\sim 1 - 3R_{200}$. For satellites around low-mass hosts (left panel), the ratio is above its global value due to strong tidal stripping in L-Galaxies. We note that ram-pressure effects on the cold gas are not taken into account in L-Galaxies at any mass scale. In addition, L-Galaxies

---

[6]We note that the ratios of the most massive galaxies are below the lower limit of Fig. 2.14 and thus are not visible
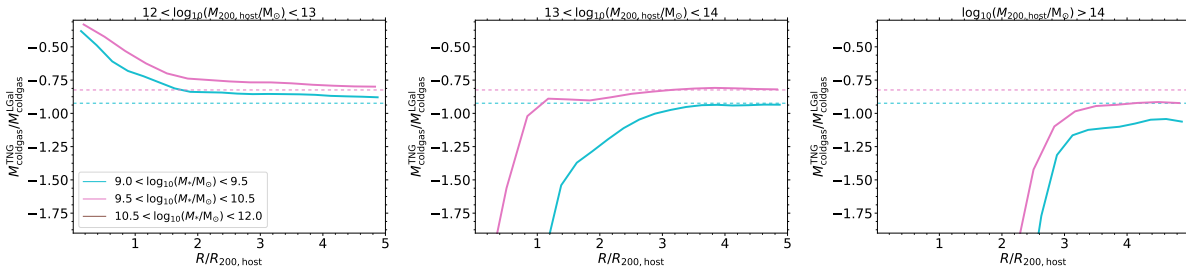
Figure 2.14: The ratio between cold gas masses in TNG and in L-Galaxies for galaxies (both satellites and centrals) in the vicinity of haloes as a function of halocentric distance. Each panel is made for haloes in a different mass range as indicated. Solid coloured lines show the median ratios for different stellar mass ranges. Dashed lines denote the median ratio for each stellar mass range for the simulation as a whole.

has a cold gas threshold, M_{crit}, below which no star formation occurs, leading to a lower limit on the predicted cold gas fractions. However, both L-Galaxies and TNG have been shown to provide an adequate match to the observed HI mass function at $z = 0$ (see Henriques et al. 2015; Diemer et al. 2019).

So far, our analysis has focused on median gas content. Fig. 2.15 shows for both models the full distributions of the ratios of hot (top) and cold (bottom) gas mass to stellar mass for intermediate-mass galaxies in the vicinity of massive clusters. We see that L-Galaxies (solid green lines) predicts more galaxies with a large hot gas mass fraction beyond the halo boundary than does TNG (solid red lines). Within R_{200} (dashed lines) there are fewer gas-rich galaxies in both models, and more galaxies have little to no hot gas. The trends with distance imply that galaxies are more likely to be stripped during infall (i.e. at $1 < R/R_{200} < 2$) in TNG than in L-Galaxies.

The cold gas content of galaxies (the bottom panel of Fig. 2.15) differs more substantially between the two models, and also behaves differently as a function of clustercentric distance. A large fraction of TNG satellites have very little or no cold gas, producing a secondary population which piles up towards the left of this figure. The lack of cold gas stripping in L-Galaxies, together with the assumed cold gas mass threshold for star formation, implies that cold gas is not strongly depleted even in quenched satellites near cluster centre. The result is a uni-modal distribution with a well defined peak at $M_{\mathrm{coldgas}}/M_{\star} \sim 0.2$ which shifts only slightly to lower values near cluster centre. Thus in L-Galaxies this distribution changes little with distance (shown by the different line styles), while for TNG the amplitude of the cold-gas-rich peak drops substantially towards cluster centre.

2.5 Summary and Discussion

In this chapter we have compared, object-by-object and statistically, the L-Galaxies semi-analytical model with the IllustrisTNG magnetohydrodynamical simulation. To do
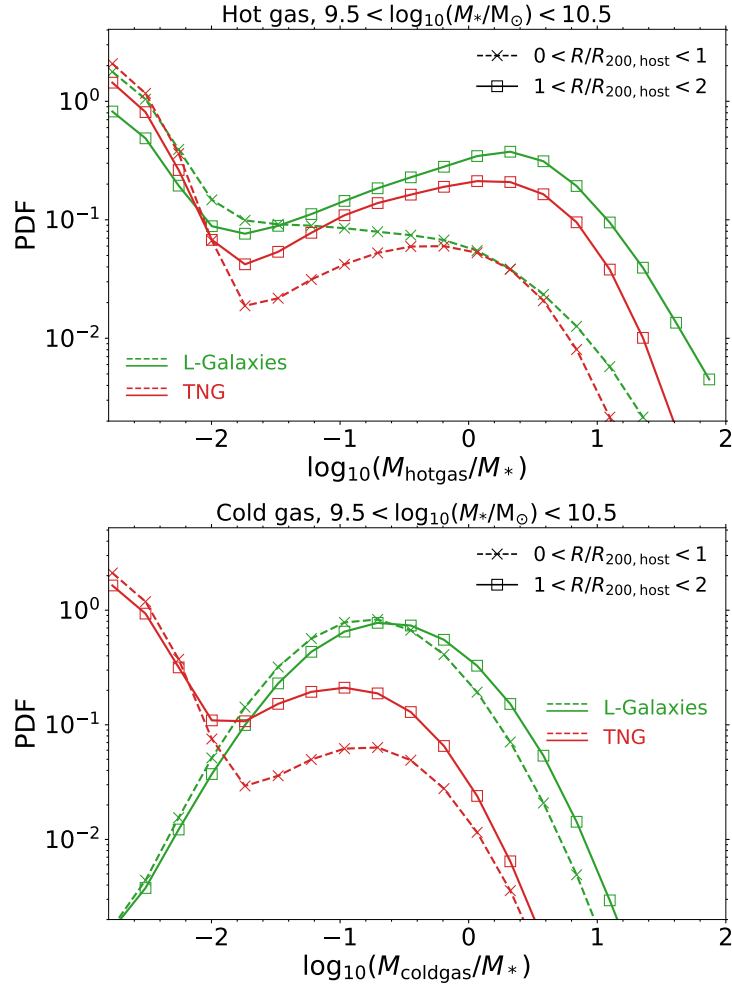
Figure 2.15: The ratio of hot (top) and cold (bottom) gas mass to stellar mass, for interme-
diate mass galaxies in the vicinity of massive clusters with $M_{200}/\mathrm{M_\odot} > 10^{14}$. Results are
shown for L-Galaxies in green and for TNG in red. Different line styles refer to different
distance ranges from cluster centre. Solid lines are for galaxies beyond R_{200}. These may not
have passed through the cluster and may be central galaxies or satellites of other nearby
haloes. All galaxies with zero gas or with logged ratios smaller than -2.8 are assigned to
the leftmost bin.

so, we have run L-Galaxies on subhalo merger trees from the TNG-DMO simulation. Comparing the properties of galaxies and haloes between the two models, we find that:

- The stellar mass functions (SMF) of the two models agree with each other and with observations (at a level better than 0.2 dex) since $z = 3$. The stellar masses of matched galaxies are also in good agreement with a typical scatter of ~ 0.2 dex, independent of redshift. The stellar mass to halo mass (SMHM) relation shows the stellar mass fraction of haloes to be generally larger in TNG than in L-Galaxies (up to 60%, Fig. 2.2).

- By $z = 0$ TNG galaxies become predominantly quenched for $\log_{10}(M_\star/\mathrm{M_\odot}) \geq 10.5$ whereas in L-Galaxies this characteristic mass scale is larger, $\log_{10}(M_\star/\mathrm{M_\odot}) \geq 11$. As a result, the specific star formation rate (sSFR) of galaxies is lower in TNG than in L-Galaxies over the transition regime, $10 \lesssim \log_{10}(M_\star/\mathrm{M_\odot}) \lesssim 11$ (Fig. 2.4). In addition, TNG predicts a higher fraction of quenched galaxies at higher redshifts, in particular at $z \geq 2$ (Fig. 2.6).

- The models agree on the amount of hot (non-star-forming) gas around massive galaxies ($\log_{10}(M_\star/\mathrm{M_\odot}) \gtrsim 11.5$). Intermediate-mass galaxies ($10.5 \lesssim \log_{10}(M_\star/\mathrm{M_\odot}) \lesssim 11.5$) are more hot-gas-rich in L-Galaxies. Low-mass galaxies ($\log_{10}(M_\star/\mathrm{M_\odot}) \lesssim 10.5$) are more hot-gas-rich in TNG (Fig. 2.7).

- A large fraction of quiescent galaxies in TNG have little or no cold (star-forming) gas, whereas those in L-Galaxies are generally more cold-gas-rich at $z = 0$. For galaxies with $\log_{10}(M_\star/\mathrm{M_\odot}) \lesssim 10.5$, $M_{\mathrm{coldgas}}^{\mathrm{TNG}}/M_{\mathrm{coldgas}}^{\mathrm{LGal}}$ decreases with cosmic time (Fig. 2.7).

- In clusters with $\log_{10}(M_{200}/\mathrm{M_\odot}) \gtrsim 14$, both models predict halo baryon fractions near the cosmic value. For groups with $12 \lesssim \log_{10}(M_{200}/\mathrm{M_\odot}) \lesssim 14$, TNG haloes have a lower baryon fraction than L-Galaxies haloes. At $\log_{10}(M_{200}/\mathrm{M_\odot}) \sim 12$, TNG haloes reach half the cosmic baryon fraction due to ejective feedback, whereas L-Galaxies haloes remain at the cosmic value (Fig. 2.8).

The differences above are mainly a result of the differing treatments of stellar and black hole feedback between the two models. In TNG the mass ejected by both kinds of feedback is spatially resolved. In L-Galaxies only supernovae eject gas, and the exact location of the ejecta is not specified. This material is kept unavailable for cooling until it returns to the subhalo and is reincorporated in the hot gas component. Unlike in TNG, it does not contribute to processes like ram-pressure stripping at large radii from halo centre.

The characteristic stellar mass scale where the population transitions from star-forming to quenched reflects black hole feedback prescriptions and is 0.5 dex higher in L-Galaxies than in TNG. Such feedback can push gas well beyond the halo boundary in TNG but not in L-Galaxies. This redistribution of baryonic mass within and outside massive dark matter haloes is a key prediction of the TNG model.

Galaxies differ more strongly between the two models in and around dark matter haloes, due to differing treatments of environmental effects. For galaxies in the vicinity of haloes, we find that:

- The stellar mass ratio, $M_\star^{\mathrm{TNG}}/M_\star^{\mathrm{LGal}}$, increases near the centres of massive haloes, whereas the ratio $\mathrm{sSFR}^{\mathrm{TNG}}/\mathrm{sSFR}^{\mathrm{LGal}}$ decreases (Fig. 2.10). Galaxies in the vicinity of clusters and groups are more frequently quenched than field galaxies in both models, but more so in TNG. The influence of clusters on quenching extends to larger radii in TNG than in L-Galaxies (Fig. 2.11).

- The ratio between the hot gas masses predicted for galaxies by the two models, $M_{\mathrm{hotgas}}^{\mathrm{TNG}}/M_{\mathrm{hotgas}}^{\mathrm{LGal}}$, falls below its average value in the vicinity of clusters and groups (Fig. 2.12), as do the mass ratios for cold (star-forming) gas (Fig. 2.14). Overall, environment imprints a stronger signature on galaxies in the vicinity of haloes in TNG. Gas stripping beyond R_{200} is substantial in TNG but weak in L-Galaxies.

- Massive galaxies ($\log_{10}(M_\star/\mathrm{M}_\odot) \gtrsim 10.5$) in the vicinity of clusters and groups are less gas-rich and less star-forming in TNG than in L-Galaxies (Figs. 2.10, 2.12, 2.13). This reflects pre-existing differences in the field, together with an enhancement of ram-pressure stripping due to AGN feedback, which makes extended subhalo gas less bound and thus more easily stripped.

These environmental differences arise primarily because not all relevant stripping processes are implemented in L-Galaxies (e.g. ram-pressure stripping of cold gas is not included) or are intentionally restricted (e.g. ram-pressure stripping of hot gas is assumed to be negligible in galaxy groups). Our comparisons with TNG suggest that these assumptions need to be re-evaluated, and may need to be modified if the stripping levels seen in TNG are realistic. In Chapters 3, 4 we update L-Galaxies to include a new method to extend ram-pressure stripping of hot gas to all galaxies, even those outside clusters, based on local measurements of the particle density and velocity fields. In the future, we will study the degree to which such prescriptions can align the environmental effects found in semi-analytic versus hydrodynamical simulations, as explored in this work.

Careful comparison with observations of the sSFR and gas fractions of galaxies in and around clusters will highlight the strengths and limitations of each simulation technique and allow both to achieve a new degree of physical realism. In addition, we expect that our comparisons between SAMs and hydrodynamical simulations techniques will become more important in the future development of galaxy evolution models to be run in Gigaparsec simulation volumes.

Chapter 3

Local Background Environment

3.1 Introduction

In this chapter we measure local properties in the immediate vicinity of dark matter sub-haloes, namely background density and bulk velocity. These quantities will be transferred from dark matter to gas based on our model assumption that gas traces dark matter linearly (possible deviations are discussed in §3.3.3). We use this local background environment (LBE) to devise a more realistic treatment of ram pressure stripping in the L-Galaxies SAM. We also investigate a variety of background properties using our LBE technique and dark matter particle data from the Millennium Simulation (Springel et al. 2005).

This chapter is structured as follows: In §3.2, we describe the gas stripping theory. In §3.3 we introduce the definition of the local background environment and discuss how it can be used for the calculation of ram-pressure force. Analysis of the LBE is given in §3.4, where we consider its velocity, density, and the correlation with galaxy and subhalo properties. In §3.5, we show the results of our new method applied to L-Galaxies and the resulting changes to the baryonic properties of galaxies. We conclude and summarize in §3.6.

3.2 Hot gas stripping

The amount of the hot gas from cosmic infall that is added to every central dark matter subhalo, and therefore its galaxy, is set to keep the baryon fraction within R_{200} of the FOF halo hosting that central subhalo equal to the cosmic baryon fraction. In addition, the radius of the hot gas halo, R_{hotgas}, is set equal to the R_{200} of its FOF halo for every central subhalo. For satellite galaxies, however, there is no cosmic accretion post-infall. As a result their hot gas radius is modified to be the smaller of R_{hotgas} and the stripping radius, $R_{\mathrm{stripping}}$, as described in detail in §3.2.1 and §3.2.2.

Here, we explain the physical processes which strip gas, and the prescriptions we use to estimate and implement them in the L-Galaxies SAM.

3.2.1 Ram-pressure stripping

Ram-pressure stripping can act on both the hot and the cold gas components of a galaxy. Physical prescriptions for the RPS of hot gas are currently included in the fiducial L-Galaxies model. Techniques to include ram-pressure stripping of cold gas in disks have also been explored (Luo et al. 2016), but these are not yet included in the publicly-released version of the model and we do not adopt them here. In this chapter, we focus on a more accurate model for the stripping of the hot gas. We adopt and extend the approach originally suggested by McCarthy et al. (2008) and already used in L-Galaxies in simpler form by Guo et al. (2011) and Henriques et al. (2015) to derive the ram-pressure stripping radius, the radius outside which all hot gas is assumed to be stripped. Our implementation contains a new method to resolve environmental properties as well as an updated estimation of the self-gravity of galaxies. We apply RPS to galaxies with an identified subhalo, i.e. central galaxies and type 1 satellites.

In general, gas can be stripped out of a subhalo if the ram-pressure force from its environment overcomes the gravitational force on its gas component. The scale on which that happens is defined by the ram-pressure stripping radius, R_{rp}. Beyond the stripping radius, all the hot gas is assumed to be stripped. The ram-pressure can be calculated using the formula of Gunn & Gott (1972) as

$$P_{\text{rp}} = \rho_{\text{LBE,gas}} \, v_{\text{gal,LBE}}^2 \,, \tag{3.1}$$

where $\rho_{\text{LBE,gas}}$ is the gas density of the galaxy's local background environment (see §3.3.1) and $v_{\text{gal,LBE}}$ is the velocity of the galaxy relative to the environment it is moving through. The gravitational force per unit area between the galaxy's hot gas and its subhalo at a given radius from the center of the subhalo is

$$F_{\text{g}}(r) = g_{\text{max}}(r) \, \rho_{\text{hotgas}}^{\text{proj}}(r) \,, \tag{3.2}$$

where $\rho_{\text{hotgas}}^{\text{proj}}(r)$ is 2D projected hot gas density around the galaxy and $g_{\text{max}}(r)$ is the maximum restoring gravitational field in the direction of galaxy's velocity relative to its LBE.

Calculation of the subhalo mass within a given radius requires assumptions for the density profiles of the dark matter and gas components. We assume subhalo and hot gas density profiles to be isothermal spheres with $\rho \propto r^{-2}$. Therefore, the maximum gravitational field is

$$g_{\text{max}}(r) = \frac{G M_{\text{subhalo}}(r)}{2r^2}, \tag{3.3}$$

where $M_{\text{subhalo}}(r)$ is the subhalo mass within the radius r and is defined as

$$M_{\text{subhalo}}(r) = M_{\text{g}} \frac{r}{R_{\text{g}}}, \tag{3.4}$$

where R_{g} is the radius within which we estimate the gravitational potential of the subhalo, and M_{g} is the mass within that radius, respectively. For central galaxies, we take $R_{\text{g}} = R_{200}$

and $M_\mathrm{g} = M_{200}$. For satellite galaxies, R_{200} and M_{200} are not appropriate values. Previous L-Galaxies models (e.g. Guo11 and H15) used the mass and radius at the time when the satellite galaxy was last a central, i.e. $M_{200,\mathrm{infall}}$ and $R_{200,\mathrm{infall}}$. Here we take R_g to be the half-mass radius of the subhalo, R_halfmass, and M_g to be the total mass within half-mass radius at its current snapshot. The mass contained within this radius should constitute a more faithful representation of the actual gravitational potential of the subhalo at late times, once significant tidal stripping has occurred.

Adopting an isothermal profile with $\rho \propto r^{-2}$ for the galaxy's hot gas halo, the 2D projected hot gas density can be estimated as

$$\rho_\mathrm{hotgas}^\mathrm{proj}(r) = \frac{M_\mathrm{hotgas}}{2\pi R_\mathrm{hotgas} r}, \tag{3.5}$$

where M_hotgas and R_hotgas are the hot gas mass and radius of the subhalo which undergoes RPS, and the coefficient $1/2\pi$ is chosen so that the integral of the projected density equals M_hotgas within projected radius R_hotgas.

Finally, the ram-pressure stripping radius, R_rp, is given by

$$R_\mathrm{rp} = \left(\frac{G M_\mathrm{g} M_\mathrm{hotgas}}{4\pi R_\mathrm{g} R_\mathrm{hotgas} \rho_\mathrm{LBE,hotgas} v_\mathrm{gal,LBE}^2} \right)^{1/2}. \tag{3.6}$$

Given the two main properties of a galaxy's LBE (i.e. the density and the velocity of the environment through which the galaxy is moving), the above estimate for the stripping radius can be applied to all of the galaxies in the simulation.

For reference, we note that Guo11 and H15 considered RPS only on satellite galaxies within R_{200}. For each satellite galaxy, they adopted a local gas density assuming an isothermal gas density profile ($\rho \propto r^{-2}$), and took the velocity of galaxy relative to its LBE, $v_\mathrm{gal,LBE}$, as the virial velocity of the host FOF halo. These are reasonable average estimates, but they are not local measurements, and do not extend to satellites beyond the virial radius or to central galaxies.

3.2.2 Tidal Stripping

In addition to RPS, tidal stripping also removes gas from satellite galaxies. Typically, SAMs assume that the fraction of stripped hot gas equals the fraction of dark matter lost by the subhalo (e.g. Guo11 and H15). Therefore,

$$\frac{M_\mathrm{hot}(R_\mathrm{tidal})}{M_\mathrm{hot,infall}} = \frac{M_\mathrm{DM}}{M_\mathrm{DM,infall}}, \tag{3.7}$$

where M_DM is the current mass of the satellite and $M_\mathrm{DM,infall}$ is its virial mass at infall. $M_\mathrm{hot}(R_\mathrm{tidal})$ is the satellite's hot gas mass after tidal stripping has happened and $M_\mathrm{hot,infall}$ is its hot gas mass at infall. For our assumed isothermal density profile, this gives the following expression for the tidal stripping radius

$$R_{\text{tidal}} = \frac{M_{\text{DM}}}{M_{\text{DM,infall}}} R_{\text{hot,infall}} \,, \tag{3.8}$$

where $R_{\text{hot,infall}}$ is the satellite's hot gas radius at infall which is assumed to be $R_{\text{200,infall}}$, since for central galaxies the hot gas radius is set to R_{200}. We only apply tidal stripping to satellite galaxies. Based on our tidal stripping prescription and considering that $M_{\text{DM}} = 0$ after a galaxy becomes a type 2 satellite, as its subhalo is no longer detected, R_{tidal} would be zero for all the type 2 galaxies. Therefore, a galaxy is assumed to be completely empty of hot gas as soon as it becomes a type 2 satellite.

3.2.3   Stripping implementation

For central galaxies, the stripping radius is equal to the ram-pressure stripping radius. For satellite galaxies, however, we take the stripping radius R_{strip} to be the minimum of the tidal and ram-pressure stripping radii. In general, if $R_{\text{strip}} < R_{\text{hotgas}}$, the gas beyond R_{strip} will be lost. After stripping, the density profile of the remaining hot gas is assumed to remain a truncated isothermal.

   Each galaxy in L-Galaxies has an ejected reservoir of gas in addition to its cold and hot gas reservoirs. The mass in the ejected reservoir can either return to the hot gas reservoir or be stripped because of ram-pressure and tidal forces. In this thesis, we take the fraction of mass stripped from the ejected reservoir to be equal to the mass fraction stripped from the hot reservoir. The hot gas stripped from satellites is added to the central hot gas reservoir, and the stripped ejected reservoir from satellites is added to the central ejected reservoir. This treatment is the same as in Guo11 and H15. For central galaxies, gas stripped (from either the hot or ejected reservoirs) is placed in a stripped reservoir, and mass in the stripped reservoir never returns to the galaxy.

3.3   Local Background Environment

3.3.1   Definition

We define the Local Background Environment of each galaxy within a specifically defined spherical shell surrounding its subhalo. Here we are referring to the galaxies which will be produced in L-Galaxies semi-analytical model within dark matter subhaloes. The radii of the background shell are chosen to exclude the galaxy and its subhalo (see §3.3.1). The density of the LBE, ρ_{LBE}, is the number density of simulation particles within this spherical shell multiplied by the particle mass. The nett velocity of the LBE, $\vec{v}_{\text{LBE}}$ is the mean velocity of these shell particles.

   Removing the galaxy and its subhalo from the LBE estimate is critical for our study. Environmental effects such as RPS are not be caused by the galaxy itself; they occur due to a galaxy's movement through its environment, so we need to separate the galaxy/subhalo system from its environment in a clean way. In a simulation, however, the background shell

can contain two species of particles: true LBE particles, and contaminating particles that are associated to the galaxy's own subhalo. The latter are removed, as described below, before deriving the LBE properties.

Defining the background shell size

For galaxies with an identified subhalo, i.e. centrals and type 1 satellites, we choose the inner and outer radii of the shell to be $R_{\text{in}} = \alpha_{\text{in}} R_{\text{subhalo}}$ and $R_{\text{out}} = \alpha_{\text{out}} R_{\text{subhalo}}$, where R_{subhalo} is the subhalo size and is defined as the distance between the most bound and most distant particles of the subhalo, as identified by SUBFIND. α_{in} and α_{out} are coefficients related to the scale of interest for our LBE estimates.

To avoid contaminating the LBE with dark matter from its own subhalo, α_{in} must be greater than 1. In practice, we choose $\alpha_{\text{in}} = 1.25$ to further reduce contamination, making the measurement slightly less compact as a trade-off. In §3.3.2, we discuss the remaining contamination in more detail, and introduce a method to remove it effectively.

The outer radius of the background shell is chosen to be the maximum of $2R_{\text{subhalo}}$ and the radius which encompasses a minimum number of particles, n_{min} in the shell. We choose $n_{\text{min}} = 30$, which gives a statistical error of less than $n_{\text{min}}^{-1/2} \approx 20\%$. For more than half of the subhaloes in MS, $\alpha_{\text{out}} = 2$ satisfies the $n_{\text{min}} = 30$ limit, and less than 1% of subhaloes reach $\alpha_{\text{out}} > 4$; these reside in very low density regions. The typical number of shell particles around satellite galaxies in groups and clusters ranges between a few hundred and a few thousand. Increasing n_{min} much beyond our fiducial choice would force the outer shell radius out to an unacceptably large distance in low density regions for little gain in the accuracy of the local density estimate.

Type 2 satellites (orphan galaxies) are not subject to RPS for hot gas since they have already lost their subhalo along with its hot gas component due to tidal stripping as mentioned earlier in §3.2.2. However, to make our analysis comprehensive, we measure their LBE properties as well, choosing $R_{\text{in}} = 0$. Because type 2 satellites are usually found near the center of FOF haloes (see Fig. 3.7), an accurate density estimate requires a relatively small outer radius. We therefore set R_{out} to be the maximum of $0.04R_{\text{200,host}}$ and the radius which encompasses $n_{\text{min}} = 30$ particles. Increasing/decreasing the outer radius by a factor of 2 does not change the properties of type 2 satellite LBE significantly. Similar to central and type 1 satellite galaxies, there will also be contaminating particles from the galaxy's subhalo when it was last resolved, and we remove this component as described in §3.3.2.

3.3.2 Removing LBE contamination using a Gaussian Mixture Method (GMM)

Removing all the subhalo particles which are identified by the SUBFIND algorithm does not result in a background shell being completely emptied of subhalo-associated particles. These near-members may be on the edge of gravitational boundedness, and typically move with a velocity that is close to the velocity of the subhalo itself, but which is significantly

different than true background particles in the shell. Their classification as members of the subhalo is largely a matter of definition, i.e. a detail of the SUBFIND algorithm, but for the purposes of classifying the true LBE, we aim to identify them as part of the subhalo itself.

We adopt a model in which the background shell of each subhalo is formed by two different species of particles. The first species consist of particles with approximately the same mean velocity and velocity dispersion as the subhalo. The second species, the true LBE particles, have unknown mean velocity and velocity dispersion.

We wish to derive the fraction of each particle species and hence the density of each species in the shell, as well as the mean velocity (3 dimensional) and 1D velocity dispersion of the LBE particles. We consider the distribution of the velocity of each species to be a Gaussian, with known mean and dispersion for the subhalo particles, and unknown mean and dispersion for LBE particles. We write the distribution of the velocities of shell particles as a Gaussian mixture

$$
\begin{aligned}
P(v) = & f_{\mathrm{sub}} \left(2\pi\sigma_{\mathrm{subhalo}}\right)^{-3/2} \exp\left(-\frac{|\vec{v} - \vec{v}_{\mathrm{subhalo}}|^2}{2\sigma_{\mathrm{subhalo}}^2}\right) \\
& + (1 - f_{\mathrm{sub}}) \left(2\pi\sigma_{\mathrm{LBE}}\right)^{-3/2} \exp\left(-\frac{|\vec{v} - \vec{v}_{\mathrm{LBE}}|^2}{2\sigma_{\mathrm{LBE}}^2}\right).
\end{aligned}
\tag{3.9}
$$

Here, $\vec{v}_{\mathrm{subhalo}}$ and $\vec{v}_{\mathrm{LBE}}$ are the mean velocities of the subhalo and its LBE, while $\sigma_{\mathrm{subhalo}}$ and σ_{LBE} are their corresponding 1D velocity dispersion. For resolved subhalos, $\vec{v}_{\mathrm{subhalo}}$ and $\sigma_{\mathrm{subhalo}}$ are measured using the particles which are identified as subhalo particles by SUBFIND algorithm. For type 2 galaxies which have no identified subhalo, $\vec{v}_{\mathrm{subhalo}}$ is considered as the current velocity of the most bound particle and $\sigma_{\mathrm{subhalo}}$ the velocity dispersion of the subhalo when it was last resolved. f_{sub} is the fraction of particles in the background shell that belong to the subhalo. Eq. 3.9 contains 5 unknown variables, $f_{\mathrm{sub}}, \vec{v}_{\mathrm{LBE}}$ (3 components) and σ_{LBE}. To proceed, we write down the first and second moments of the velocity of shell particles

$$
< \vec{v}_{\mathrm{shell}} > = f_{\mathrm{sub}} < \vec{v}_{\mathrm{subhalo}} > + (1 - f_{\mathrm{sub}}) < \vec{v}_{\mathrm{LBE}} >,
\tag{3.10}
$$

$$
< |\vec{v}_{\mathrm{shell}}|^2 > = f_{\mathrm{sub}} < |\vec{v}_{\mathrm{subhalo}}|^2 > + (1 - f_{\mathrm{sub}}) < |\vec{v}_{\mathrm{LBE}}|^2 >.
\tag{3.11}
$$

In these four equations, $< \vec{v}_{\mathrm{shell}} >$ and $< |\vec{v}_{\mathrm{shell}}|^2 >$ can be computed directly from the shell particles, while the values of $< \vec{v}_{\mathrm{subhalo}} >$ and $< |\vec{v}_{\mathrm{subhalo}}|^2 >$ are known. This leaves us with 4 equations and 5 unknowns. To solve for f_{sub} we use a maximum log-likelihood method for the velocity distribution of shell particles according to Eq. 3.9. The log-likelihood can be written as

$$
L = \prod_{i=1}^{N} P(v_i) \quad \Rightarrow \quad \ln L = \sum_{i=1}^{N} \ln P(v_i),
\tag{3.12}
$$

where the sum is over all of the shell particles (N particles in total). Enforcing the constraint that $0 \leq f_{sub} \leq 1$, we numerically maximize the likelihood via a grid search and derive the fraction of subhalo particles for each shell.

Given f_{sub}, we can calculate the velocity, velocity dispersion, and density of the LBE. We define the shell density as the average density of the shell

$$\rho_{shell} = \frac{1}{V_{shell}} \sum_{i=1}^{N} m_i \quad , \quad V_{shell} = \frac{4}{3}\pi(R_{out}^3 - R_{in}^3), \tag{3.13}$$

where m_i is the mass of each particle inside the shell and V_{shell} is the shell volume. Hence, the LBE density is

$$\rho_{LBE} = (1 - f_{sub})\rho_{shell}. \tag{3.14}$$

In addition, the mean LBE velocity is driven from Eq. 3.10, and is

$$\vec{v}_{LBE} = \frac{< \vec{v}_{shell} > - f_{sub}\vec{v}_{subhalo}}{1 - f_{sub}}. \tag{3.15}$$

Finally, the velocity of a galaxy relative to its LBE becomes

$$\vec{v}_{gal,LBE} = \vec{v}_{gal} - \vec{v}_{LBE}, \tag{3.16}$$

where $\vec{v}_{gal}$ is the velocity of the galaxy, as determined by the average over its constituent subhalo particles, i.e. $\vec{v}_{gal} = \vec{v}_{subhalo}$ for central and type 1 satellite galaxies. For type 2 satellites, which have no subhalo, $\vec{v}_{gal}$ is the current velocity of the galaxy, which is identified with the most bound particle of its subhalo at the last time this was identified.

Fig. 3.1 visualizes the 2D projected velocity distribution of particles in the background shell of two different type 1 satellite galaxies. Each row shows one galaxy, and the three panels in each row present projections in the x-y, x-z and y-z planes. The component mixture can clearly be seen for both galaxies. The circles are centered at the Gaussian mixture method's predictions for the velocities of the galaxy (cyan circles) and its LBE (white circles). The solid circles show the velocity dispersion of each particle species, which broadly encloses the most populated velocity bins. The two cases presented in Fig. 3.1 have contamination values of $f_{sub} = 0.22$ and $f_{sub} = 0.10$.

To illustrate the influence of decontaminating the background shell we compare the velocity of the shell for the galaxy in the top panel of Fig. 3.1 before and after decontamination. In the rest frame of its host FOF halo, the mean velocities in each of the three Cartesian directions of this satellite's background shell before decontamination are $\vec{v}_{shell} \simeq (-142, 62, -170)$ km/s. After decontamination, the mean velocities of the LBE are $\vec{v}_{LBE} \simeq (59, 79, 183)$ km/s. This strong difference between shell velocity and LBE velocity, both in magnitude and orientation, shows the importance of decontaminating the background shell.

To provide a sense of the level of contamination in our background shells, the average and median values derived for f_{sub} along with its distribution are shown in Fig. 3.2. The
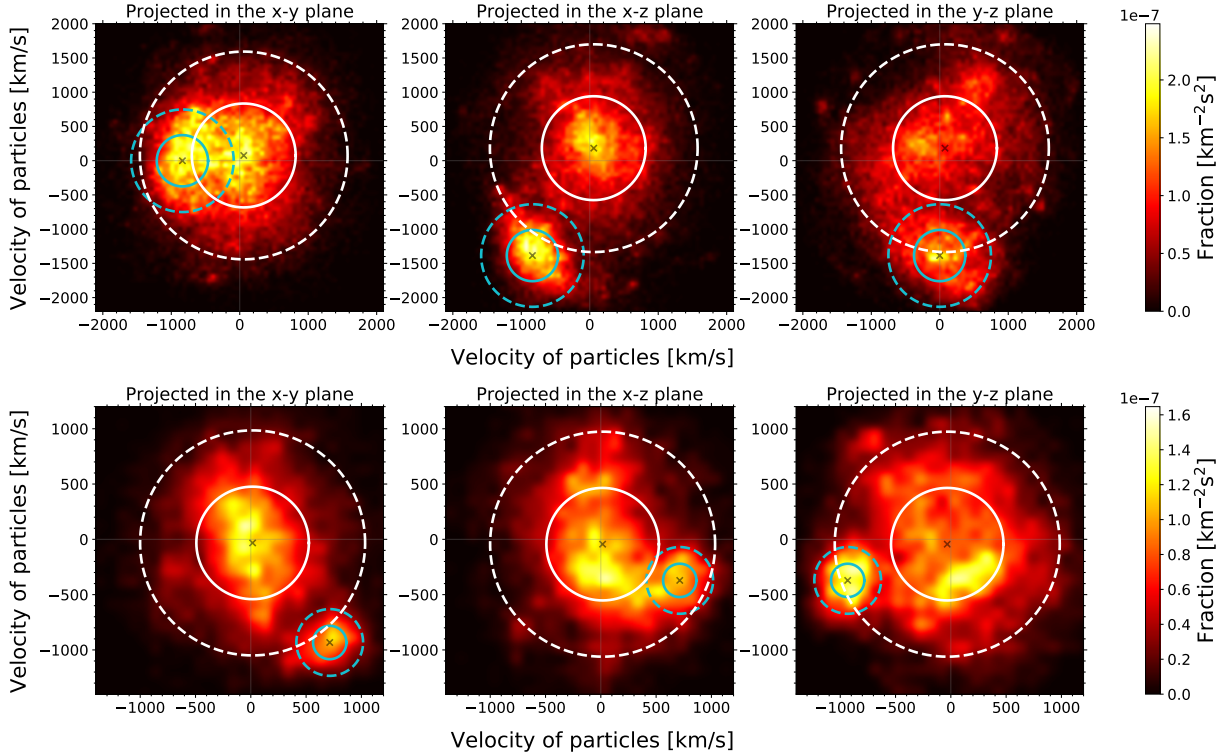
Figure 3.1: Distribution of the velocity of particles in the background shell of two satellite galaxies (each row shows one galaxy), containing 60,000 and 8,000 particles, respectively. The three panels in each row correspond to three different projections of the 3D velocity distribution in the x-y, x-z and y-z planes. The velocities are reported in the rest frame of the satellite galaxy's host halo. The colours show the fraction of particles in each velocity pixel. The cyan circles are centered at the velocity of the galaxy, and the white circles are centered at the derived mean velocity of the LBE after decontamination. The radius of solid circles is equal to velocity dispersion of the two modelled Gaussians, while dashed circles show twice that value. The center of circles are marked by cross signs and the thin vertical and horizontal grey lines show the origin at (0,0). The fraction of contaminant particles in the top panel is 0.22 and 0.10 in the bottom panel. The magnitude and direction of the LBE velocity vectors are strongly affected by our decontamination procedure (see text).
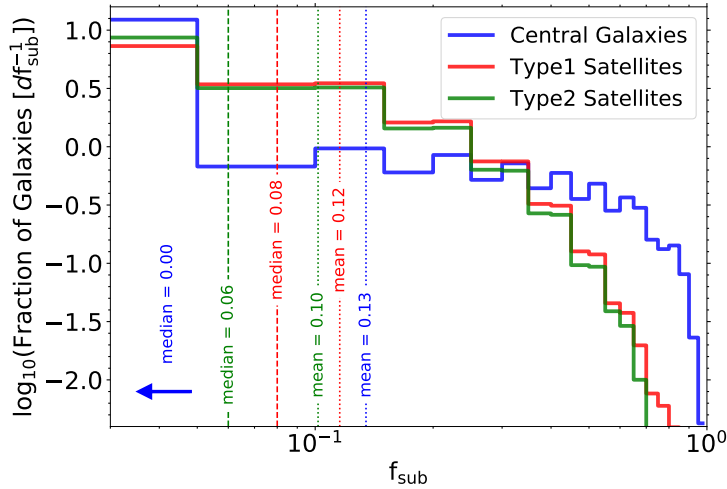
Figure 3.2: Distribution of the fraction of contaminant particles (subhalo particles), f_{sub}, in the background shell of galaxies. The blue lines illustrate central galaxies, while red and green lines correspond to type 1 and type 2 (orphan) satellite galaxies. Solid lines show the fraction of contaminants divided by the size of each bin. Dashed and dotted lines denote median and mean values of f_{sub}, which are also labeled with their value in the figure.

y-axis illustrates the fraction of galaxies divided by the size of each bin and the x-axis denotes the value of f_{sub}. The substantial difference between mean and median values for central galaxies reflects the large tail to high contamination fraction. Half of all central galaxies have $f_{sub} = 0$. In contrast, in type 1 satellites, the median and mean values for f_{sub} are significantly closer to each other and are around 0.1. For type 2 satellite galaxies, however, the contamination is not as strong as type 1 satellites.

3.3.3 The Density and Velocity of LBE Hot Gas

The LBE represents the total matter background density around galaxies as we are using the Millennium simulation. Therefore, it must be translated into a hot gas density for the purpose of computing the ram-pressure stripping. For central galaxies, we multiply the total density within the LBE shell by the cosmic baryon fraction Ω_b. For satellite galaxies, the hot gas density is taken to be the total LBE density multiplied by f_{hotgas}, the hot gas fraction of the associated main subhalo of their FOF halo:

$$
\begin{aligned}
\rho_{LBE,hotgas} &= \Omega_b \, \rho_{LBE} \qquad &\text{(Central Galaxies)} \\
\rho_{LBE,hotgas} &= f_{hotgas} \, \rho_{LBE} \qquad &\text{(Satellite Galaxies).}
\end{aligned}
\tag{3.17}
$$

In both cases we therefore assume that gas traces dark matter linearly, as commonly adopted by semi-analytic models (including L-Galaxies) to model the diffuse baryon components of haloes and subhaloes. With this assumption, the velocity of the LBE gas would be the same as the mean velocity of LBE derived from the dark matter particles.
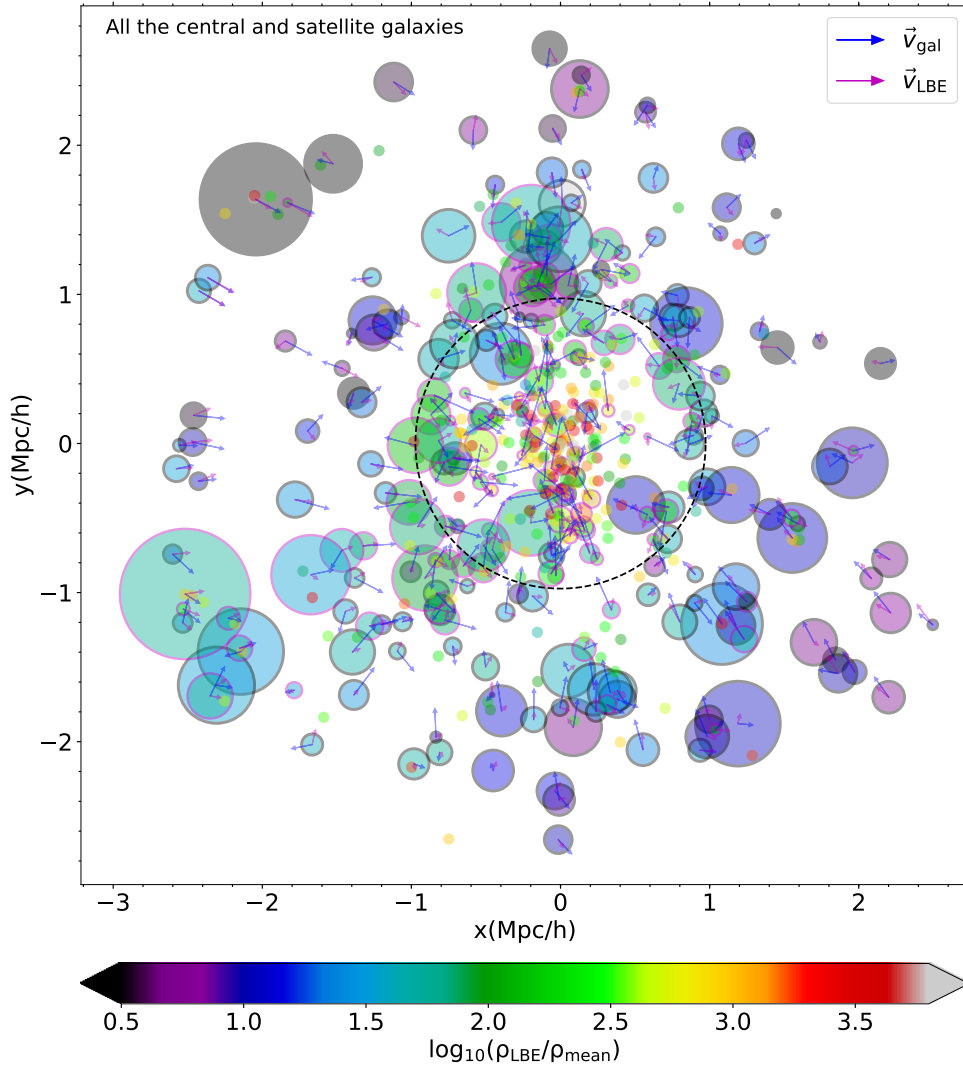
Figure 3.3: Environmental properties of the galaxies within $3 \times R_{200}$ of a massive halo with $M_{200} \approx 10^{14} \mathrm{M}_\odot/\mathrm{h}$ at redshift zero. Each circle shows a galaxy, and there are in total 582 galaxies visible, of which 169 are centrals, 120 are type 1 satellites and 293 are type 2 satellites. We note that the stellar mass limit, $M_\star = 3 \times 10^9 \mathrm{M}_\odot/\mathrm{h}$, is not applied in this figure. The face-colour of each circle corresponds to the local background density (in the units of mean density of the universe) and its edge colour specifies the galaxy's type: grey for centrals (type 0), red for type 1 satellite, and no edge colour for type 2 satellites. The size of circles is equal to the subhalo size for type 0 and type 1 galaxies, while type 2 satellite galaxies are simply shown as dots. The dashed black circle around the center corresponds to R_{200} for the main halo. The arrows illustrate the velocities for type 0 and type 1 galaxies, where the length of each arrow is proportional to the magnitude of the velocity. The length of the arrows shown in the key is $0.1\mathrm{Mpc/h} \equiv 600\mathrm{km/s}$. Blue arrows show galaxy velocities in the rest frame of the main halo, and the magenta arrows show the local background velocities in the rest frame of the main halo. For type 2 galaxies, the velocities are plotted separately in Fig. 3.4.
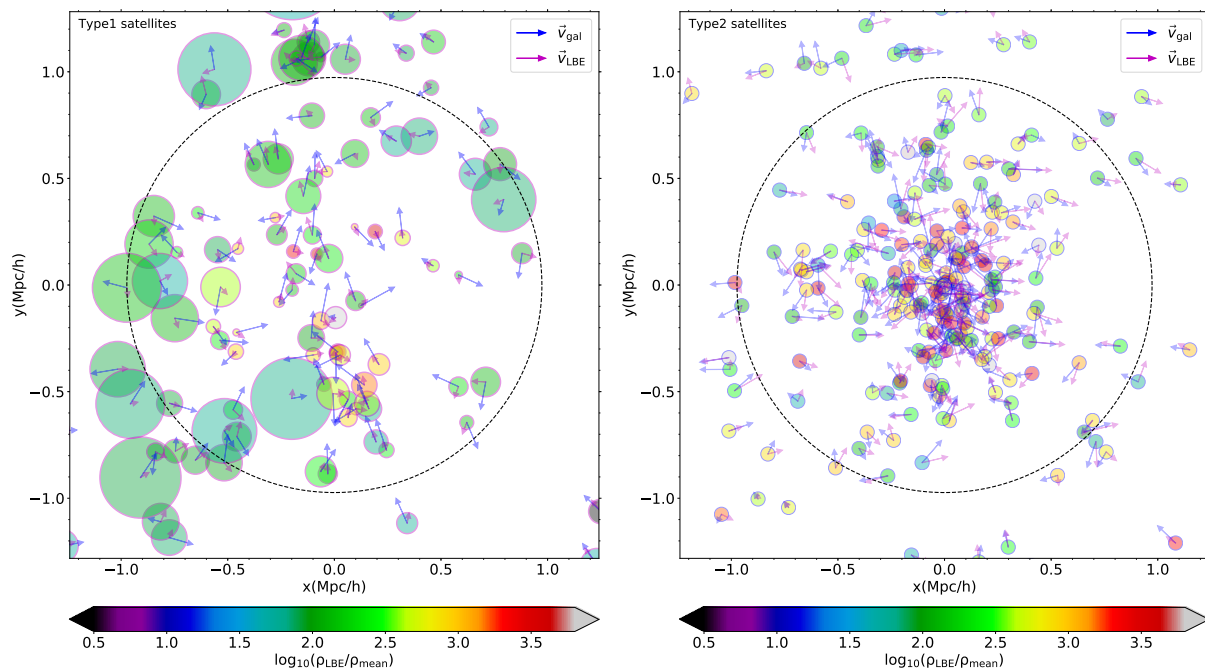
Figure 3.4: This figure has the same format as Fig. 3.3, but is meant to contrast the locations and properties of type 1 vs type 2 in the same massive halo, zoomed into smaller scales of $\sim 1.2R_{200}$. The left panel shows type 1 satellite galaxies and the right panel shows type 2 satellites. We note that the stellar mass limit, $M_\star = 3 \times 10^9 \mathrm{M}_\odot/\mathrm{h}$, is not applied in this figure. The velocity arrow scale is $0.1\mathrm{Mpc/h} \equiv 1200\mathrm{km/s}$. Comparing the two panels, type 2 galaxies mostly populate in the innermost regions, near the center of the main halo, and typically have higher background densities, in contrast to their type 1 counterparts.

We note that the LBE could be measured using the local gas directly from a hydrodynamic simulation as well. However, for our implementation in L-GALAXIES, we measure it from the dark matter simulation on which the SAM is run.

One of the greatest advantages of the LBE measurements we introduced here is the fact that the LBE is measurable for all the galaxies, removing artificial boundaries in space (e.g. the halo boundary), redshift and halo mass. We note that measuring LBE properties directly from a dark matter only simulation and then connecting them to the LBE gas properties with a formalism such as the one we described above undoubtedly neglects some aspects of the hydrodynamic interactions (e.g. Oppenheimer 2018). Indeed, not all aspects of how gas traces dark matter can be completely addressed yet, even in full magnetohydrodynamic simulations.

Fig. 3.3 illustrates the rich output of the LBE method for the galaxies in the vicinity of a single massive halo. Environmental properties are shown for all of the galaxies within $3 \times R_{200}$ of a halo with $M_{200} \approx 3 \times 10^{14} M_\odot/h$ at redshift zero in the (scaled) Millennium Simulation. Each circle shows one galaxy, where the circle size equals the subhalo size for central (black edge colour) and type 1 satellite galaxies (red edge colour). Type 2 satellites (no edge colour) are simply shown as dots. The dashed black circle around the center corresponds to R_{200} of the main halo. The arrows illustrate the velocities for central and type 1 satellite galaxies; the length of each arrow is proportional to the magnitude of the velocity. Blue arrows are the galaxy velocities, and the magenta arrows are the LBE velocities (both in the rest frame of the main halo).

Fig. 3.4 contrasts the locations and properties of type 1 vs type 2 satellites in the same halo, zoomed into a smaller scale of $1.2R_{200}$. The left panel shows type 1 satellite galaxies and the right panel shows type 2 satellites.

We point out several features of interest in Figs. 3.3 and 3.4. First, the LBE density generally decreases with distance from the halo center, although the lack of radial symmetry is clear. In addition, the galaxies move faster than their LBE – for each galaxy, the blue arrow is usually longer than the magenta one. More importantly, the LBE is not completely at rest relative to its host. We also note that $\vec{v}_{\mathrm{gal}}$ and $\vec{v}_{\mathrm{LBE}}$ are more aligned for galaxies that are far away from the halo center. Near the halo center, the angle between them is statistically more uniform. Furthermore, galaxies in high density regions move faster with respect to their local background environment. We quantitatively explore these features further in §3.4.

3.3.4   'Decontaminated' subhalo mass function

Our decontamination method (discussed in §3.3.2) changes the estimate of the subhalo mass, by assigning additional particles beyond the fiducial membership association determined by SUBFIND[1]. To assess the magnitude of this change, we set the inner radius of the background shell to $R_{\mathrm{in}} = R_{\mathrm{subhalo}}$, to capture the most possible contamination, and

---

[1]Although we investigate the subhalo mass after decontamination, we will continue using the subhalo masses found by SUBFIND in the rest of the chapter.
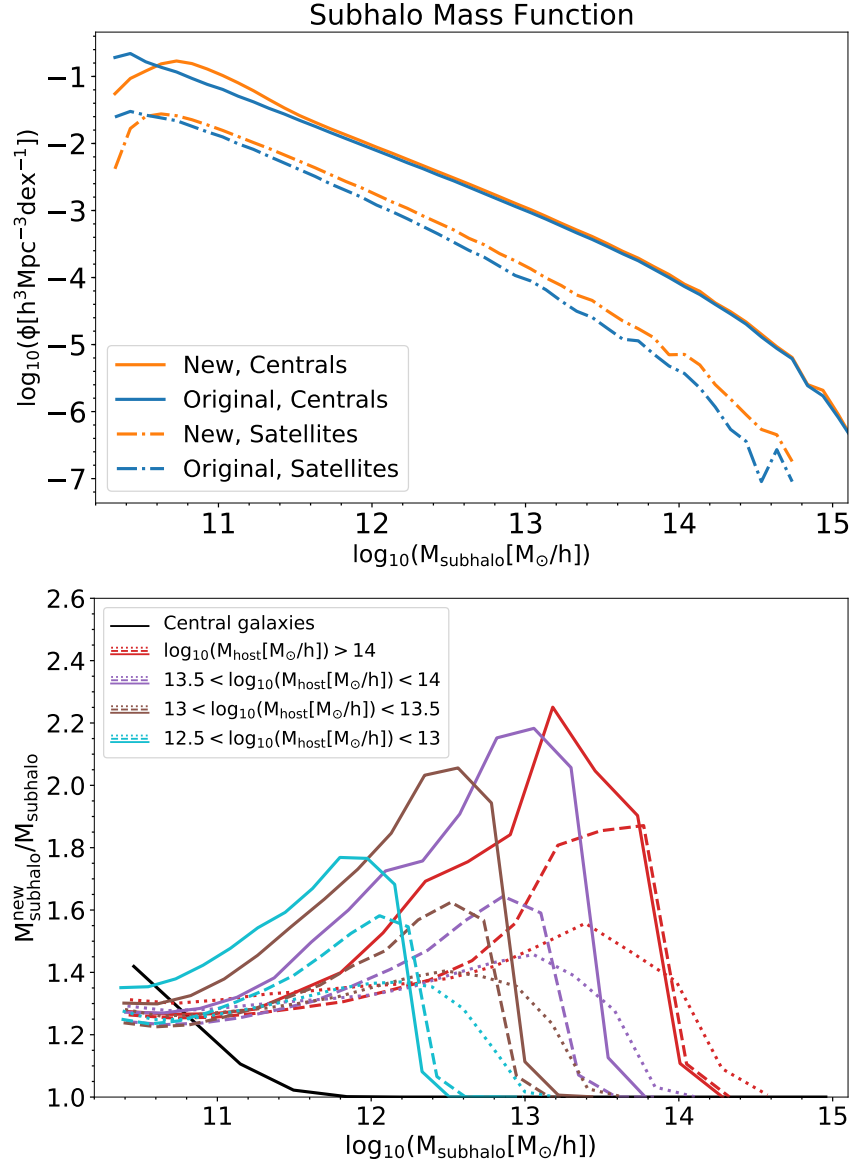
Figure 3.5: Top panel: comparison of the subhalo mass function estimated using the SUBFIND algorithm (blue) versus our modified mass function (orange). Solid lines include only central subhaloes, while dash-dot lines show satellites. Bottom panel: the median values of the ratio of updated versus original subhalo masses as a function of the original masses. Solid coloured lines correspond to the satellites within $0.5R_{200}$ of their FOF halo, dashed lines include $0.5 < R/R_{200,\text{host}} < 1$, and dotted lines show satellites beyond R_{200}. No mass limits are applied.

keep the outer radius unchanged. We then add the fraction of subhalo particles in the background shell of each subhalo to its mass:

$$M_{\text{subhalo}}^{\text{new}} = M_{\text{subhalo}} + f_{\text{sub}} M_{\text{shell}}, \qquad (3.18)$$

where M_{shell} is the mass of background shell and f_{sub} is the fraction of particles in the background shell which belong to the subhalo. We show the correspondingly updated subhalo mass function for the Millennium simulation for central and satellite subhaloes in the top panel of Fig. 3.5. The orange lines show our new subhalo mass function and blue lines show the original results of SUBFIND. The solid and dashed lines represent central and satellite subhaloes. The mass function of satellite subhaloes is more affected than centrals. The bottom panel of Fig. 3.5 illustrates the ratio of new to old mass for central subhaloes (black line) and satellites within FOF haloes of different masses (coloured lines).

Our results show that the subhalo mass increases somewhat for low mass centrals, $\log_{10}(M_{\text{subhalo}}[\text{M}_\odot/\text{h}]) < 12$, but remains unchanged for more massive centrals. For satellite subhaloes, the changes are much larger, and increasing with increasing subhalo mass. For some subhaloes, the mass can increase by more than a factor of two. The bottom panel of Fig. 3.5 shows that, at fixed subhalo mass, the mass increase is larger in lower mass FOF haloes. The bottom panel also shows that the increase in mass is larger for satellite galaxies near the center of FOF haloes (solid lines) and smaller for the ones farther away from the center (dashed and dotted lines).

We note that the masses of the most massive satellite subhaloes (the right tail of coloured curves) increase by a small fraction if at all. These are satellite subhaloes which are massive enough, compared to their host FOF, to be considered as centrals. The subhalo finder algorithm labels them as satellites because, by definition, each FOF halo can only have one central subhalo. By construction, a satellite subhalo can also not exceed the mass of its central. It is thus natural that the change in subhalo mass for these objects drops to the same value as for central subhaloes, even though they are categorized as satellites.

3.4 Analysis of LBE properties

In this section, we analyze the statistical properties of the LBE. We look for correlations between the LBE and subhalo properties including mass, type (central or satellite), position within the parent FOF halo, and mass of the host FOF halo (for satellites). This provides a first hint of the importance of ram-pressure stripping as a function of these same properties.

3.4.1 Correlation of LBE with subhalo mass

Fig. 3.6 depicts galaxy velocity with respect to the local environment, $v_{\text{gal,LBE}}$ (top panel), density ρ_{LBE} (middle panel) and ram-pressure force P_{rp} (bottom panel) as a function of subhalo mass for central and type 1 satellite galaxies at $z = 0$ in the Millennium Simulation. In all the panels, black solid lines show medians for central galaxies, and coloured lines given
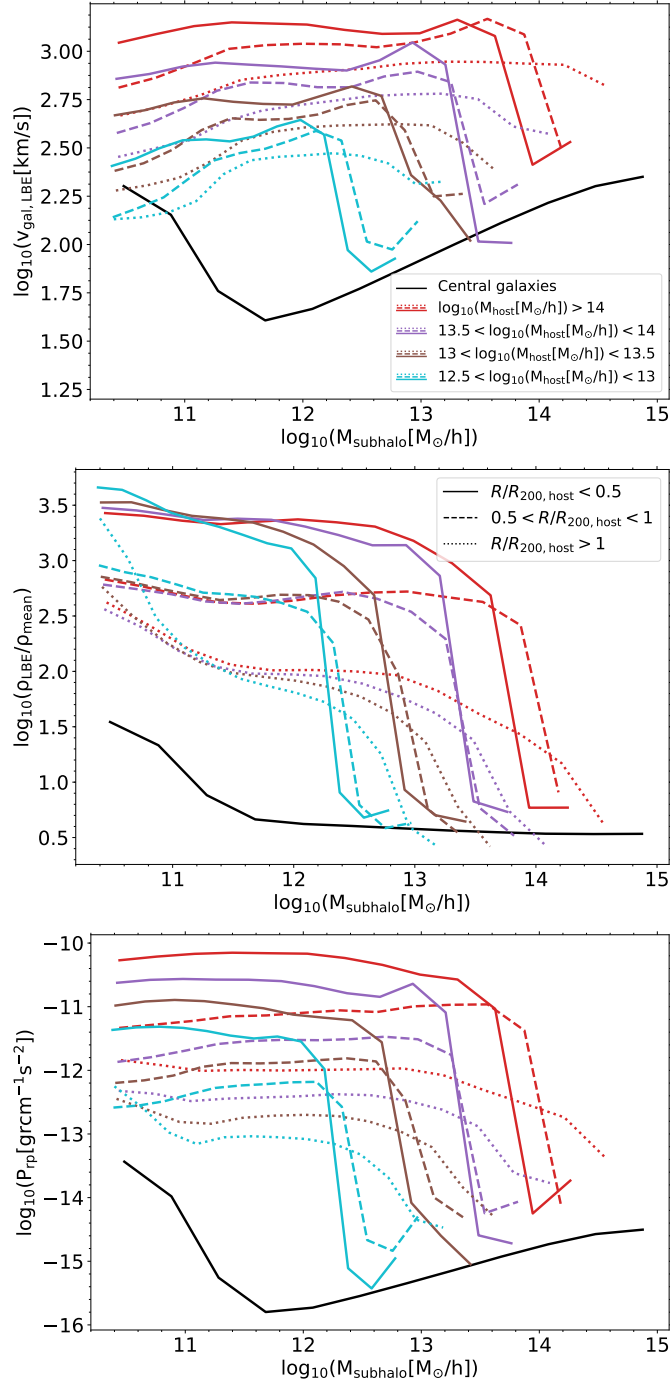
Figure 3.6: The velocity of galaxies relative to their LBE (top panel), the LBE density (middle panel) and ram-pressure force (bottom panel) as a function of subhalo mass for all of the subhaloes at $z = 0$. The black solid line corresponds to central galaxies, while the coloured lines show satellites. Solid coloured lines include satellites within $0.5R_{200}$ of the centre of the FOF halo, dashed lines are for $0.5 < R/R_{200,\mathrm{host}} < 1$ and the dotted lines show satellites beyond R_{200}.

medians for satellite galaxies, where different colours denote different host halo masses: within $R_{200}/2$ (solid), with $0.5 < R/R_{200} < 1$ (dashed), and beyond R_{200} (dotted).

For satellite galaxies, the trends of all the three physical quantities have a weak dependence on subhalo mass up to a threshold mass, beyond which there is a sharp drop. This drop happens, as before, when the subhalo mass approaches that of the central subhalo, and these massive subhaloes become equivalent to centrals in terms of their properties. Binary subhaloes at the center of a FOF halo are expected to merge, but before they do so, one subhalo will be classified as a central and the other as a satellite of much lower mass.

We also see that ρ_{LBE} has a weak dependency on the host mass for low mass satellite galaxies, whereas $v_{\mathrm{gal,LBE}}$ increases strongly with host mass, indicating that satellites of more massive haloes move faster relative to their LBE. The same trend is seen for the ram-pressure since it is proportional to $v_{\mathrm{gal,LBE}}^2$. Indeed, the median ram-pressure force is a factor of 10 larger for satellites within massive clusters of $10^{14} M_\odot$ than for satellites within groups of $10^{12} - 10^{13} M_\odot$. There is also a significant dependence of all three quantities on distance from the center of the host halo. We note that this distance dependence is much stronger for ρ_{LBE} than for $v_{\mathrm{gal,LBE}}^2$. Moreover, for $v_{\mathrm{gal,LBE}}$, this trend is stronger in more massive haloes.

3.4.2   LBE properties versus distance

As seen in the previous section, the LBE in the vicinity of satellite galaxies changes with the distance from the centre of the FOF halo as well as with the mass of the FOF halo. To investigate this in more detail, we extend our study out to $5R_{200}$ around each FOF halo and consider all galaxies contained in that volume.

Fig. 3.7 shows the distribution of the three different galaxy types as a function of their distance from the center of each FOF halo. The curves are normalized to the total number of galaxies in each distance bin, such that the sum of three curves is equal to unity. It can be seen that the type 2 satellites dominate close to the center of the FOF halo, while beyond R_{200} they form about 10% of the population. In contrast, type 1 satellites are most frequent at radii $0.5 < R/R_{200} < 2.5$. Central galaxies start to be dominant from $\approx 2.5R_{200}$. Around $R > 3.5R_{200}$ the distributions no longer vary with distance. At these large radii, there are approximately 65% centrals, $\sim 25\%$ type1 satellites and $\sim 10\%$ type 2 satellite galaxies, and these fractions are insensitive to central halo mass.

We continue by investigating how $v_{\mathrm{gal,LBE}}$ and ρ_{LBE} change as a function of distance from the center of the FOF halo. The results are shown in four bins of FOF halo mass M_{200} in Fig. 3.8, which illustrates $v_{\mathrm{gal,LBE}}$ (top 4 panels) and $\rho_{\mathrm{gal,LBE}}$ (bottom 4 panels) as a function of distance to the centre of the FOF haloes. We use bins of width $0.1/R_{200,\mathrm{host}}$ in distance, and normalize all the pixels at each distance to the maximum value at that distance. In addition, the 1σ (68%) and 2σ (95%) points of the galaxy distribution at each radius are indicated by red and white contours, while the brown dashed lines show the median value. We combine all three galaxy types together in this and the following figures.

Comparing the top four panels in Fig. 3.8, we see that, at small radii, the median
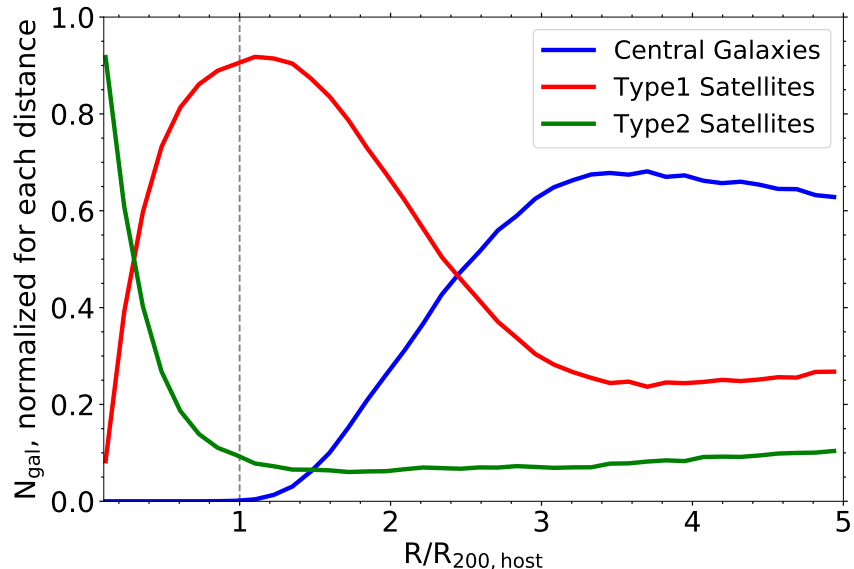
Figure 3.7: Distribution of different types of galaxies in L-Galaxies as a function of distance from the centre of FOF haloes. Blue lines correspond to central galaxies and red (green) lines to type 1 (type 2) satellite galaxies. At each distance, the sum of the three curves is normalized to unity.

value of $v_{\mathrm{gal,LBE}}$ increases with the host mass, reflecting the fact that velocity dispersion is higher in more massive haloes. We recall that $v_{\mathrm{gal,LBE}}$ is the velocity of a galaxy relative to its local background environment. Comparing the bottom four panels, we see that the median background density shows a weaker dependence on the host mass. However, the distribution of density exhibits more scatter at large distances, particularly in the vicinity of massive compared to low mass haloes. Distant galaxies with high LBE densities are mostly satellites (of other parent haloes). Our additional analysis shows that at $R/R_{\mathrm{200,host}} = 5$, the background density around satellite galaxies is ~ 2 dex larger than around centrals at the same distance. At large distances $v_{\mathrm{gal,LBE}}$ is also considerably different for central and satellite galaxies. Central galaxies move a factor of two slower relative to their LBE compared to satellites at a distance of $5R_{200}$.

Interestingly, from Fig. 3.8 it can be seen that both $v_{\mathrm{gal,LBE}}$ and ρ_{LBE} show quite continuous behavior at all scales, including across R_{200} (dashed black line). This implies that there is no abrupt truncation of environmental effects such as ram-pressure stripping at the virial radius, at least in the population average sense.

We now turn to a comparison of the motion of galaxies with respect to the motion of their LBEs. Fig. 3.9 shows how $\vec{v}_{\mathrm{LBE}}$ and $\vec{v}_{\mathrm{gal}}$ differ in magnitude and orientation. The colours and contours are the same as in Fig. 3.8. The top panels demonstrate that the LBE velocity is on average larger than $v_{\mathrm{gal}}/4$ in the centers of haloes. It is clear that the common assumption of a LBE for satellite galaxies that is at rest with respect to the hosts (e.g. Stevens et al. 2016a; Simpson et al. 2018) does not hold in general.
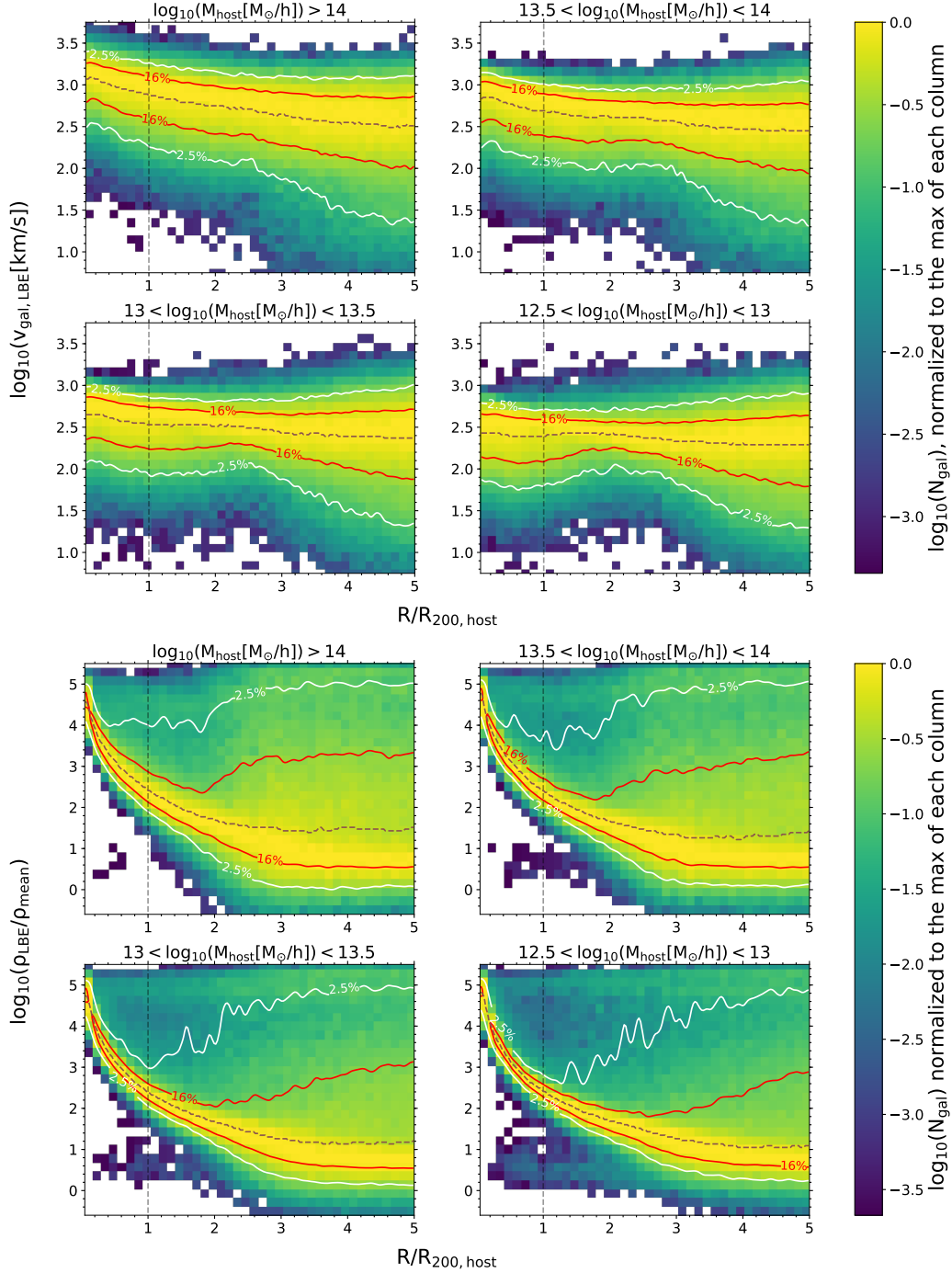
Figure 3.8: Distribution of galaxy velocities relative to their LBE (top 4 panels) and LBE density (bottom 4 panels) as a function of distance from the centre of the host halo. Each group of 4 panels shows results for four different FOF host halo mass bins, and we include all galaxies out to $5R_{200,\mathrm{host}}$. The colour table is logarithmic and values at each distance column are normalized to the maximum value of that column. Red and white contours encompass the $1\sigma(\approx 68\%)$ and $2\sigma(\approx 95\%)$ variation in properties at each distance. The brown dashed line shows the median value at each distance and the vertical gray dashed lines mark the virial radius.
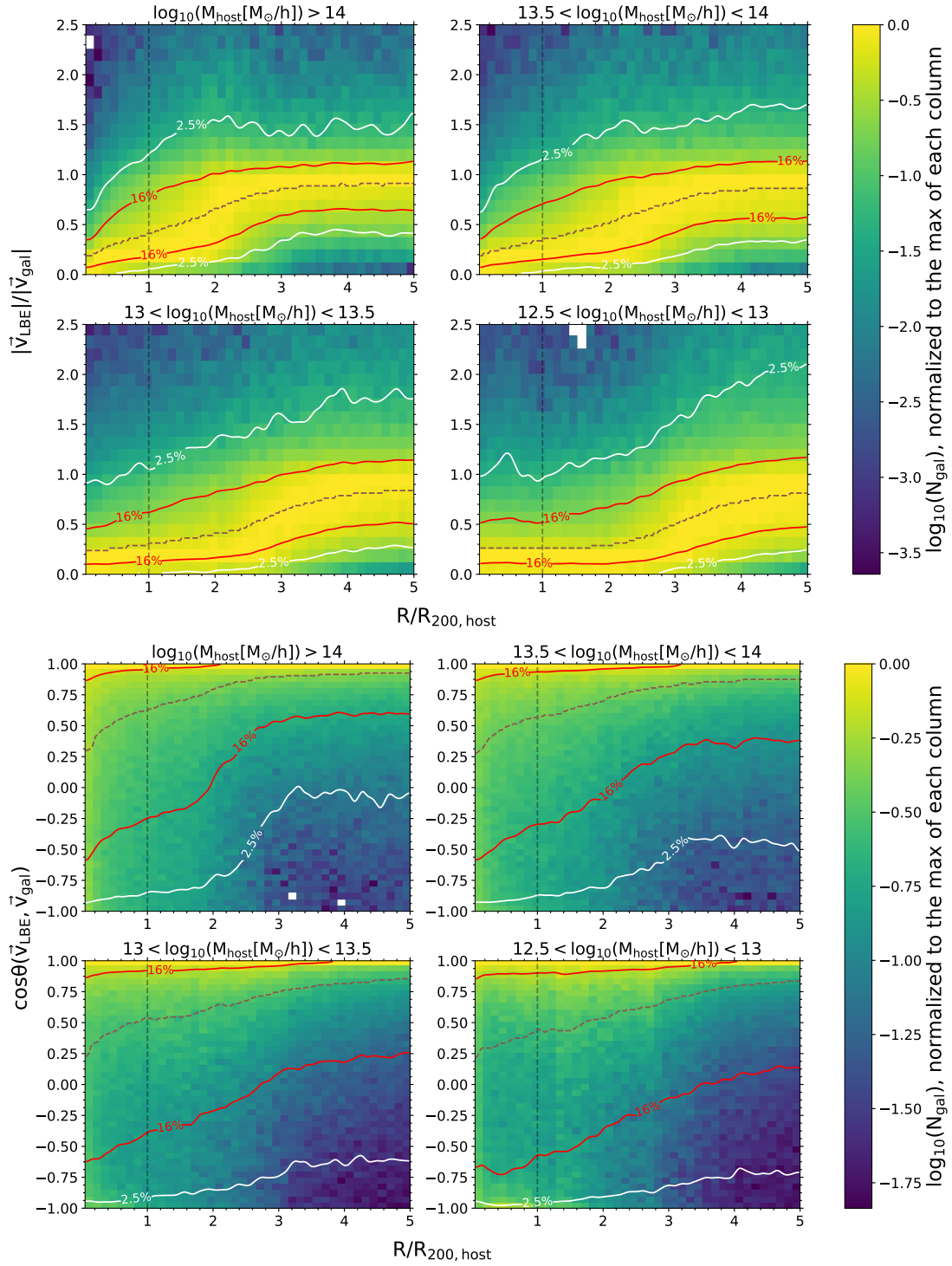
Figure 3.9: Distribution of the ratio (top panels) and angle (bottom panels) between LBE velocity and galaxy velocity (both in the rest-frame of central host halo) as a function of distance from the centre of the host halo. The format is the same as in Figure 3.8.

In all four mass bins, the velocity of the LBE at large distance asymptotically approaches a characteristic value of $\sim 80\%$ of the galaxy velocity itself. This value is reached only at progressively larger distances when normalizing by R_{200}, for lower mass haloes. Near massive haloes, we interpret this as a signature of coherent infall, with galaxies and their surrounding dark matter accreting at similar velocities.

The four bottom panels in Fig. 3.9 show the angle between $\vec{v}_{\mathrm{gal}}$ and $\vec{v}_{\mathrm{LBE}}$, both in the rest frame of the central FOF halo. At larger distances ($R \gtrsim R_{200,\mathrm{host}}$), the two noted velocities are frequently aligned in the same direction – as explained above, both the galaxy and its surrounding material move coherently in the same direction towards a nearby massive halo or mass concentration. This large-scale alignment is more pronounced around more massive centrals, as expected.

The distribution of angles becomes more uniform as $R \to 0$, reflecting the fact that the subhalo orbits become isotropized close to the center of haloes. The median stacked cosine of the relative angle drops below $1/2$ roughly within R_{200}. Even at the halo center, however, the $\cos(\theta)$ distributions do not become entirely symmetric about zero, showing that the dynamical states of groups and clusters are in general not fully relaxed.

3.4.3 Galaxy velocity versus density

Finally, we examine how the galaxy's speed relative to its LBE changes with LBE density. Fig. 3.10 shows $v_{\mathrm{gal,LBE}}$ as a function of ρ_{LBE}, for all galaxies within $5R_{200}$, stacking around central objects in the same four mass bins as before. At the centers of haloes, roughly independent of host mass, there is a residual ~ 100 km/s motion between galaxies and their local background.

We find that the median relative velocity of galaxies with respect to their LBE increases steeply with LBE density in low density regions, i.e. $\log(\rho_{\mathrm{LBE}}/\rho_{\mathrm{mean}}) \lesssim 1.5$. In higher density regions, on the other hand, $v_{\mathrm{gal,LBE}}$ is only weakly dependent on LBE density. However, at these high densities, galaxy velocity shows significant correlation with FOF halo mass. We note that the density where $v_{\mathrm{gal,LBE}}$ becomes constant corresponds roughly to the density where galaxies are expected to be infalling for the first time. Notably, the imprint of local density on $v_{\mathrm{gal,LBE}}$ is much more apparent than the imprint of radius from the FOF halo center, where these two regimes were much less clearly evident.

3.5 Results of L-Galaxies with our new stripping model

The majority of galaxies in the simulation are either central galaxies or satellites which reside beyond R_{200} of the more massive FOF haloes. At $z = 0$ of our L-Galaxies run on MS, about 20% of all galaxies are satellites within R_{200} of FOF haloes. As we have shown in §3.4, LBE properties are generally continuous across R_{200}, motivating our extension of RPS to all galaxies in the simulation regardless of type or location. As a result, the bulk of the galaxy population will be newly affected by stripping.
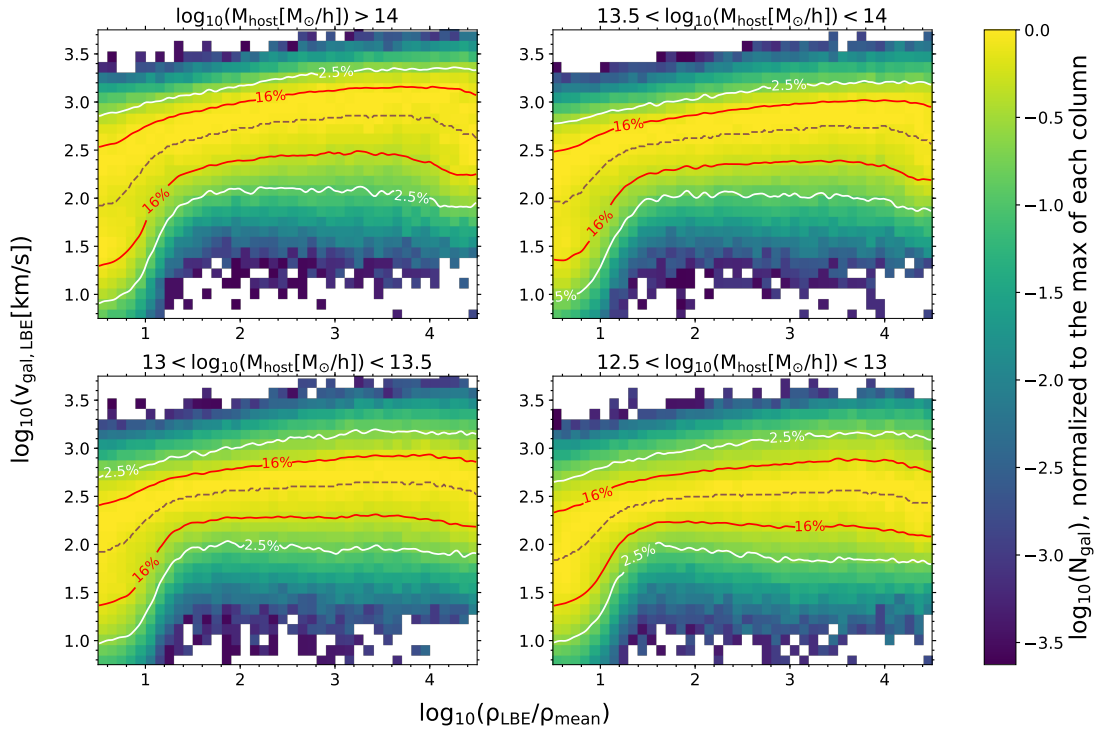
Figure 3.10: Distribution of the velocity of galaxies relative to their LBE as a function of their LBE density. The format of the panels is the same as in Figure 3.8. To first order density traces distance, and only in low-density regimes $\log(\rho_{\mathrm{LBE}}/\rho_{\mathrm{mean}}) \lessapprox 1.5$ does $v_{\mathrm{gal,LBE}}$ increase strongly with background density. This threshold overdensity roughly corresponds approximately to galaxies on first infall.
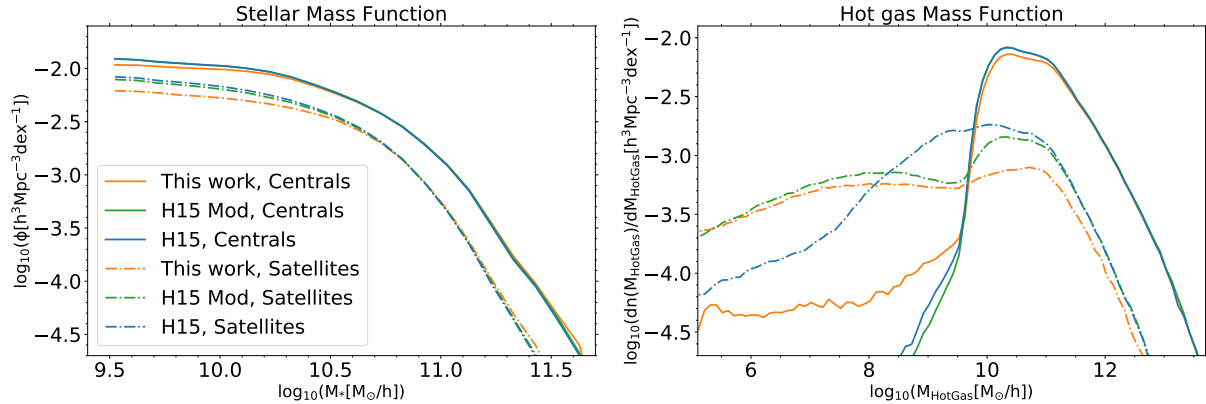
Figure 3.11: Stellar mass function (left panel) and hot gas mass function (right panel) for galaxies at $z = 0$. The orange line shows results from our new model, while green and blue lines show the outcomes of the H15 modified (see text for explanation) and H15 models, respectively. Centrals (solid) and satellites (dash-dot) are shown separately.

In this section, we incorporate the information provided by the LBE measurements into our new RPS model implemented in the L-GALAXIES code (§3.2). We compare our model with (i) the fiducial H15 result, and (ii) a modified version of H15 (hereafter 'H15 Mod'). In H15, the RPS for hot gas is limited to satellites within R_{200} of haloes more massive than $2 \times 10^{14} M_\odot/h$. In H15 Mod, we remove this halo mass limit and apply the H15 RPS prescription to all satellites within R_{200}, regardless of host mass.

We report results for all galaxies with stellar mass above $3 \times 10^9 M_\odot/h$ at $z = 0$, as the properties of galaxies at redshift zero are influenced by the physical processes they have experienced through their history. This allows us to assess the integrated influence of our new RPS model.

3.5.1   Amount and impact of hot gas stripping

Stellar and hot gas mass functions

Among all of the physical quantities predicted by the semi-analytic model, stellar mass is one of the least affected by our changes to RPS. This allows us to report changes to all other quantities as a function of stellar mass. In contrast, the hot gas mass function significantly changes in our model, especially for satellite galaxies. Fig. 3.11 illustrates the stellar (left) and hot gas (right) mass functions at $z = 0$. Solid lines denote central galaxies and dash-dotted lines correspond to satellites.

It can be seen that the stellar mass function in our new model (orange lines) has changed only slightly. The effect is strongest for the least massive galaxies, which are more strongly influenced by RPS. At high mass, beyond the knee at $M_\star \simeq 10^{10.5} M_\odot$, there is no appreciable change to the stellar masses of the overall galaxy population with respect to H15 (blue lines) or H15 Mod (green lines). As the SMF is already tightly constrained

in H15 by observational measurements, it is reassuring that it is not modified by our new RPS treatment.

The right panel of Fig. 3.11 shows the hot gas mass functions for these three models. In contrast to $M_\star$, we observe significant changes across almost the entire range of total hot gas masses. There are now a noticeable fraction of central galaxies with low hot-gas mass, $\log(M_{\mathrm{hotgas}}[\mathrm{M}_\odot/\mathrm{h}]) \lesssim 9.0$. Stripping in these central galaxies is primarily driven by rapid movement with respect to their LBE. Without RPS, they appear in the $\log(M_{\mathrm{hotgas}}[\mathrm{M}_\odot/\mathrm{h}]) \gtrsim 10$ portion of the distribution. The difference at the peak of the mass function between the three models demonstrates that this is a small effect by number. For satellite galaxies, on the other hand, this effect is much more significant. Looking at the peak of the hot gas distribution in the right panel of Fig. 3.11, the value in our new model is about 0.4 dex smaller than in previous models. In general, we find that the hot gas mass function in our new model is usually below those of H15 and H15 Mod in the mass range $\log(M_{\mathrm{hotgas}}[\mathrm{M}_\odot/\mathrm{h}]) \gtrsim 8$ for satellite galaxies.

Total stripped hot gas mass

We assess the direct impact of the new model by looking at the total hot gas mass that a galaxy has lost due to stripping processes through the whole history of its main progenitor branch. We define the total stripped hot gas fraction as

$$f_{\mathrm{StrippedHot}} = M_{\mathrm{StrippedHot}} / \left(f_{\mathrm{b}} \, M_{200,\mathrm{max}} \right), \tag{3.19}$$

where f_{b} is the cosmic baryon fraction and $M_{200,\mathrm{max}}$ is the maximum value of M_{200} throughout the history of the subhalo. $M_{\mathrm{StrippedHot}}$ is total stripped hot gas mass:

$$M_{\mathrm{StrippedHot}} = \sum_{z_{\mathrm{i}}}^{N_{\mathrm{snap}}} m_{\mathrm{strippedhot}}(z_{\mathrm{i}}), \tag{3.20}$$

where N_{snap} is the number of simulation snapshots and $m_{\mathrm{strippedhot}}(z_{\mathrm{i}})$ is the sum of the mass stripped from the hot reservoir and the ejected reservoir at $z = z_i$. We track and record this quantity in the L-GALAXIES code, and not simply in post processing.

We analyze the total stripped hot gas fraction of galaxies, stacking systems around central host haloes out to a distance of $R = 5R_{200}$. Fig. 3.12 shows the median value of $f_{\mathrm{StrippedHot}}$ as a function of distance. Each panel corresponds to a different host FOF mass range. The results are shown in three different stellar mass ranges: $9.5 < \log(M_\star[\mathrm{M}_\odot/\mathrm{h}]) < 10.5$ (solid lines), $10.5 < \log(M_\star[\mathrm{M}_\odot/\mathrm{h}]) < 11$ (dashed lines), and $\log(M_\star[\mathrm{M}_\odot/\mathrm{h}]) > 11$ (dotted lines). The modified H15 model (green) and the original H15 model (blue) results are shown for comparison with our new model results (orange).

In general, our model predicts more stripping than both the H15 and H15 Mod models. The difference is small for galaxies within R_{200} and becomes significant for galaxies at larger distances. For scales where $R \gtrsim 2.5R_{200}$, more than half of the galaxies in H15 and H15 Mod have experienced no stripping. On the other hand, our model predicts stripping for galaxies to much larger scales. It can be seen that low-mass galaxies are
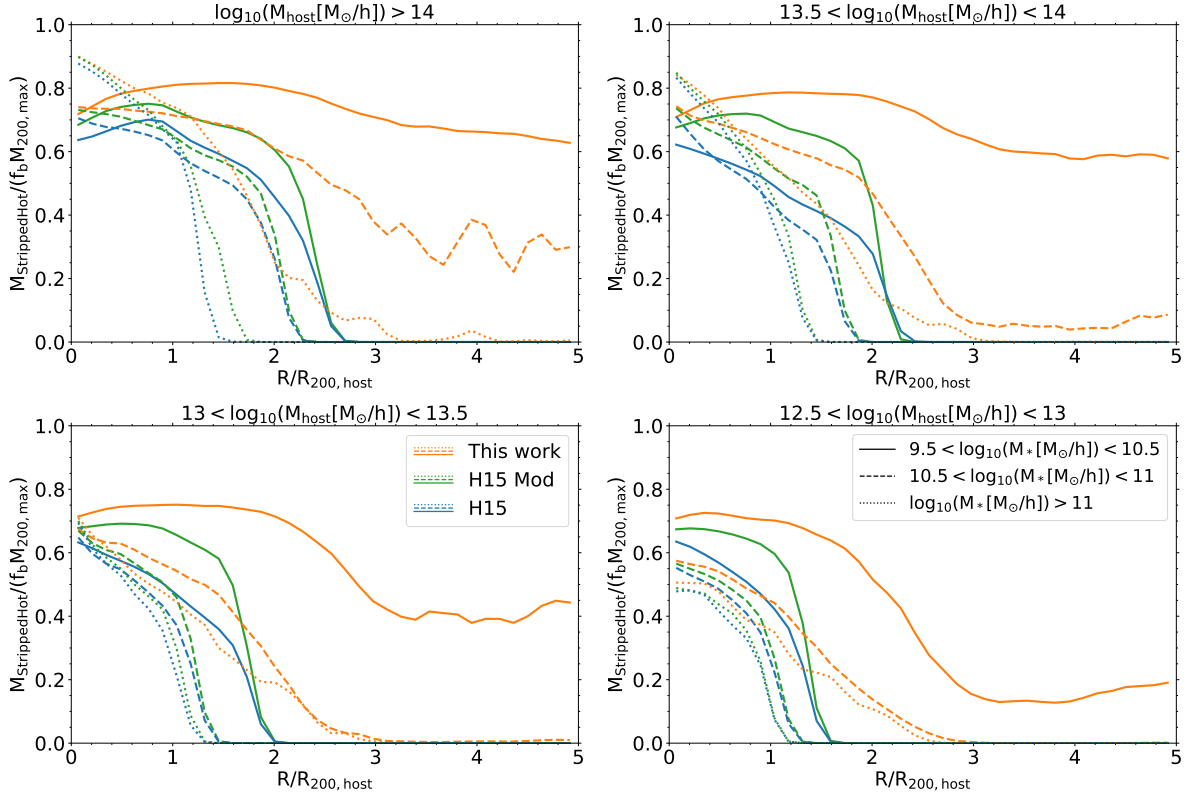
Figure 3.12: Median stripped hot gas fraction of galaxies as a function of their distance from the centre of the host halo. The total stripped hot gas fraction is defined as $f_{\mathrm{StrippedHot}} = M_{\mathrm{StrippedHot}}/(f_{\mathrm{b}}M_{200,\mathrm{max}})$, where f_{b} is the cosmic baryon fraction and $M_{200,\mathrm{max}}$ is the maximum past M_{200}. $M_{\mathrm{StrippedHot}}$ is the sum of stripped hot gas mass over all time-steps for the main progenitor of the galaxy. Different panels show results for different central host halo masses. In all of the panels, we include our new model (orange), H15 (blue), and H15 Mod (green). Different line styles correspond to different stellar mass ranges: solid lines are for galaxies with $9.5 < \log(M_{\star}[\mathrm{M}_{\odot}/\mathrm{h}]) < 10.5$, dashed lines for $10.5 < \log(M_{\star}[\mathrm{M}_{\odot}/\mathrm{h}]) < 11$, and dotted lines for $\log(M_{\star}[\mathrm{M}_{\odot}/\mathrm{h}]) > 11$.

non-trivially affected everywhere. This stripping is a combination of satellites interacting with the medium of their host haloes (so-called 'pre-processing' in galaxy groups), as well as central galaxies interacting with the large-scale matter distribution of cosmic structures, e.g. sheets and filaments.

We also see that galaxies in the vicinity of more massive FOF haloes lose a larger fraction of their hot gas mass due to stripping. Comparing different panels, we conclude that more massive FOF haloes have influence on subhaloes out to larger distances – the total stripped mass fraction decreases from the top left panel (most massive clusters) to the bottom right panel (least massive groups). As more massive haloes are found in denser environments, the increased stripping at $R/R_{200} > 2$ is likely due to ram pressure in neighboring dense haloes. Stripping is in general stronger for galaxies with lower stellar mass due to their weaker gravity, implying that more massive galaxies better retain their hot haloes. Similar trends have been previously found, although they have not been shown to extend smoothly to such large radius (e.g. McCarthy et al. 2008; Bekki 2009; Guo et al. 2011; Henriques et al. 2015; Cora et al. 2018; Stevens et al. 2019)

Interestingly, some stripping is seen for H15 and H15 Mod beyond R_{200}, even though tidal and ram-pressure stripping is not applied beyond R_{200} in those models. The main cause of this phenomenon is splashback galaxies which have previously experienced stripping phases when they were inside R_{200}, but have since passed outside this radius. The sharp drop in the stripping fraction of H15 and H15 Mod in Fig. 3.12, is related to the splashback radius, but is not necessarily equivalent to it, because we show here the integrated stripped mass through the galaxy's entire history. We note that many of the galaxies we consider as galaxies in the vicinity of a FOF halo could have been part of other FOF haloes in the past.

Hot gas fractions

We next consider the hot gas fraction – the ratio of hot halo gas mass to galaxy stellar mass – in Fig. 3.13. As before, we stack galaxies in the vicinity of FOF haloes as a function of distance. Comparing the different models, we see that our model generically predicts a smaller hot gas to stellar mass ratio. Hot gas fractions can be suppressed by an order of magnitude or more for low mass galaxies around massive hosts. This result is a consequence of the dependence of the stripped hot gas fraction on host halo mass and stellar mass discussed in §3.5.1. The difference between our model and H15 (or H15 Mod) is smaller for galaxies in the vicinity of low mass FOF haloes (bottom right panel) and gets larger with host FOF mass – gas stripping is stronger near more massive haloes. Furthermore, the hot gas to stellar mass ratio changes more for galaxies with low stellar masses (solid lines) because of the weak gravitational binding energy of these systems. For galaxies with high stellar mass (dotted lines), our model approaches the previous results of the H15 and H15 Mod models. The hot gas contents of high-mass haloes ($\gtrsim 10^{13} M_\odot$) are observationally well constrained by existing X-ray measurements (e.g. Anderson et al. 2015), so it is again a useful sanity check that we have not significantly changed the results of L-GALAXIES in this regime. Upcoming instruments and joint Sunyaev-Zeldovich analyses will offer tight
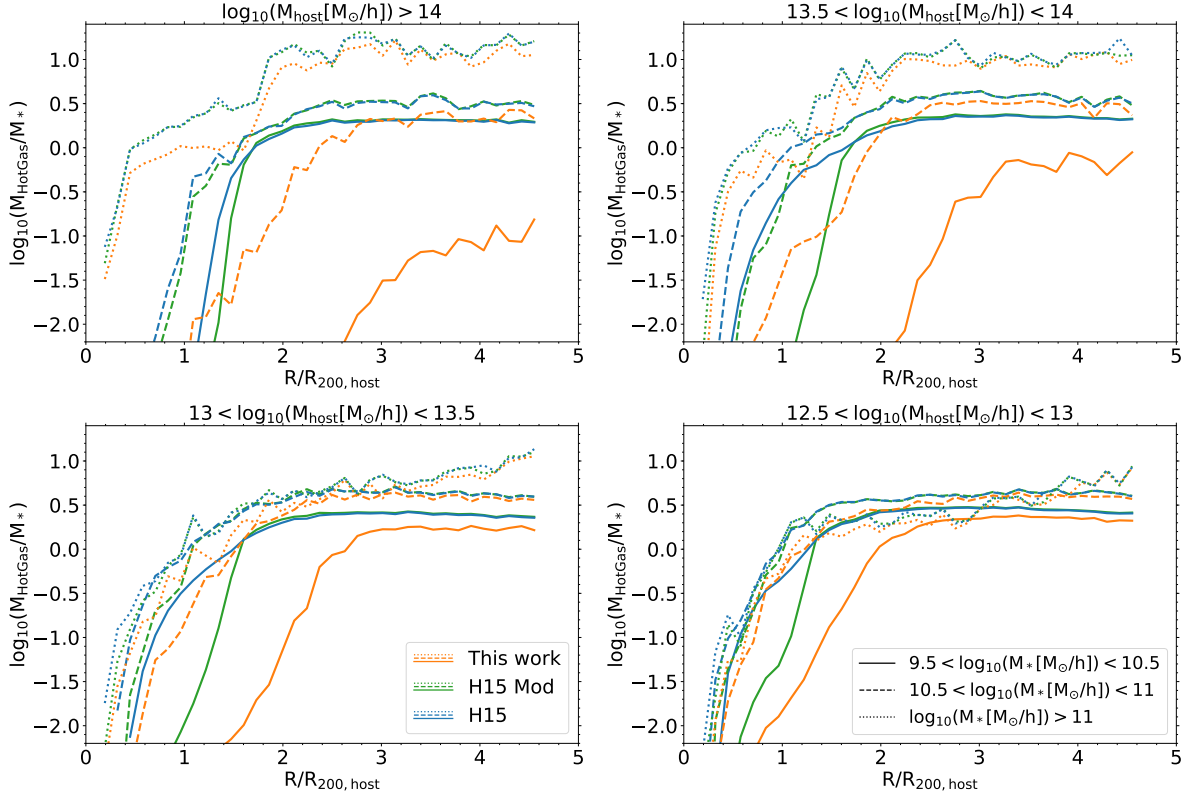
Figure 3.13: Median value of hot gas to stellar mass ratio as a function of distance to the central host haloes. Different panels show different central host masses. In all of the panels, orange lines are the results of this work, with stripping extended to all of the galaxies in the simulation, regardless of type, position, or host mass. Blue lines are the results of H15 and green lines are the H15 modified. Different line styles correspond to different stellar mass ranges, where solid lines are for the galaxies with $9.5 < \log_{10}(M_*[M_\odot/h]) < 10.5$, dashed line show the ones with $10.5 < \log_{10}(M_*[M_\odot/h]) < 11$, and dotted lines illustrate galaxies with $\log_{10}(M_*[M_\odot/h]) > 11$.

constraints on the hot gas contents down to even lower mass scales (Lim et al. 2018; Singh et al. 2018).

In all the three models, the hot gas to stellar mass ratio first increases with distance from the centre of the FOF and then flattens. For H15 and H15 Mod, this scale is around $1.5R_{200}$, which is close to the splashback radius. On the other hand, in our model, the hot gas to stellar mass ratio flattens at a scale larger than $1.5R_{200}$ and there is no clear sign of the splashback radius. We recall that our estimation of local background density – and so RPS – tracks the underlying dark matter distribution and so returns continuous values as function of distance away from any host. At the same time, it captures non-spherical effects such as higher overdensities in certain directions due to the filamentary infall of satellites, a topic we will study more in the future.
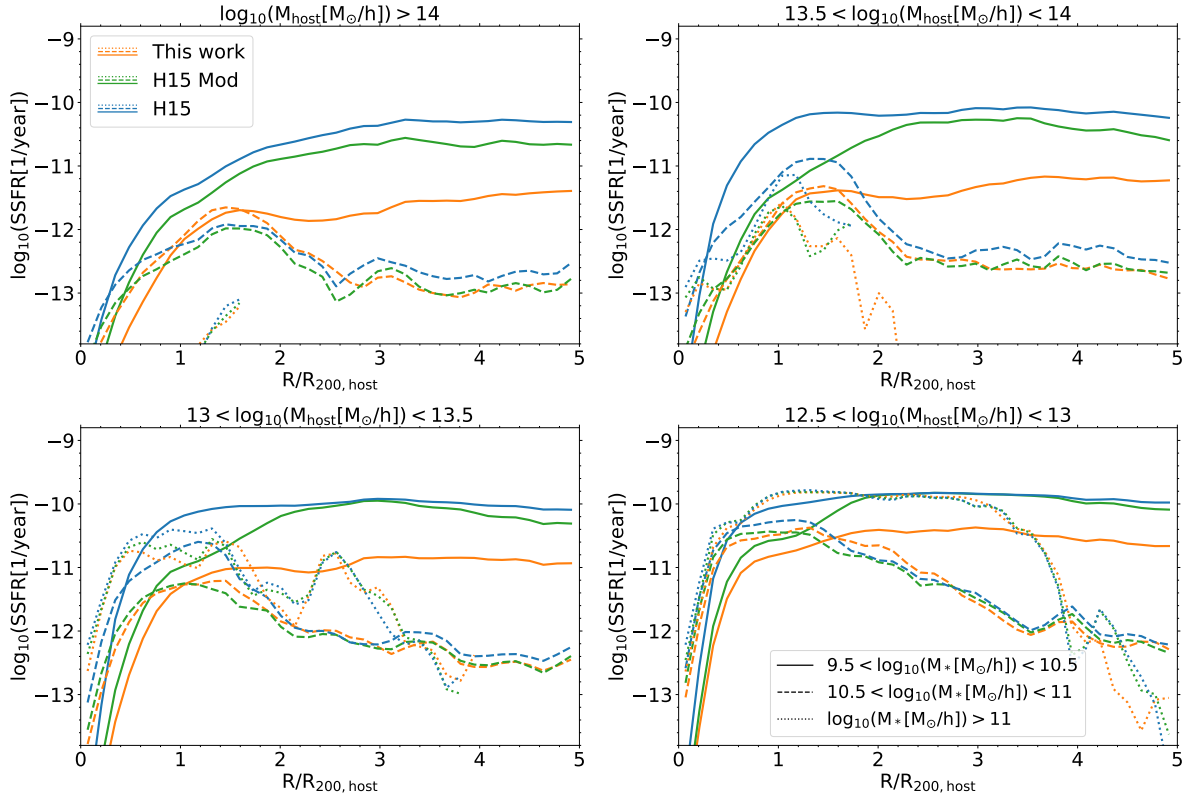
Figure 3.14: Median value of the specific star formation rate (sSFR) of galaxies as a function of their distance from massive haloes. Different panels show different central host masses. In all of the panels, orange lines are the results of this work, with stripping applied to all of the galaxies in the simulation, regardless of type, position, or host mass. Blue lines are the results of H15 and green lines are for the H15 modified models. Different line styles correspond to different stellar mass ranges, where solid lines are for the galaxies with $9.5 < \log(M_\star[\mathrm{M_\odot/h}]) < 10.5$, dashed lines are for $10.5 < \log(M_\star[\mathrm{M_\odot/h}]) < 11$, and dotted lines illustrate galaxies with $\log(M_\star[\mathrm{M_\odot/h}]) > 11$.

Specific star formation rates

Stripping of the hot gas changes the cooling rates and the masses of cold star-forming gas in galaxies and consequently, their star formation rates. Our model generically produces lower specific star formation rates for most galaxies, as shown in Fig. 3.14. Here we derive the median specific star formation rate (sSFR) of galaxies as a function of distance, as before. The colours and line styles are the same as in Figs. 3.12 and 3.13. Our model (orange) reduces the sSFR for galaxies with low stellar mass (solid lines) significantly. On the other hand, the predicted values of sSFR for galaxies with $\log(M_\star[\mathrm{M_\odot/h}]) \gtrsim 10.5$ are not notably different from H15 or H15 Mod (dashed and dotted lines). As already seen in the hot gas fractions, low mass galaxies experience the most stripping, and the ram-pressure force at large distances is not strong enough to cause significant gas stripping in
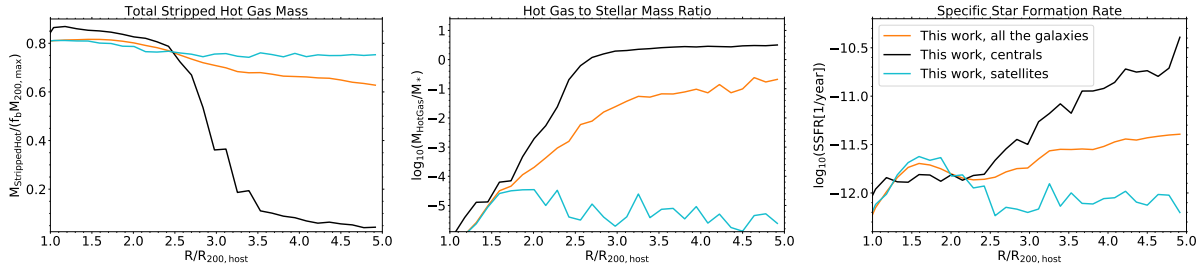
Figure 3.15: Total stripped hot gas mass (left), hot gas to stellar mass ratio (middle), and specific star formation rate (right) of galaxies as a function of distance from a central massive halo. This figure contrasts results for central and satellite galaxies beyond R_{200} in our model. Orange shows the median values for all the galaxies, while black and cyan show values separately for central and satellite galaxies. All the galaxies are located around FOF haloes with $M_{200,\mathrm{host}} > 10^{14} \mathrm{M_\odot}/\mathrm{h}$ and have stellar masses of $9.5 < \log(\mathrm{M_\star[M_\odot/h]}) < 10.5$.

more massive subhaloes.

In contrast to hot gas contents, the star formation activity of galaxies is well studied and constrained across a wide range of mass, redshift, and environment (Kauffmann et al. 2004; Peng et al. 2010; Wetzel et al. 2012). The tight star formation main sequence (Noeske et al. 2007) and its dependence on these properties provides strong constraints on simulations (Wang et al. 2014; Donnari et al. 2019). The colour distributions and relative fractions of red versus blue galaxies, including radial member colour profiles inside groups and clusters, are similarly useful benchmarks (Sales et al. 2015; Trayford et al. 2016; Nelson et al. 2018). It is clear that, in certain regimes, the sSFR changes incurred by our new RPS model updates may exceed the room allowed by current constraints. This is not surprising, as the current calibration of the L-Galaxies parameter set is based on the previous model H15. In the future, to make robust and realistic connections to observations, we will need to recalibrate the new model with our stripping changes.

Central versus satellite galaxy properties

Although our RPS implementation does not explicitly distinguish between central and satellite galaxies, we find as an outcome that satellites are much more influenced by RPS than centrals. At large distances from the centers of massive haloes ($R/R_{200,\mathrm{host}} \gtrsim 2.5$), satellites are more strongly stripped on average. This is because, by virtue of being a satellite, they typically exist in a more crowded environment. They consequently have lower hot gas to stellar mass ratios and specific star formation rates than centrals, at fixed mass.

To clearly diagnose the role of stripping for centrals versus satellites, Fig. 3.15 shows again the total stripped hot gas fraction (left), hot gas to stellar mass ratio (middle), and sSFR (right) for satellites and centrals separately. We focus on the most massive host halo bin, $M_{200,\mathrm{host}} > 10^{14} \mathrm{M_\odot}/\mathrm{h}$ (top left panels of Figs. 3.12 through 3.14) and concentrate on the outer regions of haloes, beyond R_{200}. We decompose the median for all galaxies

(orange) into centrals (black) and satellites (cyan) separately.

As can be seen in the left panel, at large radii, satellite galaxies have lost a significant fraction of their hot gas due to stripping, while central galaxies have lost only a small fraction. Specifically, satellites have a stripped fraction above 75% regardless of distance, while this fraction drops rapidly to zero for centrals beyond $\sim 3R_{200}$. This constancy for satellite systems highlights the important role of environmental effects associated to host haloes other than the central one around which we stack.

The middle panel of Fig. 3.15 makes it clear that, at large radii and for galaxies with $10^{9.5} < M_\star/(\mathrm{M}_\odot/\mathrm{h}) < 10^{10.5}$, the hot gas to stellar mass ratio of central galaxies is much higher than in satellites, exceeding unity in general. In our fiducial model, satellites at these stellar masses have lost the vast majority of their hot haloes, and have negligible hot gas fractions. Once centrals start to experience similarly harsh environments ($R/R_{200} \lesssim 2$) they become equally depleted of their hot gaseous reservoirs. Galaxies, regardless of type or history, usually cannot retain a large fraction of their hot halo gas once they approach such massive hosts.

The right panel of Fig. 3.15 shows that central galaxies have higher specific star formation rates at large radii compared to satellites. This differential effect can exceed 1 dex in sSFR, although an equal level of quiescence is reached by the time galaxies approach $R/R_{200} \simeq 2.5$ (i.e. ~ 3 Mpc) from the FOF halo, demonstrating the importance of large-scale environmental effects far beyond the virial radii of massive haloes.

3.6 Summary and Discussion

In this chapter, we have introduced a new technique to capture environmental effects, in particular, ram-pressure stripping (RPS), within semi-analytical models of galaxy formation. To do so we have introduced the concept of the local background environment (LBE). The LBE is extracted directly from the particle-level data of the high resolution N-body cosmological simulation of structure formation on which L-Galaxies is run, using a local, adaptive, spherical shell. We design a Gaussian mixture estimator to separate true background particles from subhalo contaminants in velocity space, overcoming classical difficulties of substructure finders in dense environments.

We first measure the statistical properties of the local background environment of all subhaloes in the Millennium Simulation, analyzing its properties at $z = 0$. We find that:

- Neither the LBE density (ρ_{LBE}) nor the galaxy's velocity relative to its LBE ($\vec{v}_{\mathrm{gal,LBE}}$) show a strong dependence on subhalo mass. The LBE density of satellite galaxies does not vary significantly with host halo mass, but the velocity of satellite galaxies relative to their LBE strongly increases with host mass. Central galaxies move faster relative to their LBE with increasing mass. The velocity of a galaxy relative to its environment, $\vec{v}_{\mathrm{gal,LBE}}$, declines slowly with increasing distance away from massive hosts.

- Both ρ_{LBE} and $v_{\text{gal,LBE}}$ vary continuously and weakly across the virial radius of the host halo. Neither exhibit discontinuous behavior out to $5R_{200}$, implying that ram-pressure stripping extends (and can be non-negligible) beyond the virial radius.

- At large distances from massive haloes, the LBE of galaxies moves on average in the same direction as the galaxy itself, although typically somewhat slower, a signature of coherent infall. The angle between $\vec{v}_{\text{gal}}$ and $\vec{v}_{\text{LBE}}$ becomes more uniform towards halo centers as orbits isotropize. The LBE of satellite galaxies is generically *not* at rest with respect to the host halo, in contrast to common assumptions.

Using our LBE methodology we then devise a new treatment of RPS of hot halo gas within the Munich semi-analytical model L-Galaxies. Applied to the Millennium simulation, our principal results are:

- Compared to the publicly released version of L-Galaxies (Henriques et al. 2015) our model results in significantly more hot gas stripping. While the stellar mass function remains unchanged, the hot gas fractions and specific star formation rates are strongly suppressed, depending on satellite mass, host mass, and distance.

- Galaxies with the lowest stellar masses are the most affected by stripping due to their weaker self gravity. Satellites in massive clusters ($M_{\text{host}} > 10^{14}\text{M}_\odot$) with $M_\star < 10^{10.5}M_\odot$ can lose the majority of their hot gas mass relative to the fiducial model, while for $M_\star > 10^{11}M_\odot$ the impact is subtle.

- Our LBE estimates imply that galaxies near and inside group-mass haloes ($< 10^{14}\text{M}_\odot$) also undergo sufficient RPS to impact their hot gas contents and so star formation rates, despite lower background densities and relative velocities.

- Satellites at large distances ($> 2R_{200}$) experience much stronger RPS effects than centrals at the same mass, indicative of environmental pre-processing.

In this chapter we have not yet compared the new model outcomes with observational data. This will require a recalibration of the free parameters in L-Galaxies (as in Henriques et al. 2015), which we undertake in Chapter 4. Several assumptions of our treatment for stripping, such as the mapping between the dark matter and gas matter density fields, will also benefit from comparisons with hydrodynamical simulations (Nelson et al. 2019b) which we plan to undertake in the future as well. Overall, our results demonstrate the importance of a ram-pressure stripping model which incorporates local (and *continuous*) estimates of background properties without artificial boundaries in space or halo mass.

Chapter 4

The role of environment in galaxy evolution

4.1 Introduction

In Chapter 3, we devised a new method to measure, locally and accurately, ram-pressure for all galaxies in the L-GALAXIES semi-analytical model using the particle data of the underlying dark matter only (DMO) simulation. Here, we employ this method and update L-GALAXIES by extending ram-pressure stripping to all simulated galaxies, regardless of their environment. Taking advantage of the computational efficiency of L-GALAXIES, one can quickly implement and test new ideas and theories in galaxy formation and evolution, as is done in this work. Here we probe the role of environment in galaxy evolution by investigating the idea of galaxies becoming ram-pressure stripped *prior to* and after infall into massive and intermediate-mass haloes. To do so, we calibrate our updated L-GALAXIES model against a set of observational constraints using a full MCMC approach. We then measure the actual amount of the stripped gas for every galaxy on the fly as the SAM is run. We finally contrast our model predictions with a number of other observations, specifically focusing on the role of environment, and explore the impact of our new stripping model on galaxy properties and the galaxy population as a whole.

This chapter is structured as follows: In §4.2 we introduce a variant of the L-GALAXIES model with a novel hot gas stripping method. The observations used in this work and the mock catalogues we make to compare our model with those observations are described in §4.3. Section 4.4 is dedicated to studying the environmental dependency of galaxy evolution in our model, comparing both with previous versions and with observations. Finally, we conclude and summarise our results in §4.5.

4.2   New model updates

4.2.1   Hot gas stripping

Haloes accrete hot gas (and dark matter), a process known as cosmic infall. In L-GALAXIES, the amount of this gas is set to be proportional to the amount of infalling dark matter. The hot gas radius, R_{hotgas}, of every central subhalo is set equal to the virial radius (R_{200}) of its host halo. Satellite subhaloes are assumed to have no gas infall, and their hot gas radius is determined based both on their hot gas radius at infall time and on the environmental effects they experience.

  If a subhalo moves fast enough in a dense environment, it can lose gas due to stripping processes such as tidal and ram-pressure stripping. In the H20 version of L-GALAXIES, these processes only occur to satellites within the halo R_{200} (tidal stripping) and only in satellites within R_{200} of massive clusters with $\log_{10}\left(M_{200}/\mathrm{M_\odot}\right) > 14.7$ (ram-pressure stripping). We follow the method we introduced in Chapter 3 to calculate ram-pressure stripping more self-consistently, removing these artificial boundaries in position and halo mass. We extend stripping processes so that they happen to all galaxies, regardless of whether they are a central or satellite.

  Our treatment of ram-pressure and tidal stripping is fully explained in §3.2. In this section, we explain our implementation of hot gas stripping in the new L-GALAXIES model [1]. The changes are also summarised in Table 4.1.

Stripping implementation and the fate of the stripped gas

Satellite galaxies are subject to both tidal and ram-pressure stripping. Therefore, we take the stripping radius to be the smaller of the tidal stripping radius and the ram-pressure stripping radius. For central galaxies, the stripping radius is equal to the ram-pressure stripping radius, as we do not consider them subject to tidal stripping. After stripping, we assume the density profile of the remaining gas remains isothermal with $\rho \propto r^{-2}$. We note that ram-pressure stripping is the dominant effect for most galaxies.

  In addition to hot gas stripping we also strip the ejected reservoirs of galaxies. The fraction of gas stripped from the ejected reservoir of a galaxy is assumed to be the same as the fraction of its stripped hot gas. Stripping of material that has been expelled from the galaxy by feedback processes and is assumed to lie at least temporarily in this ejecta reservoir plays a critical role in the evolution of galaxies (see §4.4.1).

  For every galaxy, if $R_{\mathrm{strip}} < R_{\mathrm{hotgas}}$, all the gas beyond R_{strip} is removed. For satellite galaxies within the halo boundary, R_{200}, the stripped gas goes directly to the hot gas component of their host halo. For central galaxies and satellites beyond the halo R_{200}, the stripped gas does not go to any halo immediately, but we keep track of it through time. If the galaxy subsequently falls into R_{200} of a halo, then the stripped gas is added to the host halo's hot gas with the condition that the host halo's baryon fraction does not exceed the

---

[1]We have made the full output of our updated L-GALAXIES model for all the Millennium and Millennium-II snapshots publicly available at lgalaxiespublicrelease.github.io.

Table 4.1: Summary of model updates regarding gas stripping as described in §4.2.

| Ram-pressure stripping		
Model	**H20**	**This work**
Formula	Eq. 3.6	Eq. 3.6
Implemented for	Satellite subhaloes within R_{200} of massive clusters	All satellite and central galaxies
$\rho_{\mathrm{LBE,hotgas}}$ (Local density)	Isothermal $\rho \propto r^{-2}$	Local density from the particle data
$v_{\mathrm{gal,LBE}}$ (galaxy's velocity relative to its environment)	Virial velocity of the satellite's host halo	The velocity of galaxy relative to its LBE
R_{g} (known radius to estimate gravity)	Satellites: R_{200} at infall time Centrals: N/A	Satellites: Half mass radius Centrals: R_{200}
M_{g} (known mass to estimate gravity)	Satellites: M_{200} at infall time Centrals: N/A	Satellites: Mass within R_{halfmass} Centrals: M_{200}
Tidal Stripping		
Formula	Eq. 3.8	Eq. 3.8
Implemented for	Satellite galaxies within R_{200} of haloes	All FOF satellite galaxies
The stripping radius and the fate of the stripped gas		
Satellite within R_{200}	same as this work	- $R_{\mathrm{strip}} = \min(R_{\mathrm{rp}}, R_{\mathrm{tidal}})$ - The stripped gas is added to the hot gas of its host - After stripping: $R_{\mathrm{hotgas}} = \min(R_{\mathrm{hotgas,old}}, R_{\mathrm{strip}})$
Satellite beyond R_{200}	N/A	- $R_{\mathrm{strip}} = \min(R_{\mathrm{rp}}, R_{\mathrm{tidal}})$ - The stripped gas stays outside its host halo and is allowed to fall inside R_{200} if the galaxy itself falls inside R_{200} of its host - After stripping: $R_{\mathrm{hotgas}} = \min(R_{\mathrm{hotgas,old}}, R_{\mathrm{strip}})$
Central galaxy	N/A	- $R_{\mathrm{strip}} = R_{\mathrm{rp}}$ - If the galaxy falls into R_{200} of a halo later, the stripped gas is also allowed to fall into that halo. - After stripping: $R_{\mathrm{hotgas}} = R_{200}$
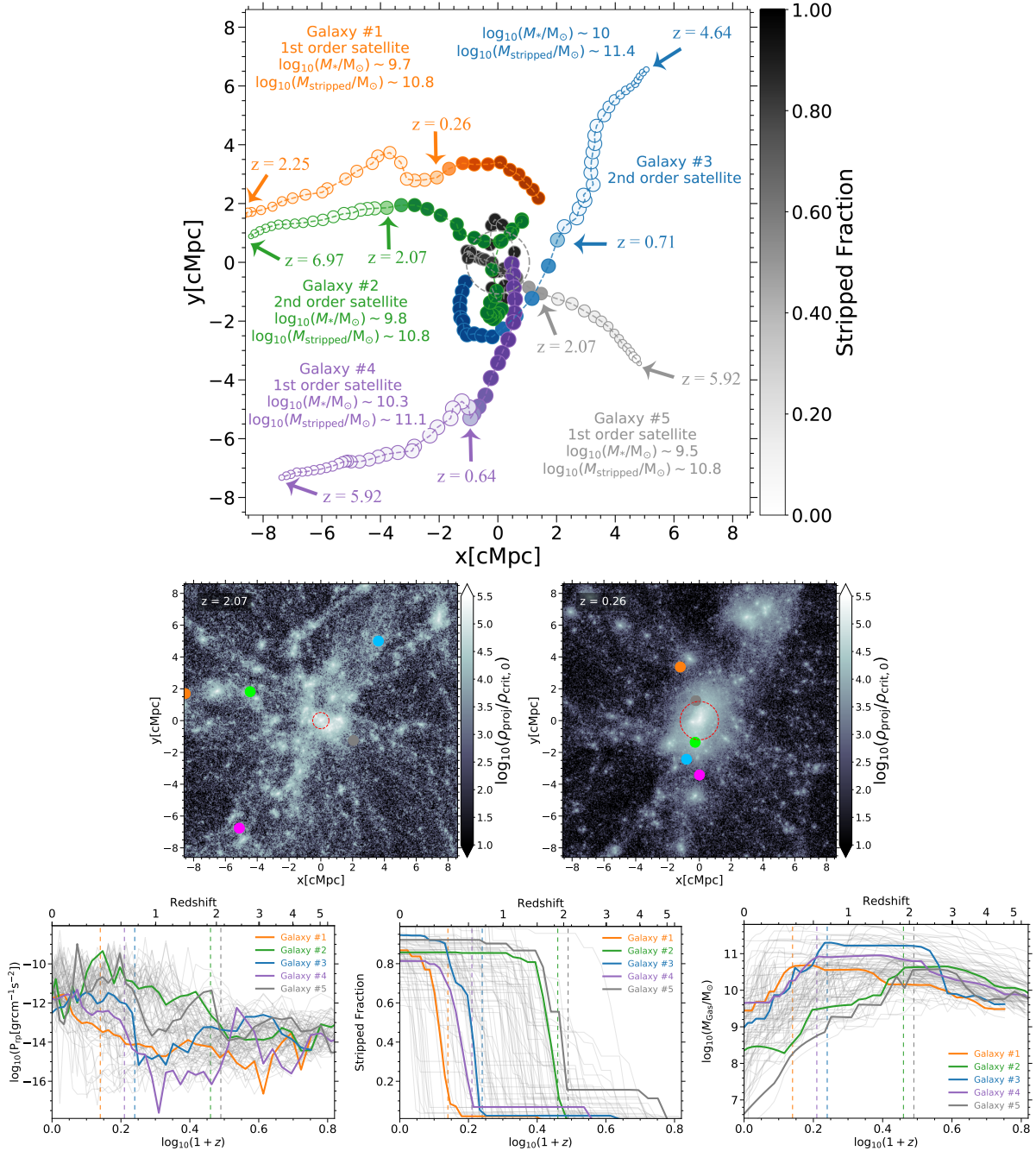
Figure 4.1: Illustration of gas stripping in our model. Top panel: Five sample galaxies in the vicinity of a massive cluster with $\log_{10}(M_{200}/M_\odot) \sim 14.5$. Each colour corresponds to a galaxy, and different circles of the same colour demonstrate the evolution of that galaxy at different redshifts. The size of each circle represents, qualitatively, the galaxy's stellar mass. Shown by the colourbar, the transparency of colours denotes the fraction of the gas stripped (Eq. 4.1). The stellar mass and total stripped mass of each galaxy are quoted at $z = 0$. Middle panel: Matter distribution, depicting the positions of the five galaxies in the cosmic web. All coordinate units are comoving. Bottom panel: ram-pressure (left), stripped fraction (middle) and gas mass (right) versus redshift. Each curve corresponds to a galaxy that is currently a satellite of the central cluster. The dashed vertical lines correspond to the redshift where our five chosen galaxies start getting stripped significantly.

cosmic value. After stripping, the new hot gas radius of a satellite will be the minimum of its former hot gas radius and R_{strip}. On the other hand, as long as a galaxy is categorised as a central galaxy, since it accretes hot gas from its environment, its hot gas radius is set to its FOF R_{200}.

Tracking gas stripping

We measure the amount of gas lost due to stripping in different conditions and separate it from other intrinsic physical processes. In order to evaluate the impact and predictions of our method quantitatively, we define the "cumulative stripped fraction", or simply the "stripped fraction" of a subhalo at a given redshift as

$$f_{\text{stripped}}(z) = M_{\text{stripped}}(z) / (f_{\text{b}} \, M_{200,\text{max}}) \,, \tag{4.1}$$

where $M_{200,\text{max}}$ is the maximum M_{200} of the main progenitor of the subhalo through time. $M_{\text{stripped}}(z)$ is the total mass which has been stripped from the subhalo since its formation time until redshift z. This includes gas stripped from the hot gas component and the ejected reservoir including material stripped while the subhalo was a central, unless we explicitly decompose the two. This is a cumulative quantity that we track for every galaxy across time.

As an overview of our new model, Fig. 4.1 illustrates a rather massive cluster with $\log_{10}(M_{200}/\text{M}_\odot) \sim 14.5$ and five galaxies that end up as its satellites by $z = 0$. Each galaxy is shown by one colour, and in the top panel, the transparency of that colour shows the cumulative stripped fraction of the galaxy (Eq. 4.1) at each simulation snapshot. The formation redshifts, and the redshifts at which each galaxy starts to be significantly stripped, are indicated by arrows. It is clear that stripping processes start long before galaxies fall within the virial radius (R_{200}) of their present-day halo (dashed circle at the centre). We find that, on average, a satellite galaxy loses more than 70-80% of its hot gas due to stripping prior to its infall (see §4.4.1). Galaxy #2 (green) and #3 (blue) are pre-infall satellites, i.e. they are already satellites of other haloes at $z > 0$, prior to their infall into the central cluster. These two galaxies have lost a considerable fraction of their hot gas through pre-processing in their initial hosts.

On the other hand, the three other galaxies (#1, #4 and #5) are categorised as central galaxies until they fall directly into their $z = 0$ host halo. These galaxies have lost their hot gas via ram-pressure stripping when moving fast through the dense environment beyond the halo boundary of their present-day host halo. The middle panels of Fig. 4.1 show the position of the sample galaxies in the cosmic web at two different redshifts, $z = 2$ and $z = 0.26$. They illustrate the times when the green (#2) and purple (#4) galaxies (left panel) and the orange galaxy (#1) are strongly stripped. For example, galaxy #1 moves through the overdensity around the central host halo, but extending far beyond its virial radius, at which there is no abrupt change in density. All five galaxies pass through dense environments at some time in their history, losing a large fraction of their gas [2]. It

---

[2]A video showing the stripping process for our sample galaxies is given in the supplementary material of Ayromlou et al. (2021b).

is clear that the matter distribution of the proto-cluster is very extended, but there is no significant change in the density of the central region of the halo.

Finally, the bottom panels of Fig. 4.1 depict the ram-pressure (left), the cumulative stripped fraction (middle), and the gas mass (right) of all the cluster's $z = 0$ surviving satellite subhaloes as a function of redshift. The previously highlighted galaxies are illustrated as thick curves, while the rest of the galaxies are shown with thin grey lines. The vertical lines correspond to the redshifts where the five sample galaxies start becoming significantly stripped. There is a strong correlation between high values of ram-pressure and the times when galaxies lose gas. Overall, Fig. 4.1 depicts the importance of modelling stripping beyond the virial radius, showing that galaxies can even lose their entire hot gas reservoir while still centrals, without ever infalling into a more massive host halo.

4.2.2   Gas infall into haloes

The L-Galaxies infall recipe in H20 is that the gas accretion rate onto haloes is equal to the accretion rate of total matter times the cosmic baryon fraction. It is possible that the baryon fraction exceeds the cosmic value (see Fig. 2.8). There are two reasons for this discrepancy, as described by Yates et al. (2017). The first and more dominant effect is due to the implementation of environmental effects such as tidal and ram-pressure stripping. Satellite galaxies in the infall regions lose dark matter due to tidal effects in the DMO simulation on which L-Galaxies is run. The lack of environmental stripping effects for gas beyond R_{200} can give these satellites a baryon fractions greater than the cosmic value when they fall into R_{200} of their host halo. This artificially increases the baryon fraction of their host, given that its infall has already topped-up the halo's baryon budget to the cosmic baryon fraction. In this work we fully resolves this issue by having gas stripping for satellites beyond the halo R_{200} (see §4.2.1).

The second reason is that total halo mass can decrease with time because of changes in morphology or halo concentration or simply through numerical fluctuations (see De Lucia et al. 2004 for subhalo mass fluctuations). At the same time, in L-Galaxies the halo baryonic mass within R_{200} is kept unchanged by construction, causing an increase in the baryon fraction. Following the prescription of Yates et al. (2017) we correct the input halo merger trees to prevent the M_{200} from decreasing with time. This accounts for any artificial decrease in M_{200} measured when determining R_{200} based on the assumption of spherical symmetry for haloes.

4.2.3   Model calibration

Like all galaxy formation models and simulations, L-Galaxies has a number of parameters (e.g. the star formation efficiency) that need to be fit. Therefore, we calibrate our new model against a set of observational constraints using the Markov Chain Monte Carlo (MCMC) approach developed by Henriques et al. (2009) and used by previous L-Galaxies versions (e.g. Guo et al. 2013; Henriques et al. 2020). To speed up the model calibration, the MCMC approach runs the model on a representative set of halo merger trees (see

Table 4.2: Free parameters used in the MCMC model calibration in this work and previous models (Guo et al. 2013; Henriques et al. 2015; Henriques et al. 2020). Those values labelled as "F.P." are fixed parameters, which are not taken from the MCMC best fit.

| Model Parameter	G13	H15	H20	This Work	Units
α_{SF} (Star formation efficiency)	0.011	0.025	0.06	0.073	
$\alpha_{\mathrm{SF,burst}}$ (Star formation burst efficiency)	0.56	0.60	0.50	0.116	
$\beta_{\mathrm{SF,burst}}$ (Star formation slope)	0.70	1.9	0.38	0.674	
k_{AGN} (Radio feedback efficiency)	N/A.	5.3×10^{-3}	2.5×10^{-3}	8.5×10^{-3}	$\mathrm{M}_\odot/\mathrm{yr}$
f_{BH} (Black hole growth efficiency)	0.03	0.041	0.066	0.011	
V_{BH} (Quasar growth scale)	280	750	700	1068	km/s
$\epsilon_{\mathrm{reheat}}$ (Mass-loading efficiency)	4.0	2.6	5.6	9.7	
V_{reheat} (Mass-loading scale)	80	480	110	119	km/s
β_{reheat} (Mass-loading slope)	3.2	0.72	2.9	2.9	
η_{eject} (Supernova ejection efficiency)	0.18	0.62	5.5	9.56	
V_{eject} (Supernova ejection scale)	90	100	220	172	km/s
β_{eject} (Supernova ejection slope)	3.2	0.80	2.0	1.88	
γ_{reinc} (Ejecta reincorporation)	N/A.	3.0×10^{10}	1.2×10^{10}	6.6×10^{9}	1/yr
M_{rp} (Ram-pressure threshold)	0.0	1.2×10^{4}	5.1×10^{4}	N/A	$10^{10}\mathrm{M}_\odot$
R_{merger} (Major-merger threshold)	0.30	0.1 (F.P.)	0.1 (F.P.)	0.1 (F.P.)	
$\alpha_{\mathrm{friction}}$ (Dynamical friction)	2.0	2.5	1.8	0.312	
$f_{\mathrm{z,hot,TypeII}}$	N/A.	N/A.	0.3 (F.P.)	0.3 (F.P.)	
$f_{\mathrm{z,hot,TypeIa}}$	N/A.	N/A.	0.3 (F.P.)	0.3 (F.P.)	
v_{inflow}	N/A.	N/A.	1000 (F.P.)	1000 (F.P.)	km/s/Mpc
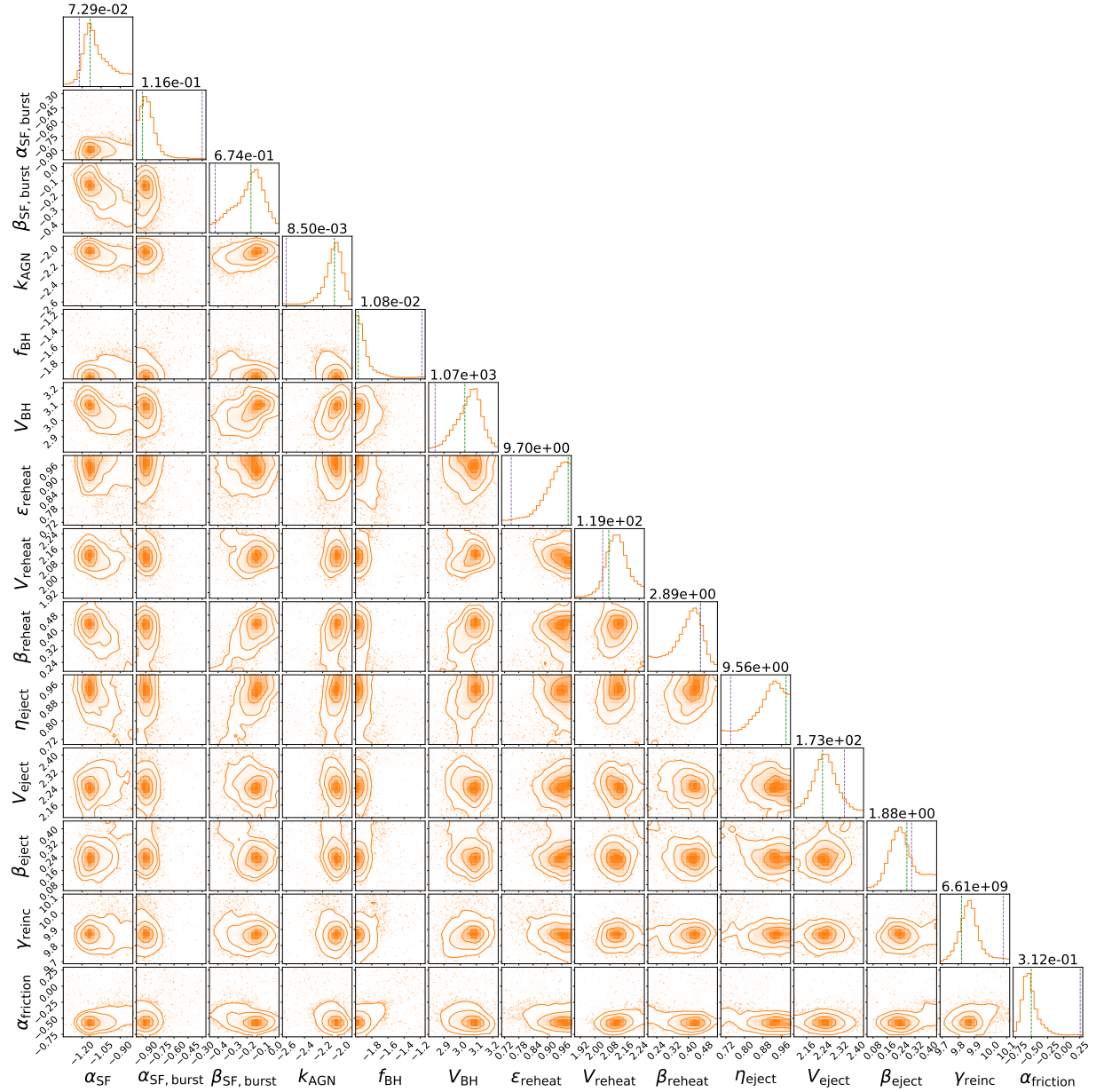
Figure 4.2: Histograms of the weighted accepted MCMC steps (after burn-in) for all the free parameters used in this model. The green dashed lines correspond to our best fit for each parameter and the purple dashed lines are the best fit in H20. The x-axes and y-axes in all panels are reported in logarithmic units. The value above each 1D histograms corresponds to the best fit (in linear units) of that parameter in this work. This figure is generated using ~ 23000 MCMC steps.

Henriques et al. 2013) instead of on the full simulations, a scheme we also adopt. In addition, we extend the previous MCMC method to also incorporate our new treatment of environmental effects.

We use six independent observational constraints: the stellar mass function and the fraction of quenched galaxies, each at $z = 0, 1, 2$. Unlike H20, we do not use the HI gas mass function at $z = 0$ as an observational constraint. However, our final model output for the HI mass function is in relatively good agreement with observations and H20 (bottom left panel of Fig. 4.7). Choosing proper observational constraints and weighting them to converge to an acceptable fit can be a tricky task. For instance, weighting all observational constraint equally, would result in a rather bad fit for the stellar mass function at $z = 0$, especially for galaxies with $10 < \log_{10}(M_\star/M_\odot) < 11$. Ultimately, exploring different weightings for different datasets, we find it best to give the highest weight to the observational constraints at $z = 0$. Furthermore, at $z = 0$ itself, we give the stellar mass function a higher weight than the quenched fraction. To properly fit the $z = 0$ stellar mass function for $M^\star$ galaxies, we give an additional weight to the stellar mass function at $10 < \log_{10}(M_\star/M_\odot) < 11$. At $z > 0$, observational constraints are weighted equally.

We run the MCMC for several tens of thousands of steps, i.e. we execute our model with different free parameters tens of thousands of times. During the calibration, we use L-GALAXIES run on the Millennium simulation for galaxies with $\log_{10}(M_\star/M_\odot) > 9$ and L-GALAXIES run on Millennium-II for lower stellar masses. This stellar mass transition value is chosen following H20 and also by monitoring the approximate stellar mass where the two runs converge for a few smaller runs of the model (see also Guo et al. 2011; Henriques et al. 2020). We note that our model has one fewer free parameter than H20, as we no longer limit ram-pressure stripping to satellites of massive clusters. Table 4.2 compares our best fit parameters to previous models. The relevant equation for each free parameter is also given in that table. The description of most of the equations can be found in Chapter 1 and also the supplementary material of Ayromlou et al. (2021b). In addition, histograms of the PDFs of accepted MCMC steps for all free parameters are shown in a corner plot in Fig. 4.2. 2D contour plots show the marginalised (and normalised) 2D posterior distributions for all the possible free parameter pairs of our model. Furthermore, 1D histograms depict the individual constraints on each parameter. The vertical dashed lines show the best fit from our model (green) and from H20 (purple), and the value quoted indicates the best fit value (in linear units).

Our best fits to the observational constraints are shown in Fig. 4.3 in comparison with observations and the H20 model. The top panels of Fig. 4.3 show that our fits (orange lines) to the stellar mass functions at different redshifts are slightly better than H20, in particular for low-mass galaxies. In addition, the bottom panels show that we have a higher fraction of massive quenched galaxies at higher redshifts, in better agreement with observational data. This is primarily due to the higher AGN feedback efficiency parameter (see Table 4.2). Overall, our model fits the targeted observational constraints successfully.

We emphasise that we *do not* include any environment-dependent quantities in the observational constraints used in our model calibration. As a result, we retain all environmental dependencies and correlations related to galaxy evolution as *predictions*, rather
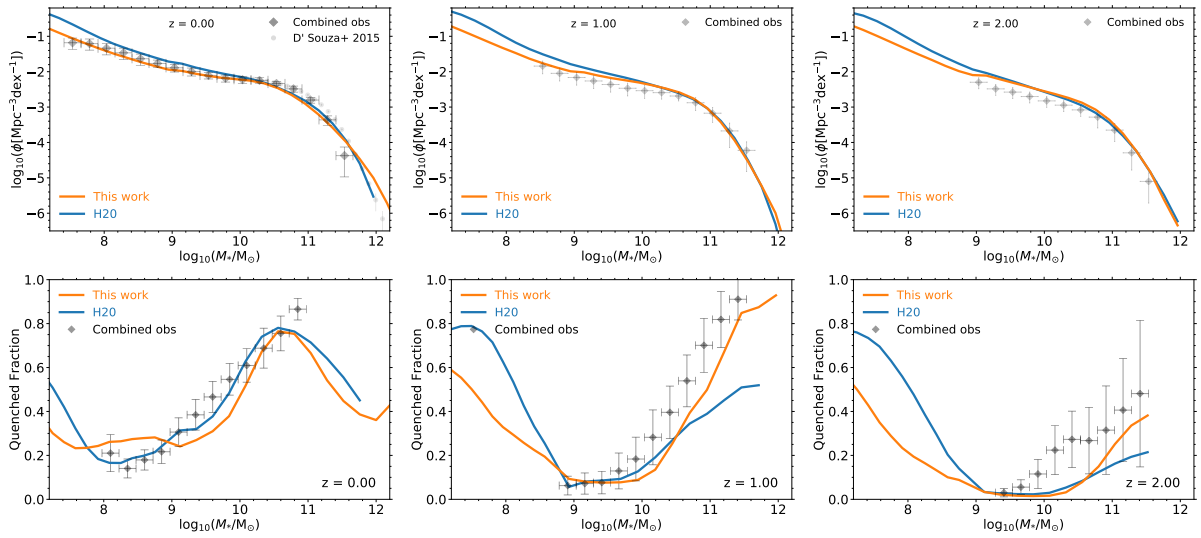
Figure 4.3: Model results for the quantities used as observational constraints in the MCMC in comparison with observations and with the H20 model. The top panels show the stellar mass functions and the bottom panels show the fraction of quenched galaxies. The combined observations used in the MCMC calibration are taken from H15 (see their Appendix 2 for more details) and include Baldry et al. (2008, 2012); Li & White (2009) for SMF at $z = 0$, Marchesini et al. (2009, 2010); Ilbert et al. (2010, 2013); Domínguez Sánchez et al. (2011); Muzzin et al. (2013); Tomczak et al. (2014) for the SMF at $z > 0$, Bell et al. (2003); Baldry et al. (2004) for the quenched fraction at $z = 0$ and Muzzin et al. (2013); Ilbert et al. (2013); Tomczak et al. (2014) for the quenched fraction at $z > 0$.

than the result of fits to observations. Our observational constraints, i.e. the stellar mass function and quenched fraction, are global values and do not distinguish between field galaxies and those in dense environments. In the rest of this chapter, we study our model's predictions regarding the properties of galaxies in different environments.

4.3 Observational data and Mock catalogues

4.3.1 Observational data

The fraction of quenched galaxies at $z = 0$

For consistency and to ensure the most robust comparisons between our model and empirical data, we carry out a new analysis of observations which constrain galaxy quenched fractions as a function of environment. Our galaxy sample at $z = 0$ is taken from the Sloan Digital Sky Survey Data Release 7 (SDSS-DR7, Abazajian et al. 2009), with stellar masses and star formation rates calculated using the methodologies described in Kauffmann et al. (2003); Brinchmann et al. (2004); Salim et al. (2007). We cross-match the SDSS-DR7 catalogue with the group catalogue from Yang et al. (2005, 2007) to identify the most massive galaxy of each group, the so-called central galaxy. We note that there are a lot of complexities associated with group-finding in observational data (e.g. see Bravo et al. 2020; Tinker 2020). We estimate the halo M_{200} and R_{200} using our galaxy formation model by fitting the central galaxy stellar to halo mass relation as described in §4.3.2 and Appendix A.

For each halo, we find galaxies with line-of-sight velocity separation from the central galaxy in the halo $|v_{\mathrm{gal,LOS}} - v_{\mathrm{halo,LOS}}| \leq \pm 10 V_{200,\mathrm{halo}}$ which lie within a 2D projected halocentric distance of $10 R_{200}$. We note that, for most of our analysis we only take galaxies with $|v_{\mathrm{gal,LOS}} - v_{\mathrm{halo,LOS}}| \leq \pm 2 V_{200,\mathrm{halo}}$ (e.g. see Figs. 4.10,4.11). In this work, we limit our SDSS galaxy sample to galaxies with $\log_{10}(M_\star/\mathrm{M}_\odot) \geq 9.5$ and our observational halo sample to haloes with $\log_{10}(M_{200}/\mathrm{M}_\odot) \geq 12$. The redshift interval of our host haloes is taken as $0.01 \leq z \leq 0.04$. Finally, we adopt the definition that galaxies with $\log_{10}(\mathrm{SSFR/yr^{-1}}) < -11$ are quenched.

A similar analysis has been carried out by Wetzel et al. (2012, 2014), where they use the SDSS data and a modified Yang et al. (2007) halo catalogue to study the properties of galaxies in different environments. In contrast, our new analysis is based on a different halo catalogue, halo mass derivation method, stellar and halo mass bins, and so on. Furthermore, the analysis in this work is designed so that the results can be compared directly and self-consistent with our SAM model predictions.

The fraction of quenched galaxies at $z > 0$

At $z > 0$, we compare our results with the fraction of quenched galaxies inferred from the Hyper Suprime-Cam Subaru Strategic Program (HSC-SSP) survey data of optical broadband photometry from Pintos-Castro et al. (2019). Their analysis is based on the

HSC-SSP project (Aihara et al. 2018). In their study, galaxy clusters are taken from the SpARCS (Muzzin et al. 2009; Wilson et al. 2009) fields, using a modified cluster red sequence algorithm by Gladders & Yee (2000, 2005); Muzzin et al. (2008) that employs photometric redshifts.

4.3.2   Mock catalogues

In order to make a fair comparison with observations, we create mock catalogues both from our own model and from that of H20. The details are explained in this subsection.

Projection in 2D

In order to compare with the SDSS data at $z = 0$, to locate galaxies in the vicinity of each halo in our model, we first transform the galaxy distribution into redshift/velocity space. This is done using their positions and peculiar velocities along the z-axis of the simulation domain, accounting for expansion due to the Hubble flow. For each simulated halo we locate nearby galaxies with $|v_{\mathrm{gal,LOS}} - v_{\mathrm{halo,LOS}}| \leq \pm 2V_{200,\mathrm{halo}}$ within a 10 Mpc projected halocentric distance.

For our comparison with the HSC data (Pintos-Castro et al. 2019) at $z > 0$, we adopt the projection made by Pintos-Castro et al. (2019) within a redshift slice of

$$\Delta z = z_{\mathrm{halo}} \pm 0.05 \times (1 + z_{\mathrm{halo}}). \tag{4.2}$$

The physical distance corresponding to Δz could exceed our simulation box size for some redshifts. Therefore for simplicity we project the entire simulation box along the z-axis of the simulation volume ($l_{\mathrm{box}} \sim 700\,\mathrm{Mpc}$ for the Millennium simulation in the Planck cosmology).

Deriving halo mass and radius

For each central galaxy in both models and observations we calculate a halo mass, M_{200}, from its stellar mass with the fitting formula below (motivated by Yang et al. 2003; Moster et al. 2010):

$$\log_{10}(M_{200}/\mathrm{M}_\odot) = \alpha_1 \log_{10}(M_\star/\mathrm{M}_\odot) + \beta_1, \tag{4.3}$$

where α_1 and β_1 are free parameters which we derive using our final, calibrated model output (see Figs. A.1,A.2 in appendix A): $\alpha_1 = 1.65$, $\beta_1 = -5.16$ for $\log_{10}(M_\star/\mathrm{M}_\odot) \geq 10.5$, and $\alpha_1 = 0.80$, $\beta_1 = 3.70$ for $\log_{10}(M_\star/\mathrm{M}_\odot) < 10.5$. The above equation is valid for galaxies with $\log_{10}(M_\star/\mathrm{M}_\odot) > 9.5$. The stellar mass at which α_1 and β_1 change is $\log_{10}(M_\star/\mathrm{M}_\odot) = 10.5$ which roughly corresponds to haloes with $\log_{10}(M_{200}/\mathrm{M}_\odot) \sim 12.2$. For each halo, R_{200} is calculated from M_{200} through

$$R_{200} = \left(\frac{3M_{200}}{4\pi \times 200\rho_{\mathrm{crit}}} \right)^{1/3}. \tag{4.4}$$

We note that independent values of halo mass and radius are given in the Yang et al. (2005, 2007) catalogue as well. There were calculated from abundance matching using the observed stellar mass function and an analytical halo mass function. In contrast, here we use the median stellar mass to halo mass ratio at each stellar mass bin in our model, which does not invoke the same assumptions as abundance matching. In practice, the differences between their values and ours are quite small.

For our direct comparisons with the SDSS observations, wherever the halo mass, M_{200} and the halo radius, R_{200}, are needed, we derive M_{200} using Eq. 4.3. The corresponding R_{200} is then derived using Eq. 4.4. We do this for the data *as well as* for the models. We note that such a derivation of M_{200} and R_{200} leads to considerable scatter in halo mass and radius compared with the actual values measured directly from the simulation. This is explained in more detail in Appendix A (see Figs. A.1, A.2).

For our comparison with the HSC data (Pintos-Castro et al. 2019) at $z > 0$, we use the direct simulation halo masses rather than making a mock catalogue. This is because there are many complexities in the technique that work employs to derive halo masses, that are beyond the level we wish to emulate in this work. We note that this makes our high redshift comparisons less reliable (see §4.4).

Homogenization of the halo mass distributions between models and observations

In general, the halo mass distribution within a given halo mass bin (e.g. haloes with $14 < \log_{10}(M_{200}/\mathrm{M_\odot}) < 15$) can differ between the observations and the models. This bias could affect our results and conclusions. Therefore, we re-sample the distribution of simulated haloes to match the observed distributions.

Assume that we want to compare the quantity "Q" (e.g. the fraction of quenched galaxies) between a model and an observation, as a function of M_{200}. We divide each halo mass bin (e.g. $14 < \log_{10}(M_{200}/\mathrm{M_\odot}) < 15$) in the model into smaller sub-bins and calculate the quantity Q within those sub-bins. The final value of the quantity Q within the larger bin is

$$Q = \sum_{i=1}^{n} Q_i W_i, \tag{4.5}$$

where Q_i is the value (mean, median, etc.) of Q within the ith sub-bin and "n" is the number of sub-bins. In addition, W_i is the weight of the ith sub-bin, defined as the ratio of the fraction of haloes in the ith sub-bin of the observational sample to the fraction of haloes in the ith sub-bin of the model. This homogenization is only done for our comparison with the SDSS data at $z = 0$.
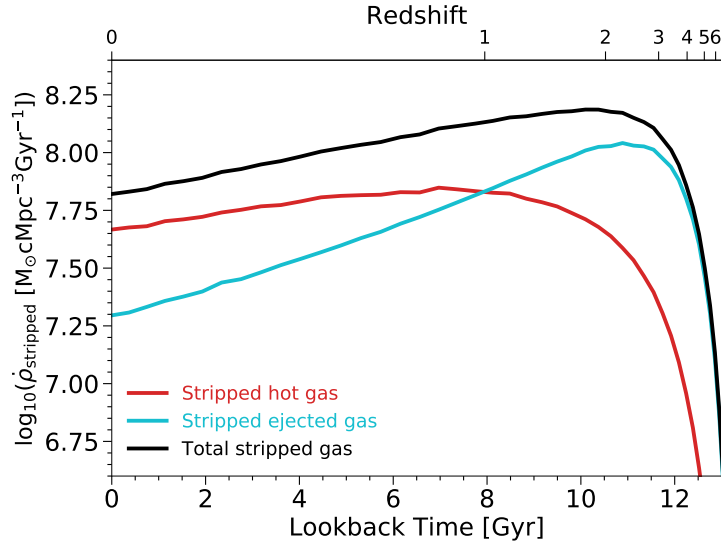
Figure 4.4: Time evolution of the stripping rate density as defined in Eq. 4.6. The red and cyan lines correspond to the stripping rate density of the hot gas (red) and the ejected reservoir (cyan), respectively. Summing the two, the black line is the total gas mass stripping rate density.

4.4 Results

4.4.1 Gas stripping through time

As a first, global exploration of the role of gas stripping, we define the stripping rate density, $\dot{\rho}_{\mathrm{stripped}}(t)$, as the stripped mass in the entire simulation per unit time (gigayear), normalised to the simulation volume:

$$\dot{\rho}_{\mathrm{stripped}}(t) = \frac{1}{V_{\mathrm{simulation}}} \sum_{i=1}^{\mathrm{N_{gal}}} \dot{m}_{\mathrm{stripped,i}}(t), \qquad (4.6)$$

where $\dot{m}_{\mathrm{stripped,i}}(t)$ is the gas stripping rate of the ith galaxy per unit time, and the sum is over all galaxies ($\mathrm{N_{gal}}$). In addition, $V_{\mathrm{simulation}}$ is the comoving simulation volume.

Fig. 4.4 shows $\dot{\rho}_{\mathrm{stripped}}(t)$ as a function of lookback time (lower x-axis) as well as redshift (upped x-axis). Considering the redshift evolution of $\dot{\rho}_{\mathrm{stripped}}$, most of the stripped gas at $z > 1.2$ is due to the stripping of the ejected material (cyan line) rather than the hot halo gas (red line), demonstrating a strong correlation between feedback processes and gas stripping at high redshifts. At $z < 1.2$, stripping of the hot gas is the dominant stripping process.

In L-GALAXIES, the outflows contributing to the ejected reservoir are caused by supernova feedback and are present mostly for low-mass galaxies. We note that AGN feedback in our model prevents the hot gas from cooling but does not eject it outside the halo.

Therefore, it does not contribute to the material in the ejected reservoir. Some hydrodynamical simulations (e.g. IllustrisTNG) have strong outflows caused by black hole feedback in massive galaxies. As discussed in Chapter 2, the presence of ejective black hole feedback results in a significant enhancement in ram-pressure stripping for massive galaxies. We will consider the possibility of ejective black hole feedback and study its influence on gas stripping in L-GALAXIES in future work.

The total stripping rate density (black line) does not decrease monotonically with redshift, but it has a maximum at $z \sim 2$. The same is true for the ejected stripped density rate (blue line) with a maximum at $z \sim 2$, implying a close relationship to the peak of cosmic star formation rate density which also occurs at $z \sim 2$ (see Fig. 4.14). Due to the maximal total star formation rate at $z \sim 2$ there is an abundance of powerful stellar feedback activity in L-GALAXIES, and the largest fraction of ejected material at this cosmic epoch. This results in the suppression of the hot gas density in galaxies and, as a result, the suppression of the gravitational force between the galaxies and their hot halo gas (Eq. 3.2). Therefore, the hot and ejected gas of galaxies are more easily stripped.

Fig. 4.5 shows the median cumulative stripped fraction (Eq. 4.1) up to $z = 0$, versus halocentric distance, for galaxies in the vicinity of clusters (right row), groups (middle row) and lower mass haloes (left row). We stack all galaxies in the vicinity of haloes as a function of distance, and in each panel the curves show median values at each distance bin. The solid and dotted lines correspond to central and satellite galaxies, respectively.

The top panel of Fig. 4.5 shows the total stripped fraction of galaxies by $z = 0$. We also divide the stripped fraction into two categories based on whether they were central or satellite galaxies when stripping occurred. In particular, the stripped fractions in the middle and bottom rows are calculated only when a galaxy is either a satellite, or a central, respectively. Therefore, the top panel is the sum over the middle and bottom panels. In the rest of this subsection, we use Fig. 4.5 as a reference to describe the model predictions for gas stripping in different types of galaxies.

Gas stripped out of satellite galaxies

The middle panel of Fig. 4.5 shows that $z = 0$ satellite galaxies (dotted lines) lose a fraction of their gas after infall. There is a trend with distance for galaxies near FOF haloes: galaxies closer to the halo centre have lost more gas. That is a direct influence of environmental processes, as galaxies closer to the halo centre reside in denser environments and are more strongly stripped. There is a minimum amount of stripping at $R/R_{200} \sim 1-3$. This is where the most distant satellites of the FOF haloes reside, i.e. the characteristic scale at which galaxies change type from central to satellite according to the halo finder algorithm. Among all satellites, the most distant are the least influenced by environmental effects. Beyond this scale, satellite galaxies belong to other FOF haloes and are mostly closer to the centre of their respective hosts. As a result, they are more strongly stripped. The resulting stripped fraction increases with distance beyond this characteristic scale, until reaching a constant, mass-dependent, global value.

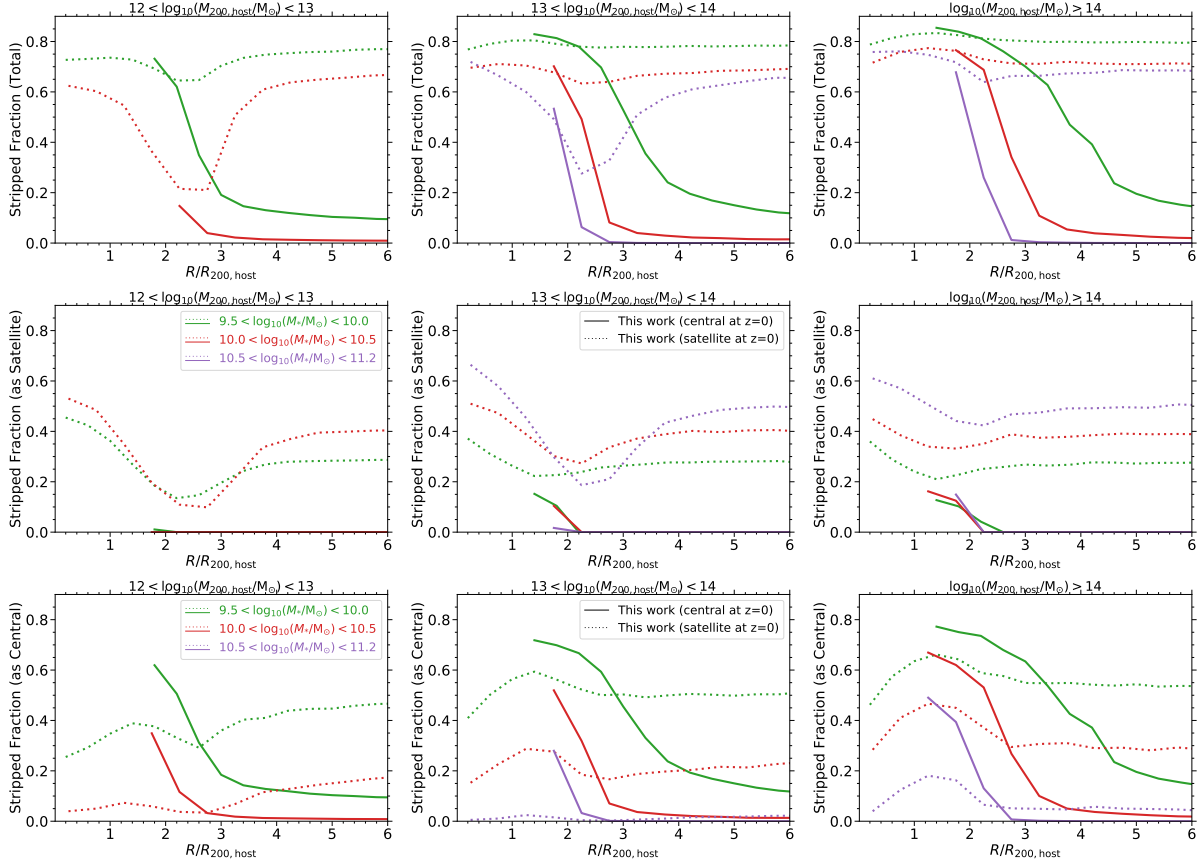Galaxies that are centrals at $z = 0$ could have been satellites at some point in their

Figure 4.5: The median cumulative stripped fraction of gas (Eq. 4.1) in galaxies as a function of halocentric distance at $z = 0$. Different columns show results for different central host halo masses. In all the panels, different colours correspond to different stellar mass ranges (indicated in the legends) and different line styles correspond to central galaxies (solid) versus satellites (dotted). The top row shows the total stripped fraction, which is divided into two categories as shown in the middle and bottom rows: the cumulative gas stripped from galaxies when they were satellites (middle row) versus when they were centrals (bottom row). Galaxies experience significant stripping, both when they are satellites, and when they are centrals (see text for details).

history. These galaxies are mainly flyby or splashback systems, i.e. former satellites of other central haloes. Flyby galaxies enter a halo, traverse it, and then leave without becoming bound to the halo, while splashback galaxies remain bound to that halo and can reach apocenter before possibly returning. The solid lines in the middle row of Fig. 4.5 represent the gas stripped out of these two kinds of galaxies. They are the central galaxy of their own halos at $z = 0$, and the stripped gas shown with solid lines is calculated when they were satellites of other haloes at $z > 0$. There is a characteristic scale at $R/R_{200} \sim 1.5 - 2$ where these galaxies show any signs of having lost gas, which corresponds to the splashback radius of the nearby central halo at $z = 0$.

Gas stripped out of central galaxies

While gas stripping out of satellite galaxies is expected, central galaxies are less often imagined to experience significant stripping. As illustrated in the bottom panel of Fig. 4.5, our model shows that galaxies can in fact lose a non-negligible fraction of their hot gas due to stripping while they are centrals. The stripped fraction decreases with halocentric distance for galaxies that are centrals at $z = 0$ (solid lines), and can reach 80% in the median for low-mass central galaxies in the vicinity of clusters (bottom right panel, solid lines). Interestingly, more than half of the current massive central galaxies near clusters (bottom right panel, solid purple lines) have lost more than half of their gas due to stripping beyond $\sim 1.5 R_{200}$.

Our model predicts that $z = 0$ satellite galaxies (dotted lines in Fig. 4.5) lose a large fraction of their hot gas prior to infall, when they are the central galaxy of their own halo. This is illustrated in the bottom panel of Fig. 4.5 (dotted lines). There is a local maximum at $R/R_{200} \sim 1 - 2$, corresponding to where these galaxies change type from central to satellite. At this scale, the overall stripped fraction is very similar for central versus satellite galaxies, reflecting the uniformity of our gas stripping approach in treating different types of galaxies. For satellite galaxies with $R/R_{200} \lesssim 1 - 2$, the fraction of the gas they have lost as a central decreases towards the centre of the halo: galaxies close to the halo centre have earlier infall times, and have spent a correspondingly longer time as satellites than more distant galaxies.

There is an overall trend with stellar mass. The top panel of Fig. 4.5 shows that the total stripped fraction decreases with stellar mass (green, to red, to purple). The reason is the weaker gravitational binding energy of low-mass systems. The trend is reversed for the stripped fraction *as satellites* (middle panels), because low-mass galaxies lose a larger percentage of their gas prior to infall when they were still the central galaxy of their own halo (bottom panel). Therefore, there is not much residual gas available to be stripped once they later become satellites.

4.4.2   Gas content of galaxies and subhaloes

Gas content is the quantity most affected by our new stripping method. In this subsection, we analyse the predictions of our model for hot (non-star-forming) and cold (star-forming)
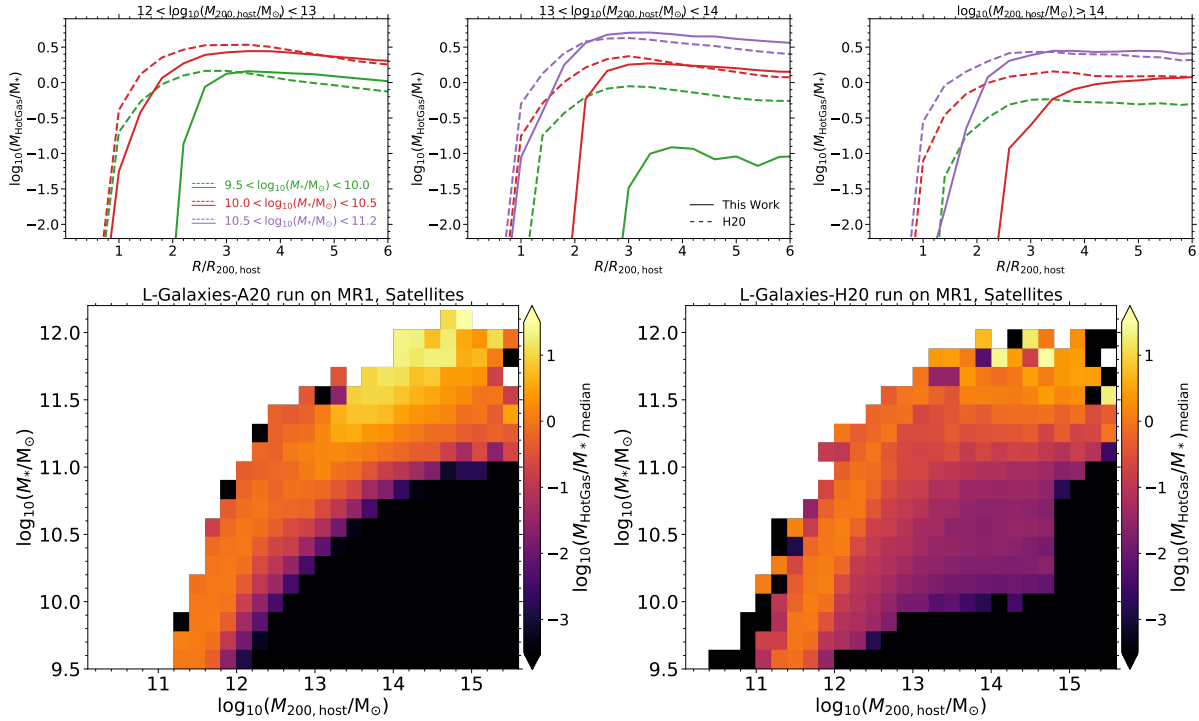
Figure 4.6: Top panel: Hot gas to stellar mass ratio as a function of halocentric distance at $z = 0$, as a function of host mass (three columns), stellar mass (line colors), and model (line styles). Bottom panel: 2D histograms of the hot gas to stellar mass ratio of satellite galaxies as a function of their host halo mass (x-axis) and stellar mass (y-axis), contrasting this work (left panel) and H20 (right panel).

gas, comparing to observations and the H20 model.

Hot (non-star-forming) gas

In the top panel of Fig. 4.6 we show the hot gas to stellar mass ratio, $M_{\mathrm{hotgas}}/M_\star$, as a function of halocentric distance for galaxies in the vicinity of clusters (top right), groups (top middle), and lower mass haloes (top left). For both models (different line styles) and at all stellar mass ranges (different colours), the $M_{\mathrm{hotgas}}/M_\star$ ratio decreases with decreasing halocentric distance from a constant global value. The radius at which the ratio starts to decrease in our model is larger than in H20, showing the impact of more spatially extended gas stripping in the new model.

The hot gas to stellar mass ratio decreases with the halo mass, reflecting the fact that gas stripping processes are more efficient in the dense regions surrounding the most massive halos. Interestingly, the difference between our model and H20 is more significant near massive haloes (right panel), showing the importance of modelling ram-pressure self-consistently in all environments. Moreover, the hot gas to stellar mass ratio increases with galaxy stellar mass. This is also a direct impact of stripping as discussed in §4.4.1 (see Fig.
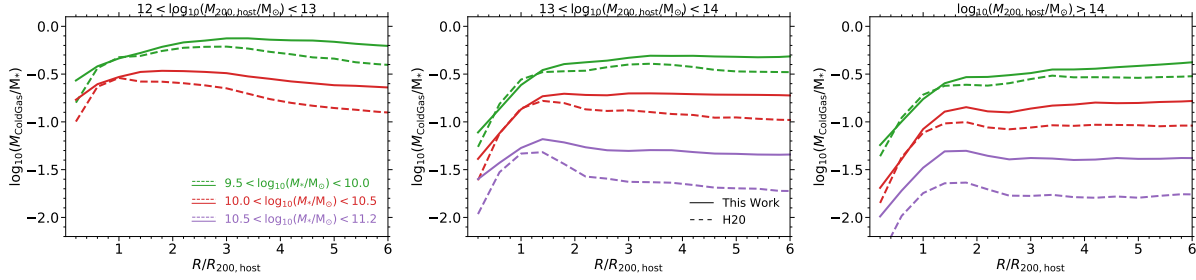
Figure 4.7: Cold gas to stellar mass ratio as a function of halocentric distance at $z = 0$. We show the dependence on host halo mass (three columns), stellar mass (colours), and contrast our updated model with H20 (linestyles).

4.5).

The dependence of this ratio on the stellar mass of satellites, as well as their host halo mass, is illustrated in the bottom panels of Fig. 4.6. The 2D histogram is coloured by the median value of $\log_{10}(M_{\mathrm{hotgas}}/M_\star)$. In H20 (right panel), there is an abrupt transition at $\log_{10}(M_{200}/\mathrm{M_\odot}) \sim 14.7$. This results from H20 only applying ram-pressure stripping to satellites within R_{200} of haloes with $\log_{10}(M_{200}/\mathrm{M_\odot}) \gtrsim 14.7$ (see §1.2.8 and §4.2.1). On the other hand, such a sharp transition is not present in our model, and low-mass satellite galaxies are more gas-poor than in H20, due to both pre-infall and post-infall stripping.

Cold star-forming gas in galaxies

The cold gas component is also affected by environmental processes. However, as we do not implement cold gas stripping directly, we do not expect our model to differ significantly from H20 in this regard. Fig. 4.7 shows the median cold gas to stellar mass ratio as a function of halocentric distance. As before, galaxies in the vicinity of haloes are stacked and the lines represent the median values at each radial distance bin.

In both models, $M_{\mathrm{coldgas}}/M_\star$ increases with distance and reaches a constant global value at $R/R_{200} \sim 1-2$. The trend with distance roughly follows the trend of $\log_{10}(M_{\mathrm{hotgas}}/M_\star)$ (Fig. 4.6, top panel). However, the influence of environment on the cold gas extends out to smaller radii than is seen for the hot gas. Only when galaxies run out of hot gas does cold gas component cease to grow. Subsequently, as star formation continues, the cold gas mass decreases further until either it is exhausted, or the galaxy merges.

Fig. 4.8 shows the HI mass function for galaxies in our model (orange lines), H20 (blue lines), and observations (grey points, Zwaan et al. 2005; Haynes et al. 2011; Jones et al. 2018). Two different runs are shown for each model: L-Galaxies run on the Millennium and Millennium-II simulations. Due to the better resolution of the Millennium-II simulation we can extend the model results down to lower HI masses. On the other hand, the Millennium simulation provides better statistics for larger M_{HI} values. Both our model and H20 are in relatively good agreement with observations. However, we note that H20 uses the HI mass function as an observational constraint for their model calibration, while
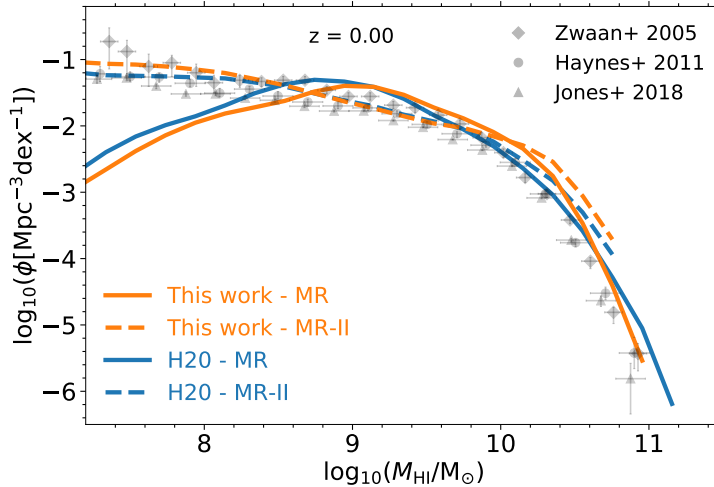
Figure 4.8: HI mass function from this work in comparison with H20 and with observations from Zwaan et al. (2005); Haynes et al. (2011); Jones et al. (2018).

we do not.

4.4.3   Star formation and galaxy quenching

Direct model predictions

We move on to study the star-formation activity, and quenching, of galaxies. The top panel of Fig. 4.9 shows the fraction of quenched galaxies, f_q, as a function of halocentric distance at $z = 0$. For each halo mass bin (panel) all galaxies in the vicinity of haloes are stacked. The results are shown for different stellar mass bins (different colours) for our model (solid lines) and for H20 (dashed lines). In the vicinity of clusters (top right), f_q decreases with distance in both models and flattens at a distance that is always larger than the halo boundary, R_{200}. There is a clear trend with halo mass: galaxies in the vicinity of more massive haloes are more quenched. This follows directly from what we showed in §4.4.2 (Figs. 4.6, 4.7) regarding the gas content of galaxies.

The top panel of Fig. 4.9 often reveals a minimum in the quenched fraction at $R/R_{200} \sim 1 - 2$. This is where the most distant satellites of FOF haloes reside, i.e. where they are the least influenced by their environment. At halocentric radii smaller than this scale, satellite galaxies are strongly influenced by their host halo. Beyond this scale, satellites belong to other FOF haloes and could be close to their own centrals and, therefore, more strongly influenced by environmental processes. The contribution of those satellites at $R/R_{200} > 2$ in the total quenched fraction (i.e. centrals and satellites together), is sufficient to cause a quenched fraction larger than the value at $R/R_{200} \sim 1 - 2$, causing the minimum. We note that this directly follows the minimum of the cumulative stripped fraction as shown by dotted lines in the top panel of Fig. 4.5.

Comparing with H20, gas stripping in our model affects f_q to larger halocentric dis-

tances. In order to quantify this, we define a characteristic radius called $R_{c,20\%}$ at which the quenched fraction is 20% above its field value,

$$f_q(R_{c,20\%}) - f_{q,\text{field}} = 0.2 \,, \tag{4.7}$$

where $f_{q,\text{field}}$ is the fraction of quenched field galaxies, calculated for galaxies with halo-centric distance in the range of $5 < R/R_{200} < 10$. The middle row of Fig. 4.9 shows $R_{c,20\%}/R_{200}$ (normalised to the host halo R_{200}) for our model (solid lines) and H20 (dashed lines) as a function of halo mass. The results are shown for two different stellar mass ranges (middle left and middle right panels) at different redshifts (different colours).

Our model quenches galaxies in the vicinity of massive haloes to much larger halo-centric distances than H20 at all redshifts. At $z > 2$, there is no distance within which galaxies become 20% more quenched than field galaxies. This indicates that the influence of environmental processes on galaxy quenching is non-negligibly visible only since $z \sim 2$. At $z \lesssim 1$, $R_{c,20\%}/R_{200}$ in our model is on average four times larger than in H20. We also observe a trend with halo mass: galaxies in the vicinity of more massive haloes are quenched up to larger fractions of their R200. The same trend is not present in H20 or is very weak. Moreover, there is no significant correlation with redshift, except for $z \gtrsim 2$ where $R_{c,20\%}/R_{200}$ is either small (pink lines, middle row of Fig. 4.9) or is not present. Comparing the two panels in the middle row of Fig. 4.9, $R_{c,20\%}/R_{200}$ decreases with stellar mass, i.e. low-mass galaxies are strongly influenced by their environment out to larger distances.

Environment can also influence intrinsic physical processes such as stellar and black hole feedback. As an example, consider galaxies with $10.5 < \log_{10}(M_{\text{star}}/M_\odot) < 11.2$ that reside in the vicinity of clusters in our model (solid purple line, top right panel). When the gas is removed, there are two main consequences: (i) their star formation will decrease due to hot gas stripping and a lack of cold gas replenishment, and (ii) the efficiency of their black hole feedback will decrease because it is a function of hot halo gas (see Table 4.2 and the supplementary material). The decrease in black hole feedback allows the hot gas to cool faster, which increases star-formation. Such non-trivial couplings between environmental effects and feedback processes will be explored in more detail in future work.

Finally, the bottom panel of Fig. 4.9 shows 2D histograms of the quenched fraction of satellite galaxies as a function of stellar mass and host halo mass. In both our model (bottom left) and H20 (bottom right), there is a strong trend with halo mass, and in general, satellites of more massive hosts are more quenched. In addition, the quenched fraction increases with stellar mass. Comparing the two models, our model has more quenched satellites than H20 at all stellar and host halo masses. Significantly, satellites with $\log_{10}(M_\star/M_\odot) < 10$ residing in groups with $13 < \log_{10}(M_{200}/M_\odot) < 14$ are more quenched in our model than in H20. This is due to gas stripping both within groups and prior to infall.
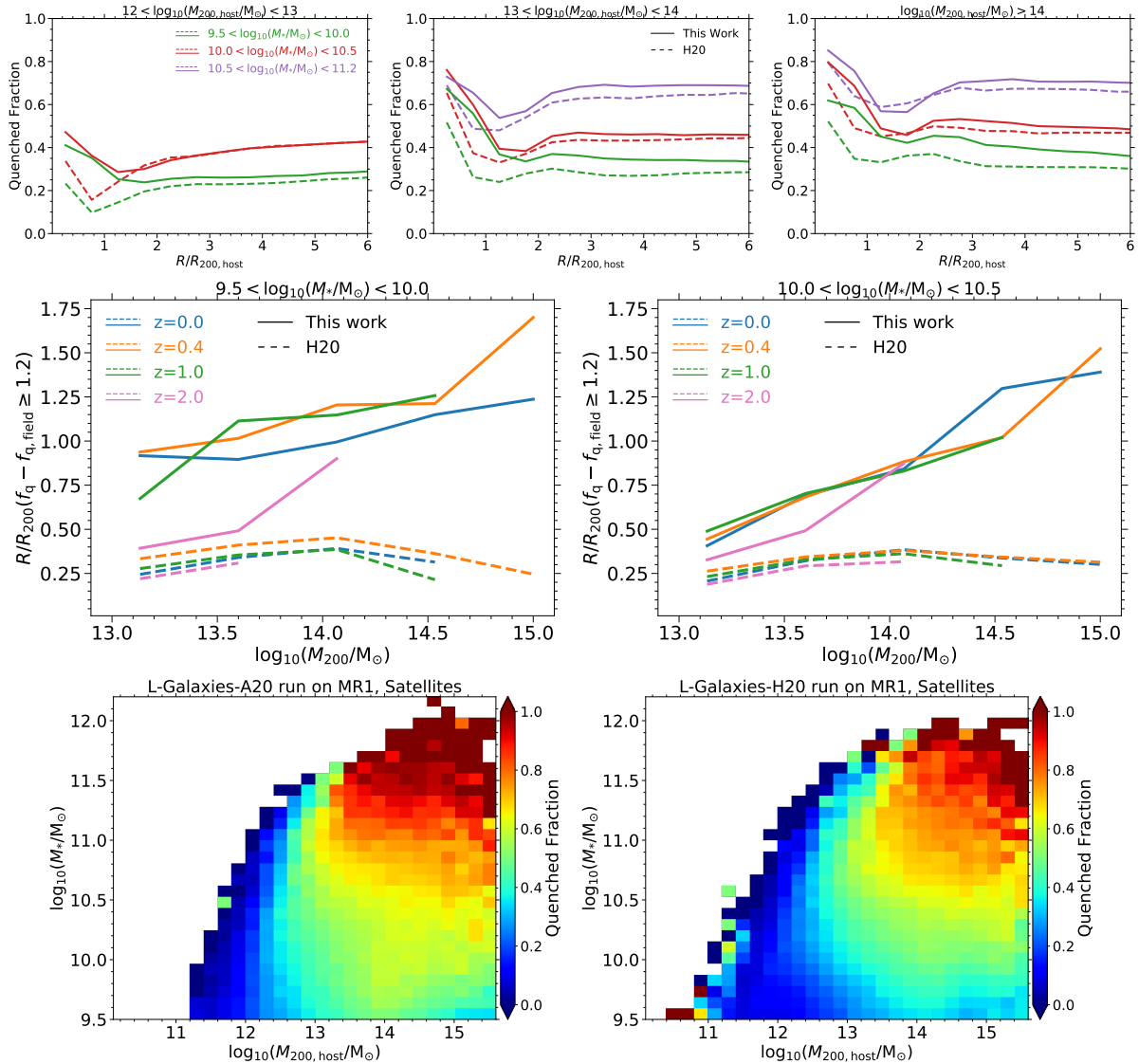
Figure 4.9: Top panel: Fraction of quenched galaxies as a function of halocentric distance at $z = 0$. Middle panel: Halocentric radius at which the quenched fraction is 20% above the field value vs. the halo mass both for this work and for H20 at different redshifts. Bottom panel: 2D histograms of the quenched fraction of satellite galaxies as a function of their host halo masses (x-axis) and their stellar masses (y-axis) in this work (left panels) and in H20 (right panels) at $z = 0$. At $z = 0$, galaxies with $\log_{10}(\mathrm{SSFR/yr^{-1}}) < -11$ are considered as quenched and at $z > 0$ galaxies with $\mathrm{SSFR/yr^{-1}} < (1 + z)/(2 \times 10^{10})$ are considered as quenched (following the quenching criteria in H20).

Comparing with observations at $z = 0$

We compare our results for the fraction of quenched galaxies in different environments with SDSS observations. For both the models and observations, the halo mass (M_{200}) and radius (R_{200}) are estimated from their stellar masses as described in §4.3.2. The simulations are transformed into redshift/velocity space based on the method explained in §4.3.2. For every dark matter halo, we project the outputs of both our model and H20 along the z-axis of the simulation volume in velocity space with the thickness of the projected slice taken as $|v_{\mathrm{gal,LOS}} - v_{\mathrm{halo,LOS}}| \leq \pm 2V_{200,\mathrm{halo}}$. For observations, the velocity separations are calculated along the lone-of-sight using the galaxy redshifts, and the 2D projected distances are calculated from the sky coordinates.

Fig. 4.10 shows the fraction of quenched galaxies as a function of projected halocentric distance in our model (solid lines), in H20 (dashed lines), and in the SDSS observations (points with errorbars). Each panel corresponds to a host stellar mass (or equivalently halo mass) bin indicated at the top of each panel. The results are shown for three different stellar mass ranges, specified by different colours. We first note that both models reproduce the field quenched fractions as a function of stellar mass. In all the halo mass ranges, a clear trend with distance is present both in the models and in the observations: the quenched fraction decreases with halocentric distance and reaches a constant, field value at some radius usually larger than the halo boundary, R_{200}.

For almost all stellar and host mass regimes our model shows better agreement with observations than H20. In the vicinity of massive haloes (top panel), the environmental dependence of quenched fraction extends to larger radius in our model and in SDSS compared to H20. Looking specifically at low-mass galaxies in the vicinity of clusters (top panel, green lines and points), our model and SDSS show that up to 60-70% of galaxies near the halo centre are quenched, while this value is 10-20% lower in H20. While our model is in better agreement for intermediate-mass (red lines and points) and massive (purple lines and points) galaxies, it underpredicts the fraction of quenched massive and intermediate-mass galaxies at $1 < R/R_{200} < 3$.

We suggest two reasons for this discrepancy which can motivate future model developments. The first is a lack of cold gas stripping in our model, which can be accommodated within our LBE framework, while the second is a lack of ejective AGN feedback. It is possible that strong ejective feedback can push gas outside the halo boundary. Infalling galaxies passing through this ejected gas experience substantial enhancement in ram-pressure and can therefore lose a larger fraction of their halo gas, as we see in the IllustrisTNG simulations. Furthermore, in massive galaxies with $\log_{10}(M_\star/\mathrm{M}_\odot) > 10.5$, AGN feedback makes extended subhalo gas less bound which results in an enhancement of ram-pressure stripping and thus galaxy quenching (see Chapter 2).

Considering galaxies surrounding groups (middle panel) and lower mass haloes (bottom panel; Fig. 4.10), our model is again in reasonably good agreement with observations, while H20 exhibits weaker effects within R200 and the dependence of the quenched fraction of distance flattens at smaller distances comparing to our model and SDSS. The persistence of the variation in quenched fraction out to large halocentric distances is even more marked
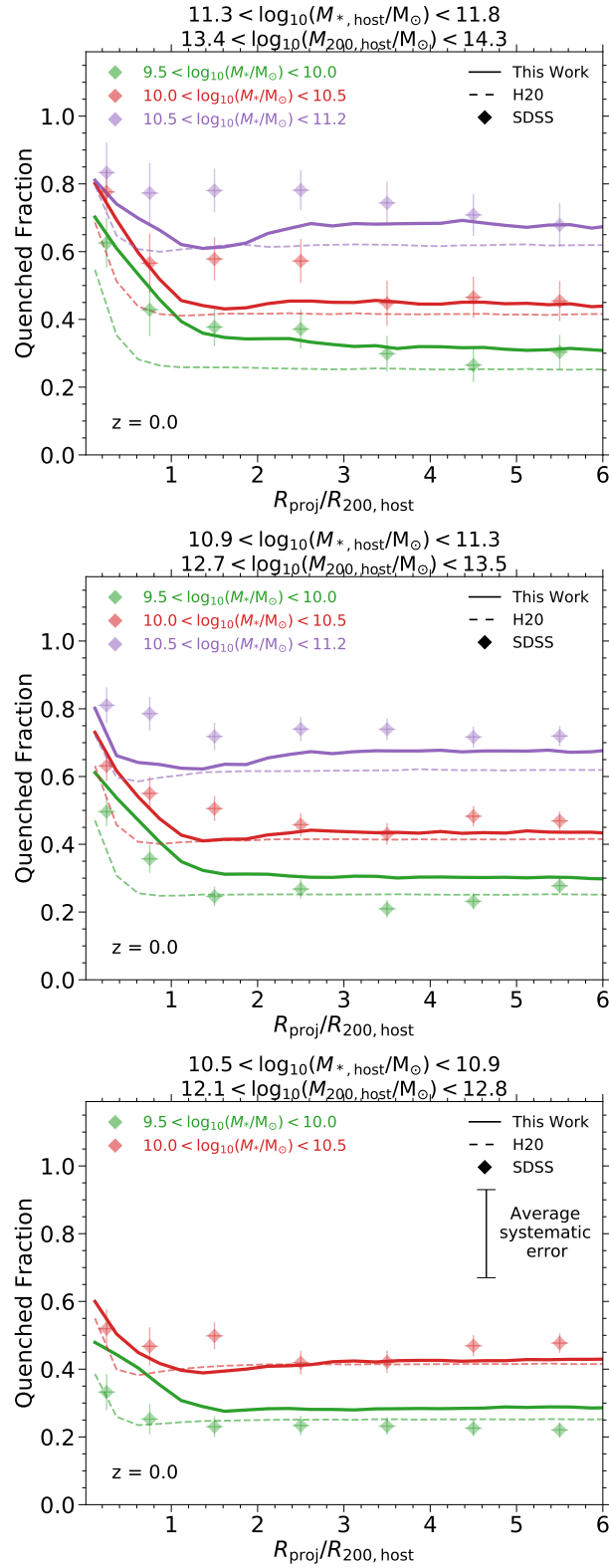
Figure 4.10: Fraction of quenched galaxies vs. projected halocentric distance at $z = 0$. For both models and observations, galaxies with $\log_{10}(\mathrm{sSFR/yr^{-1}}) < -11$ are considered as quenched and the halo mass is calculated using the stellar masses of the central galaxies, based on Eq. 4.3. The error bars are binomial 95% confidence intervals based on a Gaussian approximation.
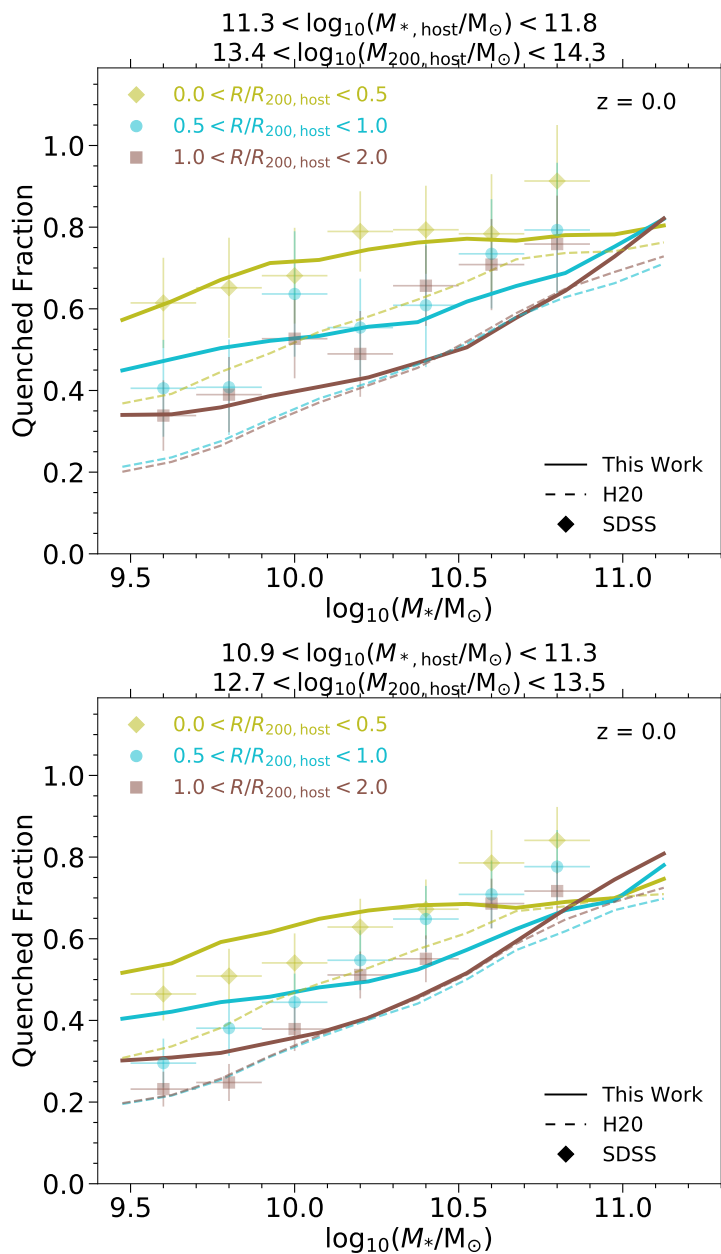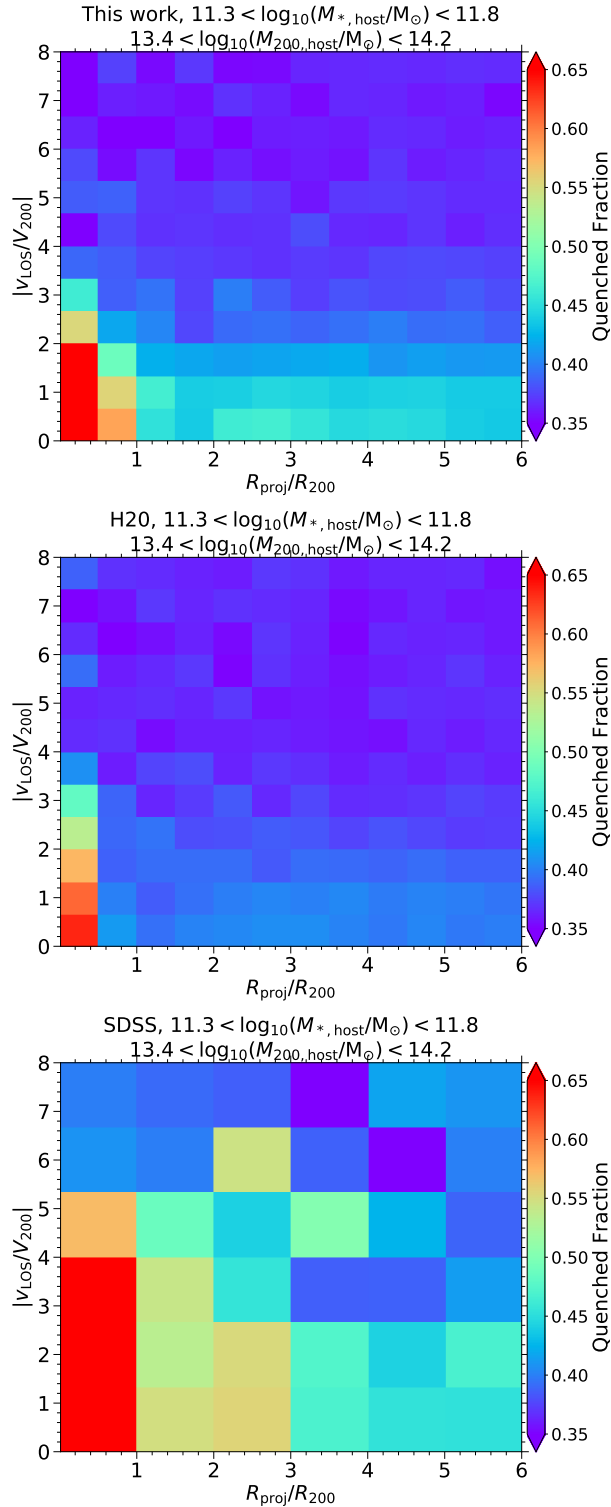
Figure 4.11: Fraction of quenched galaxies as a function of galaxy stellar mass at $z = 0$, comparing the two models to our analysis of SDSS data. For both models and observations, galaxies with $\log_{10} \mathrm{SSFR/yr} < -11$ are considered as quenched. The halo mass in both models and observations are calculated using the stellar masses of the central galaxies, based on Eq. 4.3. The error bars are binomial 95% confidence intervals based on a Gaussian approximation.

Figure 4.12: The fraction of quenched galaxies in projected phase space: as a function of projected halocentric distance (x-axis) and line-of-sight velocity (y-axis). We compare our new model (top panel), H20 (middle panel) and SDSS (bottom panel), defining galaxies with $\log_{10}(\mathrm{SSFR/yr^{-1}}) < -11$ as quenched. All galaxies with $\log_{10}(M_\star/\mathrm{M_\odot}) > 9.5$ are included. Note that the statistics are quite different: the theory panels contain ~ 18000 haloes while only ~ 100 haloes are available in the data.
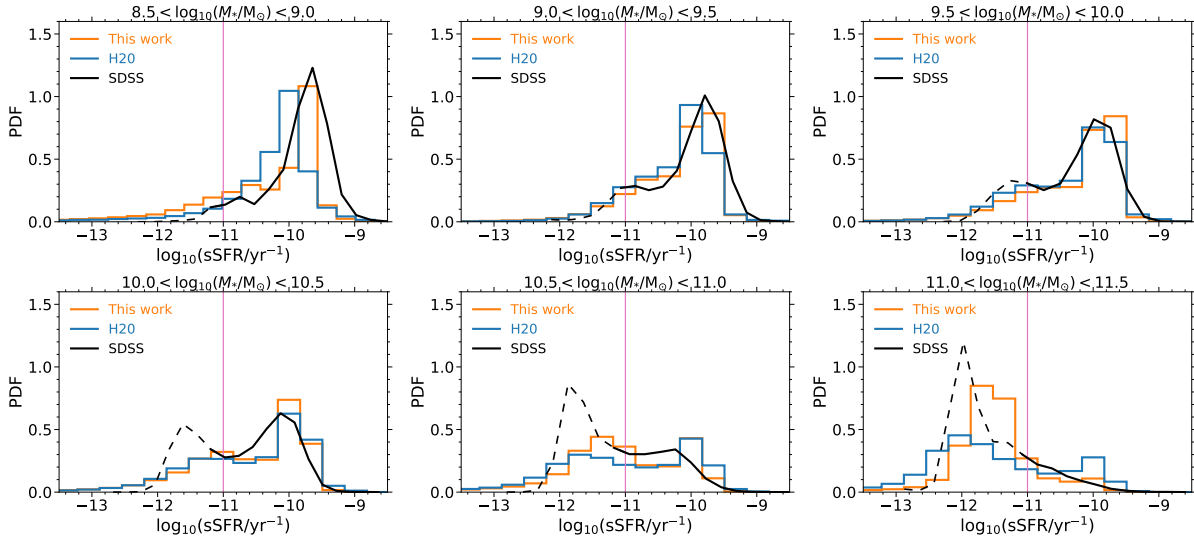
Figure 4.13: Distributions of sSFR for galaxies in this work, H20 and observations. Each panel corresponds to a particular stellar mass range. The SDSS data are based on Brinchmann et al. (2004) with the corrections of Salim et al. (2007). Galaxies with $\log_{10}(\mathrm{sSFR/yr^{-1}}) < -11$ are considered as quenched. Observational data are shown with dashed lines in the regions where there is high uncertainty in the observed specific star formation rates. Despite extensive modification to the stripping properties of galaxies, the sSFR distributions are largely unchanged.

in the SDSS data, a point we will come back to later.

In Fig. 4.11, we show the fraction of quenched galaxies, now as a function of stellar mass, for three different halocentric distance bins (different colours). Different panels correspond to different host stellar (or halo) masses. In general, the quenched fraction almost always increases monotonically with stellar mass for both the models and the observations. In the vicinity of massive haloes (top panel), our model is in relatively good agreement with observations for all the distance bins, while H20 is off by up to 20%. The difference between our model and H20 decreases with stellar mass and is the largest for low-mass galaxies.

Similar results are found for galaxies in the vicinity of intermediate mass haloes (bottom panel of Fig. 4.11), although the difference between our model and H20 is smaller. Overall, our model predictions are in better agreement with observations than H20, and low-mass galaxies in cluster environments are the most influenced by our new gas stripping method.

Fig. 4.12 shows the fraction of quenched galaxies as a function of projected halocentric distance (x-axis) and line-of-sight velocity (y-axis), i.e. projected phase space (PPS; see also Oman et al. 2020). We contrast our model (top panel), H20 (middle panel), and SDSS (bottom panel). In all three cases the quenched fraction decreases both with halocentric distance and with the magnitude of the line-of-sight velocity. As $R_{\mathrm{proj}}/R_{200}$ and $|v_{\mathrm{LOS}}/v_{200}|$ increase, more field galaxies are included in each bin and the quenched fraction eventually approaches the field value. The trend with distance is stronger in our model than in H20,
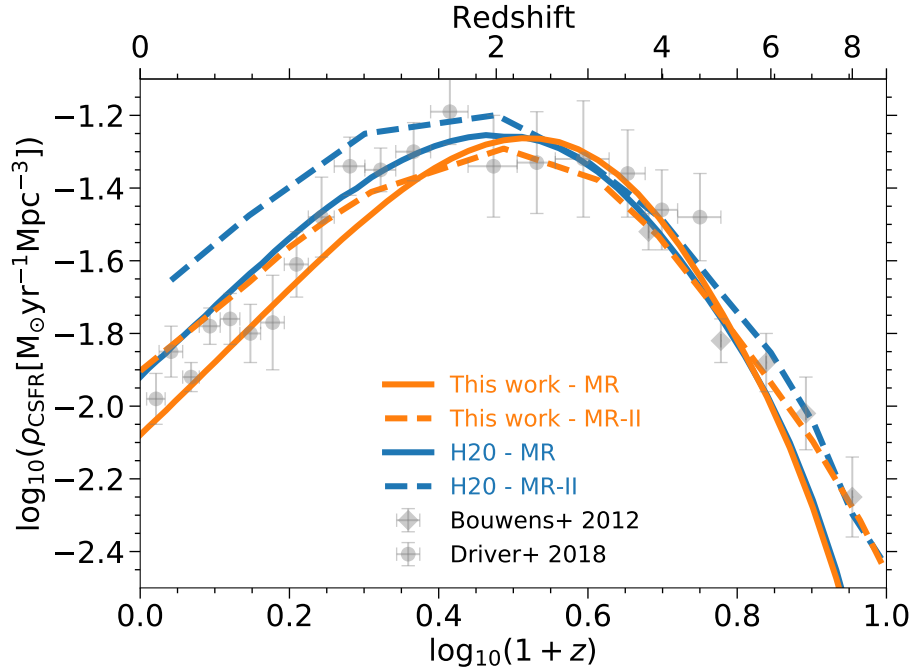
Figure 4.14: Cosmic star formation rate density as a function of redshift for our model, for H20 and for observations from Bouwens et al. (2012); Driver et al. (2018).

but is still weaker than in SDSS. In other words, real haloes seem to influence nearby galaxies out to somewhat larger distances than in either model.

As a final comparison with SDSS data, Fig. 4.13 shows the distributions of specific star formation rate in this work, in H20, and in SDSS observations at $z \sim 0$. Different panels correspond to different stellar mass ranges. SDSS data are shown with black lines, which become dashed where there is high uncertainty in observed star formation rates. The magenta vertical lines at $\log_{10}(\mathrm{sSFR/yr^{-1}}) = -11$ demarcate the value below which galaxies are considered as quenched. Although we have changed the properties of galaxies near massive hosts significantly, the overall specific star formation rates are rather similar. Both our model and H20 are in relatively good agreement with observation. The noticeable difference is for massive galaxies with $11 < \log_{10}(M_\star/\mathrm{M_\odot}) < 11.5$, where our model shows lower specific star formation rates than H20. This is caused by the higher black hole feedback efficiency in our new model.

Beyond $z = 0$: the cosmic star formation rate density

In Fig. 4.14, we compare the cosmic star formation rate density, ρ_{CSFR}, as a function of redshift in the two models to observations taken from Bouwens et al. (2012); Driver et al. (2018). Overall, both models are in agree quite well with data. The two models are similar at redshifts greater than the peak of cosmic star formation rate density, i.e. $z \gtrsim 2$. On the other hand, at lower redshifts, ρ_{CSFR} in our model is smaller than in H20. The maximum

difference between our model and H20 occurs at $z = 0$ where ρ_{CSFR} is 0.15 dex smaller in our model. This is mainly due to our extended gas stripping implementation but also to our higher AGN feedback efficiency. The former mostly affects low-mass galaxies while the latter influences star formation in more massive objects.

Quenched fractions versus observations at $z > 0$

Fig. 4.15 shows the fraction of quenched galaxies versus projected halocentric distance in our model, in H20, and as observed in the HSC survey (Pintos-Castro et al. 2019) at four different redshifts. For this comparison, we take the direct output of our simulation for the halo mass and radius (§4.3.2) and project the whole simulation depth along the z-axis of the simulation volume as a rough approximation of the survey characteristics (§4.3.2).

At all redshifts the quenched fraction decreases with distance both for models and for observations. The agreement with observations is fair for both models, although the quenched fraction of low-mass galaxies in our model (solid green lines) is higher than in H20 (dashed green lines) and than observed (green points) within the virial radius of clusters. At $z = 1$ (bottom right panel), both our model and H20 show a rather strong trend with distance for low-mass galaxies, whereas such a trend is not observed. This could be due to the presence of low-mass quenched galaxies at $z = 1$ which fall outside the observed samples. The overall trend with stellar mass is similar for our work, for H20 and for the observational data. At all halocentric distances and redshifts, the quenched fractions increases with stellar mass.

In both models, the quenched fraction near the cluster centre almost always decreases with redshift, i.e. lower redshift galaxies have higher quenched fractions. On the other hand, comparing observations at $z = 0.4$ and $z = 0.6$ (top left and top right panels), the quenched fraction is higher at higher redshift, the opposite of the trend predicted by the models, possibly due to different methods or definitions of halo mass. It would be best to compare to high redshift data with spectroscopic redshifts to confirm whether these discrepancies are real or are caused by systematic errors of some kind. Observational constraints beyond the local Universe will undoubtedly pose a challenge to theoretical models, and more sophisticated comparisons and future model improvements will further increase our understanding of the role of environment in galaxy evolution.

4.5 Summary and Discussion

In this chapter, we study the impact of environment on the formation and evolution of galaxies. We present a variant of the Munich semi-analytical model of galaxy formation, L-Galaxies, with a novel gas-stripping method. Based on the method we introduced in Chapter 3, we measure the properties of the local environment of every galaxy and subhalo directly from the particle data of the underlying N-body simulations. This enables us to devise a more accurate treatment of environmental processes, particularly ram-pressure stripping. We re-calibrate the parameters of the new model using an MCMC technique
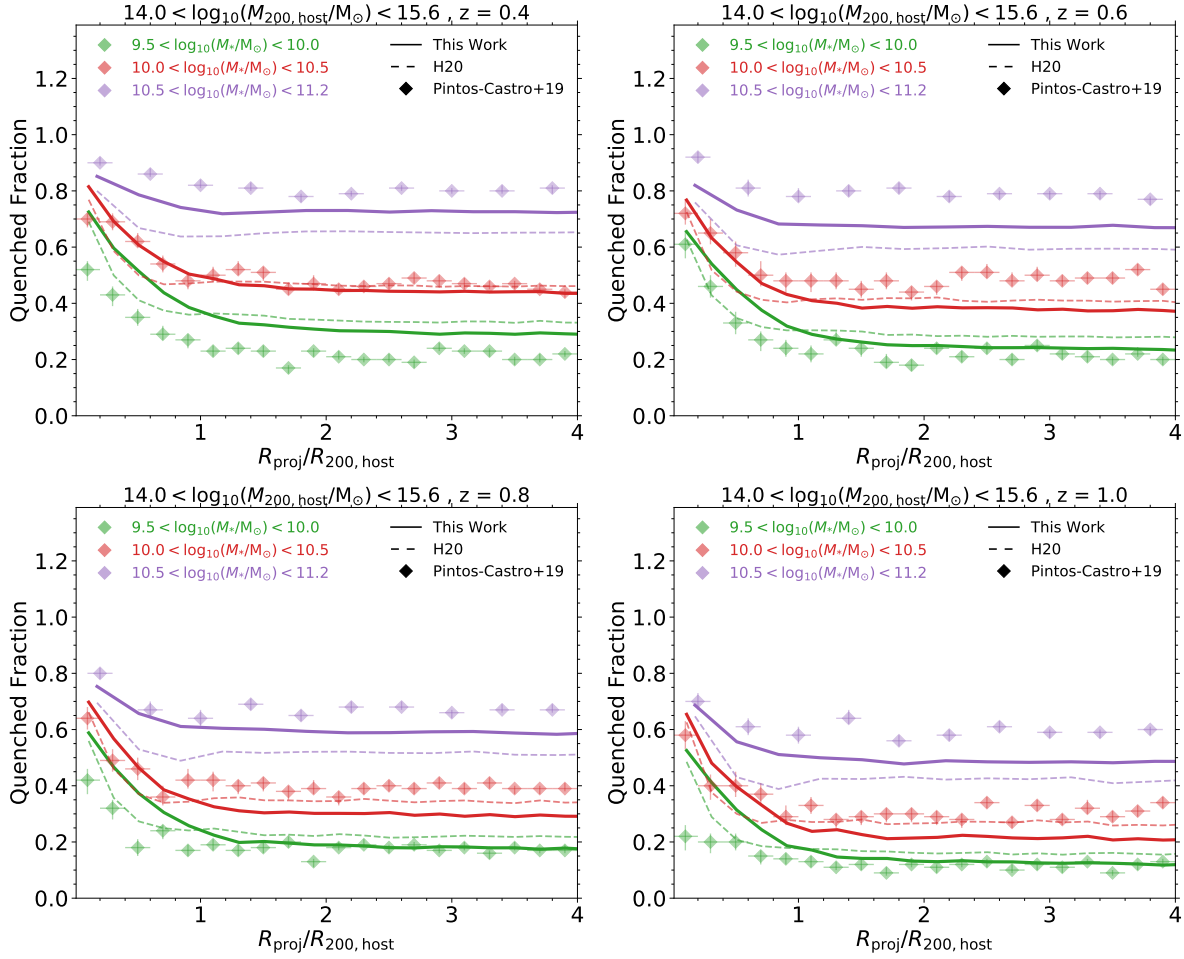
Figure 4.15: Fraction of quenched galaxies as a function of projected distance to centre of clusters at different redshifts. In the models, galaxies with SSFR $< (1+z)/(2 \times 10^{10})$ are considered as quenched. Here we compare to observational data at $0.4 \leq z \leq 1.0$ from Pintos-Castro et al. (2019). Note that in this data a colour cut is used and galaxies with $U - J > 0.88\,(J - V) + 0.59$ are considered as quenched. In comparison to H20, our updated model shows an environmental effect on the quenched fraction which extends to larger halocentric distance.

and a set of observational constraints, namely the stellar mass function and quenched fraction at $z = 0, 1, 2$. Due to this re-calibration, global properties of galaxies such as the stellar mass function, quenched fractions versus galaxy mass and HI mass function are all largely unchanged from H20 and remain consistent with observations. Analysing the results of our new model and the standard model on which it is based (H20), our main results are as follows:

- Measuring the total amount of stripped gas in our model, we find that galaxies in the vicinity of haloes with $M_{200}/\mathrm{M}_\odot > 10^{12}$ lose a large fraction (median $\sim 80\%$ in low-mass galaxies with $9.5 < \log_{10}(M_\star/\mathrm{M}_\odot) < 10$) of their gas due to ram-pressure stripping while they were in fact central galaxies (Fig. 4.5).

- At high redshifts, $z \gtrsim 1$, most stripping is due to gas removal of previously 'ejected' material. At $z \lesssim 1$, in contrast, stripping of the hot halo gas is the dominant contributor (Fig. 4.4).

- The ratio of hot gas to stellar mass, $M_{\mathrm{hotgas}}/M_\star$, decreases with decreasing halocentric distance towards the centres of haloes, due to stripping. In our model, more than half of all galaxies in the vicinity of clusters and groups, up to several virial radii, are almost devoid of hot gas. The dependence of $M_{\mathrm{hotgas}}/M_\star$ on environment extends to much larger halocentric distances in our model than in H20, with low-mass galaxies being more strongly affected by their environment (Fig. 4.6).

- Near clusters and groups in our model, the quenched fraction decreases with halocentric distance, and it flattens to the field value only at $R/R_{200} \lesssim 2-3$, far beyond the halo virial radius (Fig. 4.9).

- The characteristic halocentric distance at which the fraction of quenched galaxies is 20% larger than its field value ($R_{\mathrm{c,20\%}}$) is, on average, four times larger in our model than in H20. In our model, $R_{\mathrm{c,20\%}}/R_{200}$ increases monotonically with halo mass, whereas such a trend is not present in H20 (Fig. 4.9).

We undertake a new analysis of SDSS galaxy data (Abazajian et al. 2009) combined with the Yang et al. (2005, 2007) halo catalogues, inferring the quenched fraction versus halocentric distance out to $R_{\mathrm{proj}} = 10R_{200}$ with a methodology consistent between simulations and data. Together with observational results from the HSC survey, we compare against our model predictions. Our principal results are:

- The $z = 0$ observed trend of the quenched fraction of galaxies (f_{q}) versus halocentric distance (SDSS) is well reproduced in our model up to several halo virial radii, a noticeable improvement over H20. Nevertheless, the observed environmental dependency of galaxies extends to slightly larger distances (Fig. 4.10).

- In our model, as well as in SDSS observations, the quenched fraction near haloes increases with halo mass (Fig. 4.10). The strength of environmental quenching in

the vicinity of haloes also decreases with increasing galaxy stellar mass, which is consistent with the observations (Fig. 4.11).

- At higher redshifts, $0.4 \leq z \leq 1$, our model is in relatively good agreement with observations from the HSC survey, while quantitative differences remain, particularly within the R_{200} of clusters (Fig. 4.15). We note that we have not attempted to model the effect of errors on the photometric redshifts that are used in the data.

- Our predicted HI gas mass function is in good agreement both with the previous model and with $z = 0$ data (Fig. 4.8).

Chapter 5

Conclusions and Outlook

One fundamental aspect affecting the formation and evolution of galaxies is their environment. When galaxies move sufficiently fast in dense regions, environmental processes such as tidal and ram-pressure stripping can strip gas out of galaxies and their subhaloes. These processes influence galaxy properties such as gas content, star formation, colour, stellar mass, morphology, and so on. In this thesis, we study the impact of environment on the formation and evolution of galaxies.

Many of the environmental processes mentioned above occur naturally in hydrodynamical simulations, while they need to be modeled explicitly in semi-analytical models (SAMs) of galaxy formation. Traditionally, SAMs model environmental processes only for satellite galaxies within the halo boundary (typically the virial radius) of their host haloes. That is partly because estimating ram-pressure beyond this scale is difficult without the direct measurement of the density and velocity of the local environment of galaxies. However, several observational (Hansen et al. 2009; von der Linden et al. 2010; Wetzel et al. 2012; Lu et al. 2012) and theoretical (Balogh et al. 1999; Bahé et al. 2012) studies discuss that environmental effects might act beyond the halo boundary. As result, without accurate modelling of environmental processes for all galaxies, it is not possible to robustly reproduce the properties of galaxies which reside in different environments.

Semi-analytical models are the best way to rapidly compute physically-based galaxy formation models, which are very much needed in cosmology, allowing, in particular, to vary physical prescriptions and cosmology and reliably find the impact these have on galaxy properties. In Chapter 2, we perform a comparison, object-by-object and statistically, between the Munich semi-analytical model, L-GALAXIES, and the IllustrisTNG hydrodynamical simulations. Analyzing the properties of galaxies in different environments we find that:

- The gas content and star formation rates of galaxies in and around clusters and groups differ substantially between the two models, with IllustrisTNG satellites less star-forming and less gas-rich.

- Environmental processes such as ram-pressure stripping are stronger and operate to larger distances and for a broader host mass range in IllustrisTNG.

- Therefore, the treatment of galaxy evolution in the semi-analytic model needs to be improved by prescriptions which capture local environmental effects more accurately.

In Chapter 3, we introduce a Local Background Environment (LBE) estimator that can be measured in and around every galaxy or its dark matter subhalo in high-resolution cosmological simulations. The LBE is designed to capture the influence of environmental effects such as ram-pressure stripping on the formation and evolution of galaxies in semi-analytical models. We define the LBE directly from the particle data within an adaptive spherical shell, and devise a Gaussian mixture estimator to separate background particles from previously unidentified subhalo particles. Analyzing the LBE properties, we find that:

- The LBE of satellite galaxies is not at rest with respect to their host halo, in contrast to typical assumptions.

- The orientations of the velocities of a subhalo and its LBE are well aligned in the outer infall regions of haloes, but decorrelated near halo center.

- Significantly, there is no abrupt change in LBE velocity or density at the halo virial radius. This suggests that stripping should also happen beyond this radius.

We use the time-evolving LBE of galaxies to formulate a more accurate treatment of ram-pressure stripping for all galaxies within the Munich semi-analytical galaxy formation model, L-Galaxies. We note that this is the first time that actual local measurements are directly employed to capture environmental processes in semi-analytical models. In Chapter 4, we fully recalibrate the updated model using a Markov Chain Monte Carlo (MCMC) method with the stellar mass function and quenched fraction of galaxies at $0 \leq z \leq 2$ as observational constraints. Running the updated model, we produce hundreds of millions of galaxies at different redshifts. On the observational side, we undertake a new analysis of the SDSS galaxy data inferring the fraction of quenched galaxies versus halocentric distance. Analysing the results of our new model and the standard model on which it is based (Henriques et al. 2020), and also comparing mock catalogues of the updated model with SDSS and HSC observations, we find that:

- Galaxies in the vicinity of massive halos in the updated model are much less gas rich and less star forming. By measuring the actual amount of stripped gas in our model, we discover that these galaxies lose a large fraction of their hot halo gas prior to infall, when they are central galaxies.

- In the vicinity of massive and intermediate-mass halos at $z = 0$, the updated model produces more quenched galaxies and stronger environmental dependencies than the previous model, better recovering observed trends with halocentric distance (SDSS) up to several virial radii.

- At higher redshifts, $0.4 \leq z \leq 1$, our model is in relatively good agreement with observations from the HSC survey, while quantitative differences remain, particularly within the R_{200} of clusters.

The remaining tensions with data motivate two possible future model improvements: (i) stripping of the cold, star-forming gas discs in galaxies, and (ii) handling the ejection and re-distribution of gas in the (sub)halo due to baryonic feedback processes. Our method for incorporating the local background environment of galaxies can be naturally extended to handle cold gas stripping at smaller scales. At the same time, we have shown that the impact of environment on galaxy properties extends to much larger scales than the often assumed halo virial radius, and that related effects are also present in cosmological hydrodynamical simulations. Model improvements, incorporating insights from the use of our local environmental measurements in hydrodynamical simulations will be ideally suited to reveal the links between the physics of galaxy evolution and large scale correlations (e.g. two point correlation function of galaxies of different colour). Complex questions such as the physics behind the galactic conformity, the observed large-scale correlation between the star formation of neighbouring galaxies (Weinmann et al. 2006; Kauffmann et al. 2013), will be interesting avenues of further investigation using our new model.

Appendix A

Deriving the halo mass from stellar mass

The total halo mass, M_{200}, is not observable and is usually estimated using other well-defined observables. As explained in §4.3.2, we derive the halo mass from the stellar mass of each halo's central galaxy to make mock catalogues comparable with observations. Comparing these mock halo masses with their actual values from the simulation, we here explore the resulting scatter.

Fig. A.1 shows the direct simulation halo mass from the Millennium simulation as a function of the stellar mass of the central galaxy in our model (orange) and H20 (blue). The solid lines denote the median values and the light and dark shaded regions correspond to the 1σ and 2σ scatter of the distribution. The black line shows our best fit, which is in good agreement with our model (orange line) based on which the fitting is performed.

Additionally, Fig. A.2 shows the fit halo mass from Eq. 4.3 (y-axis) as a function of the direct simulation halo mass (x-axis) in our model and H20. The two halo masses (fit and model) are in rather close agreement with the 1σ scatter of 0.2-0.3 dex. The H20 is a bit off near $M_{200}/\mathrm{M}_\odot \sim 10^{13}$, which reflects different stellar mass to halo mass relationships in our model and H20. In this work, whenever we needed to convert stellar mass to halo mass, we used the fit based on our model (see §4.3.2).

Although this scatter is likely smaller than the typical error on stellar mass estimates from observations, its impact on the virial radius, R_{200}, could be substantial. For instance, if the mock halo mass is 0.3 dex larger/smaller than the true halo mass, this leads to the mock virial radius being $\sim 20-25\%$ larger/smaller than the true virial radius. As a result, in our comparison with observations, where we report results as a function of halocentric distance (Figs. 4.10 and 4.15), the trends with distance could contain $20-25\%$ error.
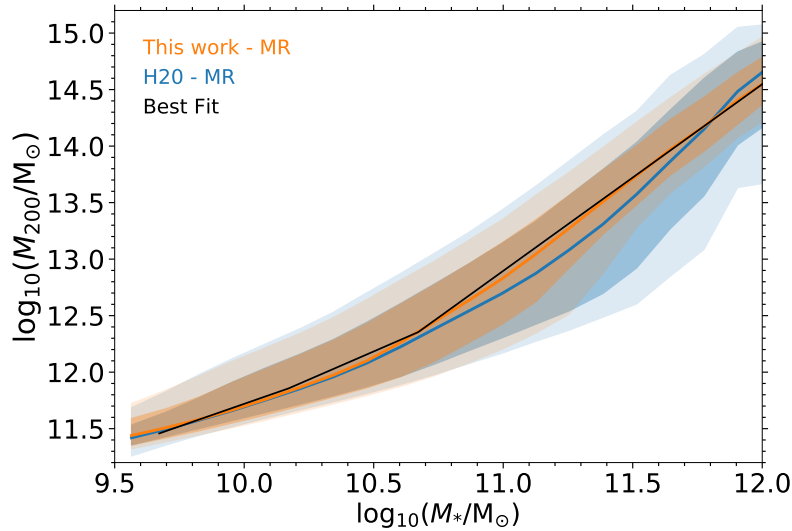
Figure A.1: Halo mass as a function of stellar mass in this work (orange) and in H20 (blue). The solid black line shows our best fit using L-Galaxies (this work) to the halo mass, as given in Eq. 4.3. The orange and blue solid lines correspond to the median values and the shaded regions illustrate 1σ and 2σ of the distribution. Our best fit (black line) is very close to the median value from the simulation (orange line), but slightly differs from the median line of the other model (H20).
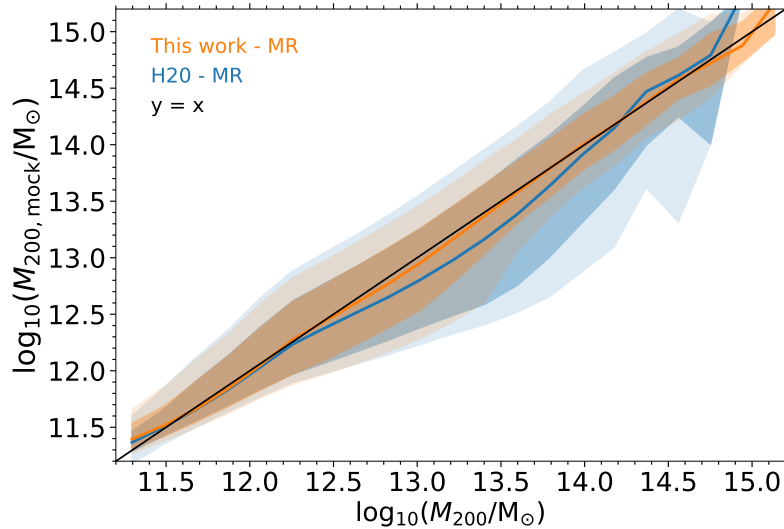
Figure A.2: The halo mass calculated using the stellar mass (Eq. 4.3) as a function of the halo mass measured directly from the Millennium simulation. The solid lines correspond to the median values and the shaded regions illustrate 1σ and 2σ of the distribution. The 1σ scatter around $y = x$ line is $\sim$ 0.2-0.3 dex, and the 2σ scatter is up to 0.5-0.6 dex.

Bibliography

Abazajian K. N., et al., 2009, ApJS, 182, 543

Ade P. A., et al., 2014, Astronomy & Astrophysics, 571, A16

Adhikari S., Dalal N., Chamberlain R. T., 2014, Journal of Cosmology and Astroparticle Physics, 2014, 019

Aghanim N., et al., 2018, arXiv preprint arXiv:1807.06209

Aihara H., et al., 2018, PASJ, 70, S4

Anderson M. E., Gaspari M., White S. D. M., Wang W., Dai X., 2015, MNRAS, 449, 3806

Angulo R. E., Hilbert S., 2015, Monthly Notices of the Royal Astronomical Society, 448, 364

Angulo R. E., White S. D., 2010, Monthly Notices of the Royal Astronomical Society, 405, 143

Angulo R. E., Springel V., White S. D. M., Jenkins A., Baugh C. M., Frenk C. S., 2012, MNRAS, 426, 2046

Aragon-Calvo M. A., Neyrinck M. C., Silk J., 2016, arXiv e-prints, (arXiv:1607.07881)

Avila-Reese V., Firmani C., Hernández X., 1998, ApJ, 505, 37

Ayromlou M., Nelson D., Yates R. M., Kauffmann G., White S. D. M., 2019, MNRAS, 487, 4313

Ayromlou M., Nelson D., Yates R. M., Kauffmann G., Renneby M., White S. D. M., 2021a, MNRAS, 502, 1051

Ayromlou M., Kauffmann G., Yates R. M., Nelson D., White S. D. M., 2021b, MNRAS, 505, 492

Bahé Y. M., McCarthy I. G., Crain R. A., Theuns T., 2012, Monthly Notices of the Royal Astronomical Society, 424, 1179

Bahé Y. M., Schaye J., Crain R. A., McCarthy I. G., Bower R. G., Theuns T., McGee S. L., Trayford J. W., 2017, MNRAS, 464, 508

Baldry I. K., Glazebrook K., Brinkmann J., Ivezić Ž., Lupton R. H., Nichol R. C., Szalay A. S., 2004, ApJ, 600, 681

Baldry I., Glazebrook K., Driver S., 2008, Monthly Notices of the Royal Astronomical Society, 388, 945

Baldry I. K., et al., 2012, Monthly Notices of the Royal Astronomical Society, 421, 621

Balogh M. L., Morris S. L., Yee H., Carlberg R., Ellingson E., 1999, The Astrophysical Journal, 527, 54

Bekki K., 2009, MNRAS, 399, 2221

Bell E. F., McIntosh D. H., Katz N., Weinberg M. D., 2003, ApJS, 149, 289

Bernardi M., Meert A., Sheth R., Vikram V., Huertas-Company M., Mei S., Shankar F., 2013, Monthly Notices of the Royal Astronomical Society, 436, 697

Bertone S., De Lucia G., Thomas P. A., 2007, Monthly Notices of the Royal Astronomical Society, 379, 1143

Binney J., Tremaine S., 1987, Galactic Dynamics, Princeton Univ

Birnboim Y., Dekel A., 2003, MNRAS, 345, 349

Bond J. R., Cole S., Efstathiou G., Kaiser N., 1991, ApJ, 379, 440

Boselli A., Gavazzi G., 2006, PASP, 118, 517

Boselli A., et al., 2016, A&A, 596, A11

Boselli A., et al., 2018, A&A, 614, A56

Bouwens R. J., et al., 2012, ApJ, 754, 83

Boylan-Kolchin M., Springel V., White S. D., Jenkins A., Lemson G., 2009, Monthly Notices of the Royal Astronomical Society, 398, 1150

Bravo M., Lagos C. d. P., Robotham A. S. G., Bellstedt S., Obreschkow D., 2020, MNRAS, 497, 3026

Brinchmann J., Charlot S., White S. D. M., Tremonti C., Kauffmann G., Heckman T., Brinkmann J., 2004, MNRAS, 351, 1151

Bryan G. L., et al., 2014, ApJS, 211, 19

Chabrier G., 2003, PASP, 115, 763

Chiu I., et al., 2018, Monthly Notices of the Royal Astronomical Society, 478, 3072

Cole S., Lacey C. G., Baugh C. M., Frenk C. S., 2000, Monthly Notices of the Royal Astronomical Society, 319, 168

Cora S. A., et al., 2018, Monthly Notices of the Royal Astronomical Society

Crain R. A., et al., 2015, MNRAS, 450, 1937

Croton D. J., et al., 2006, Monthly Notices of the Royal Astronomical Society, 365, 11

Croton D. J., et al., 2016, The Astrophysical Journal Supplement Series, 222, 22

D'Souza R., Vegetti S., Kauffmann G., 2015, Monthly Notices of the Royal Astronomical Society, 454, 4027

Dalcanton J. J., Spergel D. N., Summers F. J., 1997, ApJ, 482, 659

Davé R., Rafieferantsoa M. H., Thompson R. J., Hopkins P. F., 2017, MNRAS, 467, 115

David L. P., Jones C., Forman W., Vargas I. M., Nulsen P., 2006, The Astrophysical Journal, 653, 207

Davies L. J. M., et al., 2019, MNRAS, 483, 5444

Davies J. J., Crain R. A., Oppenheimer B. D., Schaye J., 2020, MNRAS, 491, 4462

Davis M., Efstathiou G., Frenk C. S., White S. D. M., 1985, ApJ, 292, 371

De Lucia G., Kauffmann G., Springel V., White S. D. M., Lanzoni B., Stoehr F., Tormen G., Yoshida N., 2004, MNRAS, 348, 333

De Lucia G., Springel V., White S. D., Croton D., Kauffmann G., 2006, Monthly Notices of the Royal Astronomical Society, 366, 499

Diemer B., Kravtsov A. V., 2014, The Astrophysical Journal, 789, 1

Diemer B., et al., 2019, MNRAS, 487, 1529

Domínguez Sánchez H., et al., 2011, Monthly Notices of the Royal Astronomical Society, 417, 900

Donnari M., et al., 2019, MNRAS, 485, 4817

Donnari M., et al., 2020a, MNRAS,

Donnari M., Pillepich A., Nelson D., Marinacci F., Vogelsberger M., Hernquist L., 2020b, arXiv e-prints, p. arXiv:2008.00004 (arXiv:2008.00004)

Dressler A., 1980, The Astrophysical Journal, 236, 351

Driver S. P., et al., 2018, MNRAS, 475, 2891

Dutton A. A., 2009, MNRAS, 396, 121

Efstathiou G., 1992, MNRAS, 256, 43P

Elbaz D., et al., 2007, Astronomy & Astrophysics, 468, 33

Font A. S., et al., 2008, Monthly Notices of the Royal Astronomical Society, 389, 1619

Forcada-Miro M. I., White S. D. M., 1997, arXiv e-prints,

Fu J., Hou J. L., Yin J., Chang R. X., 2009, ApJ, 696, 668

Fu J., Guo Q., Kauffmann G., Krumholz M. R., 2010, MNRAS, 409, 515

Fu J., Kauffmann G., Li C., Guo Q., 2012, MNRAS, 424, 2701

Fu J., et al., 2013, MNRAS, 434, 1531

Genel S., et al., 2014, Monthly Notices of the Royal Astronomical Society, 445, 175

Genzel R., Tacconi L. J., Lutz D., et al., 2015, ApJ, 800, 20

Giodini S., et al., 2009, The Astrophysical Journal, 703, 982

Gladders M. D., Yee H. K. C., 2000, AJ, 120, 2148

Gladders M. D., Yee H. K. C., 2005, ApJS, 157, 1

Gnedin N. Y., 2000, ApJ, 542, 535

Gonzalez-Perez V., Lacey C. G., Baugh C. M., Lagos C. D. P., Helly J., Campbell D. J. R., Mitchell P. D., 2014, MNRAS, 439, 264

Gonzalez A. H., Sivanandam S., Zabludoff A. I., Zaritsky D., 2013, The Astrophysical Journal, 778, 14

Gottlöber S., Yepes G., 2007, ApJ, 664, 117

Gunn J. E., Gott J. Richard I., 1972, ApJ, 176, 1

Guo Q., et al., 2011, Monthly Notices of the Royal Astronomical Society, 413, 101

Guo Q., White S., Angulo R. E., Henriques B., Lemson G., Boylan-Kolchin M., Thomas P., Short C., 2013, MNRAS, 428, 1351

Guo Q., et al., 2016, MNRAS, 461, 3457

Hansen S. M., Sheldon E. S., Wechsler R. H., Koester B. P., 2009, The Astrophysical Journal, 699, 1333

Hastings W. K., 1970, Biometrika, 57, 97

Hatfield P., Jarvis M., 2017, Monthly Notices of the Royal Astronomical Society, 472, 3570

Haynes M. P., et al., 2011, AJ, 142, 170

Hearin A. P., Behroozi P. S., van den Bosch F. C., 2016, Monthly Notices of the Royal Astronomical Society, 461, 2135

Helly J. C., Cole S., Frenk C. S., Baugh C. M., Benson A., Lacey C., Pearce F. R., 2003, MNRAS, 338, 913

Henriques B. M. B., Thomas P. A., Oliver S., Roseboom I., 2009, MNRAS, 396, 535

Henriques B. M. B., White S. D. M., Thomas P. A., Angulo R. E., Guo Q., Lemson G., Springel V., 2013, MNRAS, 431, 3373

Henriques B. M., White S. D., Thomas P. A., Angulo R., Guo Q., Lemson G., Springel V., Overzier R., 2015, Monthly Notices of the Royal Astronomical Society, 451, 2663

Henriques B. M. B., White S. D. M., Thomas P. A., Angulo R. E., Guo Q., Lemson G., Wang W., 2017, MNRAS, 469, 2626

Henriques B. M. B., Yates R. M., Fu J., Guo Q., Kauffmann G., Srisawat C., Thomas P. A., White S. D. M., 2020, MNRAS, 491, 5795

Hernquist L., Katz N., 1989, ApJS, 70, 419

Hopkins P. F., 2015, MNRAS, 450, 53

Hubble E., Humason M. L., 1931, The Astrophysical Journal, 74, 43

Ilbert O., et al., 2010, The Astrophysical Journal, 709, 644

Ilbert O., et al., 2013, Astronomy & Astrophysics, 556, A55

Jaffé Y. L., Smith R., Candlish G. N., Poggianti B. M., Sheen Y.-K., Verheijen M. A. W., 2015, MNRAS, 448, 1715

Jones M. G., Haynes M. P., Giovanelli R., Moorman C., 2018, MNRAS, 477, 2

Joshi G. D., Pillepich A., Nelson D., Marinacci F., Springel V., Rodriguez-Gomez V., Vogelsberger M., Hernquist L., 2020, MNRAS, 496, 2673

Kauffmann G., 1996, MNRAS, 281, 475

Kauffmann G., 2015, Monthly Notices of the Royal Astronomical Society, 454, 1840

Kauffmann G., White S. D., Guiderdoni B., 1993, Monthly Notices of the Royal Astronomical Society, 264, 201

Kauffmann G., Colberg J. M., Diaferio A., White S. D., 1999, Monthly Notices of the Royal Astronomical Society, 303, 188

Kauffmann G., et al., 2003, MNRAS, 341, 33

Kauffmann G., White S. D., Heckman T. M., Ménard B., Brinchmann J., Charlot S., Tremonti C., Brinkmann J., 2004, Monthly Notices of the Royal Astronomical Society, 353, 713

Kauffmann G., Li C., Zhang W., Weinmann S., 2013, Monthly Notices of the Royal Astronomical Society, 430, 1447

Klypin A. A., Trujillo-Gomez S., Primack J., 2011, ApJ, 740, 102

Komatsu E., et al., 2011, The Astrophysical Journal Supplement Series, 192, 18

Kraljic K., et al., 2018, MNRAS, 474, 547

Kravtsov A., Vikhlinin A., Meshcheryakov A., 2018, Astronomy Letters, 44, 8

Krumholz M. R., McKee C. F., Tumlinson J., 2009, ApJ, 693, 216

Lacey C. G., et al., 2016, Monthly Notices of the Royal Astronomical Society, 462, 3854

Lagos C. d. P., Tobar R. J., Robotham A. S., Obreschkow D., Mitchell P. D., Power C., Elahi P. J., 2018, Monthly Notices of the Royal Astronomical Society, 481, 3573

Larson R. B., Tinsley B. M., Caldwell C. N., 1980, ApJ, 237, 692

Li C., White S. D., 2009, Monthly Notices of the Royal Astronomical Society, 398, 2177

Lim S. H., Mo H. J., Li R., Liu Y., Ma Y.-Z., Wang H., Yang X., 2018, ApJ, 854, 181

Lim S. H., Barnes D., Vogelsberger M., Mo H. J., Nelson D., Pillepich A., Dolag K., Marinacci F., 2020a, arXiv e-prints, p. arXiv:2007.11583 (arXiv:2007.11583)

Lim S., Mo H., Wang H., Yang X., 2020b, The Astrophysical Journal, 889, 48

Lovisari L., Reiprich T., Schellenberger G., 2015, Astronomy & Astrophysics, 573, A118

Lu T., Gilbank D. G., McGee S. L., Balogh M. L., Gallagher S., 2012, Monthly Notices of the Royal Astronomical Society, 420, 126

Luo Y., Kang X., Kauffmann G., Fu J., 2016, MNRAS, 458, 366

Marchesini D., Van Dokkum P. G., Schreiber N. M. F., Franx M., Labbé I., Wuyts S., 2009, The Astrophysical Journal, 701, 1765

Marchesini D., et al., 2010, The Astrophysical Journal, 725, 1277

Marinacci F., et al., 2018, Monthly Notices of the Royal Astronomical Society, 480, 5113

Martis N. S., et al., 2016, ApJ, 827, L25

McCarthy I. G., Frenk C. S., Font A. S., Lacey C. G., Bower R. G., Mitchell N. L., Balogh M. L., Theuns T., 2008, MNRAS, 383, 593

McKee C. F., Krumholz M. R., 2010, ApJ, 709, 308

Metropolis N., Rosenbluth A., Rosenbluth M., Teller A., Teller E., 1953, J. Chem. Phys., 21, 1087

Mitchell P. D., et al., 2018, MNRAS, 474, 492

Mo H. J., Mao S., White S. D. M., 1998, MNRAS, 295, 319

Mo H., Van den Bosch F., White S., 2010, Galaxy formation and evolution. Cambridge University Press

More S., Diemer B., Kravtsov A. V., 2015, The Astrophysical Journal, 810, 36

Mosleh M., Tavasoli S., Tacchella S., 2018, ApJ, 861, 101

Moster B. P., Somerville R. S., Maulbetsch C., van den Bosch F. C., Macciò A. V., Naab T., Oser L., 2010, ApJ, 710, 903

Muzzin A., Wilson G., Lacy M., Yee H. K. C., Stanford S. A., 2008, ApJ, 686, 966

Muzzin A., et al., 2009, ApJ, 698, 1934

Muzzin A., et al., 2013, The Astrophysical Journal, 777, 18

Naiman J. P., et al., 2018, Monthly Notices of the Royal Astronomical Society, 477, 1206

Nelson D., et al., 2015, Astronomy and Computing, 13, 12

Nelson D., Genel S., Pillepich A., Vogelsberger M., Springel V., Hernquist L., 2016, MN-RAS, 460, 2881

Nelson D., et al., 2018, MNRAS, 475, 624

Nelson D., et al., 2019a, Computational Astrophysics and Cosmology, 6, 2

Nelson D., et al., 2019b, MNRAS, 490, 3234

Noeske K. G., et al., 2007, ApJ, 660, L43

Oemler A., 1974, PhD thesis, California Institute of Technology

Okamoto T., Gao L., Theuns T., 2008, MNRAS, 390, 920

Oman K. A., Bahé Y. M., Healy J., Hess K. M., Hudson M. J., Verheijen M. A. W., 2020, arXiv e-prints, p. arXiv:2009.00667 (arXiv:2009.00667)

Oppenheimer B. D., 2018, Monthly Notices of the Royal Astronomical Society, 480, 2963

Oppenheimer B. D., Davé R., 2008, MNRAS, 387, 577

Oppenheimer B. D., Davé R., Kereš D., Fardal M., Katz N., Kollmeier J. A., Weinberg D. H., 2010, MNRAS, 406, 2325

Pakmor R., Springel V., 2013, Monthly Notices of the Royal Astronomical Society, 432, 176

Pakmor R., Bauer A., Springel V., 2011, Monthly Notices of the Royal Astronomical Society, 418, 1392

Pallero D., Gómez F. A., Padilla N. D., Torres-Flores S., Demarco R., Cerulo P., Olave-Rojas D., 2019, MNRAS, 488, 847

Peng Y.-j., et al., 2010, ApJ, 721, 193

Pilkington K., Few C. G., Gibson B. K., et al., 2012, A&A, 540, A56

Pillepich A., et al., 2018a, Monthly Notices of the Royal Astronomical Society, 473, 4077

Pillepich A., et al., 2018b, Monthly Notices of the Royal Astronomical Society, 475, 648

Pillepich A., et al., 2019, Monthly Notices of the Royal Astronomical Society, 490, 3196

Pintos-Castro I., Yee H. K. C., Muzzin A., Old L., Wilson G., 2019, ApJ, 876, 40

Planck Collaboration 2016, A&A, 594, A13

Planck Collaboration et al., 2018, arXiv e-prints, p. arXiv:1807.06209 (arXiv:1807.06209)

Poggianti B. M., et al., 2017, ApJ, 844, 48

Press W. H., Schechter P., 1974, ApJ, 187, 425

Renneby M., Henriques B. M. B., Hilbert S., Nelson D., Vogelsberger M., Angulo R. E., Springel V., Hernquist L., 2020, MNRAS, 498, 5804

Riebe K., et al., 2011, arXiv e-prints, p. arXiv:1109.0003 (arXiv:1109.0003)

Roediger E., Brüggen M., 2007, MNRAS, 380, 1399

Sales L. V., et al., 2015, MNRAS, 447, L6

Salim S., et al., 2007, ApJS, 173, 267

Sanderson A. J., O'Sullivan E., Ponman T. J., Gonzalez A. H., Sivanandam S., Zabludoff A. I., Zaritsky D., 2013, Monthly Notices of the Royal Astronomical Society, 429, 3288

Saro A., De Lucia G., Borgani S., Dolag K., 2010, MNRAS, 406, 729

Sarron F., Adami C., Durret F., Laigle C., 2019, A&A, 632, A49

Schaye J., et al., 2015, MNRAS, 446, 521

Scoville N., Lee N., Vanden Bout P., et al., 2017, ApJ, 837, 150

Sheth R. K., Mo H. J., Tormen G., 2001, MNRAS, 323, 1

Simpson C. M., Grand R. J., Gómez F. A., Marinacci F., Pakmor R., Springel V., Campbell D. J., Frenk C. S., 2018, Monthly Notices of the Royal Astronomical Society, 478, 548

Singh P., Majumdar S., Nath B. B., Silk J., 2018, MNRAS, 478, 2909

Skillman S. W., Warren M. S., Turk M. J., Wechsler R. H., Holz D. E., Sutter P. M., 2014, arXiv e-prints, p. arXiv:1407.2600 (`arXiv:1407.2600`)

Somerville R. S., Primack J. R., 1999, Monthly Notices of the Royal Astronomical Society, 310, 1087

Somerville R. S., Primack J. R., Faber S. M., 2001, MNRAS, 320, 504

Spergel D. N., et al., 2003, The Astrophysical Journal Supplement Series, 148, 175

Springel V., 2005, MNRAS, 364, 1105

Springel V., 2010, Monthly Notices of the Royal Astronomical Society, 401, 791

Springel V., Yoshida N., White S. D. M., 2001a, New˜Astron., 6, 79

Springel V., White S. D., Tormen G., Kauffmann G., 2001b, Monthly Notices of the Royal Astronomical Society, 328, 726

Springel V., et al., 2005, nature, 435, 629

Springel V., et al., 2018, Monthly Notices of the Royal Astronomical Society, 475, 676

Stevens A. R., Croton D. J., Mutch S. J., 2016a, Monthly Notices of the Royal Astronomical Society, 461, 859

Stevens A. R. H., Croton D. J., Mutch S. J., 2016b, MNRAS, 461, 859

Stevens A. R. H., et al., 2019, MNRAS, 483, 5334

Stringer M. J., Benson A. J., 2007, MNRAS, 382, 641

Sunyaev R., Zeldovich Y. B., 1972, Comments on Astrophysics and Space Physics, 4, 173

Sutherland R. S., Dopita M. A., 1993, ApJS, 88, 253

Tavasoli S., Vasei K., Mohayaee R., 2013, A&A, 553, A15

Tecce T. E., Cora S. A., Tissera P. B., Abadi M. G., Lagos C. d. P., 2010, Monthly Notices of the Royal Astronomical Society, 408, 2008

Terrazas B. A., et al., 2020, MNRAS, 493, 1888

Teyssier R., 2002, A&A, 385, 337

Tinker J. L., 2020, arXiv e-prints, p. arXiv:2007.12200 (`arXiv:2007.12200`)

Tomczak A. R., et al., 2014, The Astrophysical Journal, 783, 85

Tonnesen S., Bryan G. L., 2009, ApJ, 694, 789

Torrey P., Vogelsberger M., Genel S., Sijacki D., Springel V., Hernquist L., 2014, Monthly Notices of the Royal Astronomical Society, 438, 1985

Trayford J. W., Theuns T., Bower R. G., Crain R. A., Lagos C. d. P., Schaller M., Schaye J., 2016, MNRAS, 460, 3925

Treyer M., et al., 2018, Monthly Notices of the Royal Astronomical Society, 477, 2684

Truong N., et al., 2020, MNRAS,

Vijayaraghavan R., Ricker P. M., 2017, ApJ, 841, 38

Vogelsberger M., Genel S., Sijacki D., Torrey P., Springel V., Hernquist L., 2013, MNRAS, 436, 3031

Vogelsberger M., et al., 2014, Monthly Notices of the Royal Astronomical Society, 444, 1518

Wadsley J. W., Keller B. W., Quinn T. R., 2017, MNRAS, 471, 2357

Wang W., Sales L. V., Henriques B. M. B., White S. D. M., 2014, MNRAS, 442, 1363

Wang E., Wang H., Mo H., van den Bosch F. C., Lim S. H., Wang L., Yang X., Chen S., 2018a, ApJ, 864, 51

Wang Y., et al., 2018b, ApJ, 868, 130

Wang L., Xu D., Gao L., Guo Q., Qu Y., Pan J., 2019, MNRAS, 485, 2083

Wang J., Xu W., Lee B., Du M., Overzier R., Shao L., 2020a, arXiv e-prints, p. arXiv:2009.08159 (arXiv:2009.08159)

Wang J., Bose S., Frenk C. S., Gao L., Jenkins A., Springel V., White S. D. M., 2020b, Nature, 585, 39

Webb K., et al., 2020, MNRAS, 498, 5317

Weinberger R., et al., 2017, MNRAS, 465, 3291

Weinberger R., et al., 2018, MNRAS, 479, 4056

Weinmann S. M., Van Den Bosch F. C., Yang X., Mo H., 2006, Monthly Notices of the Royal Astronomical Society, 366, 2

Wetzel A. R., Tinker J. L., Conroy C., 2012, MNRAS, 424, 232

Wetzel A. R., Tinker J. L., Conroy C., van den Bosch F. C., 2014, MNRAS, 439, 2687

White S. D. M., 1989, in Frenk C. S., sEllis R. S., Shanks T., Heavens A. R., Peacock J. A., eds, NATO ASIC Proc. 264: The Epoch of Galaxy Formation. p. 15

White S. D. M., Frenk C. S., 1991, ApJ, 379, 52

White S. D. M., Rees M. J., 1978, MNRAS, 183, 341

Wilson G., et al., 2009, ApJ, 698, 1943

Yan H., Fan Z., White S. D. M., 2013, MNRAS, 430, 3432

Yang X., Mo H. J., van den Bosch F. C., 2003, MNRAS, 339, 1057

Yang X., Mo H. J., van den Bosch F. C., Jing Y. P., 2005, MNRAS, 356, 1293

Yang X., Mo H. J., van den Bosch F. C., Pasquali A., Li C., Barden M., 2007, ApJ, 671, 153

Yates R. M., Henriques B., Thomas P. A., Kauffmann G., Johansson J., White S. D., 2013, Monthly Notices of the Royal Astronomical Society, 435, 3500

Yates R. M., Thomas P. A., Henriques B. M. B., 2017, MNRAS, 464, 3169

Yoshida N., Stoehr F., Springel V., White S. D. M., 2002, MNRAS, 335, 762

Yun K., et al., 2019, MNRAS, 483, 1042

Zinger E., Dekel A., Kravtsov A. V., Nagai D., 2018, Monthly Notices of the Royal Astronomical Society, 475, 3654

Zinger E., et al., 2020, arXiv e-prints, p. arXiv:2004.06132 (arXiv:2004.06132)

Zwaan M. A., Meyer M. J., Staveley-Smith L., Webster R. L., 2005, MNRAS, 359, L30

von der Linden A., Wild V., Kauffmann G., White S. D., Weinmann S., 2010, Monthly Notices of the Royal Astronomical Society, 404, 1231

Acknowledgements

My 8th-grade science teacher, Mr. Naseri, taught us physics so beautifully that it motivated me to explore physics throughout my life. You have my special thanks, Mr. Naseri. Later, as a bachelor's student in physics, I became unsure if I wanted to pursue a career in physics. Contemplating my options in depth, I realized that becoming a physicist was the only path for me, which leaves no regrets in the future. This is where my real journey in physics started. This journey is now at the stage in which I am receiving my Ph.D. from one of the most prestigious institutions in the world. Of course, neither is this the end of the journey nor is there an end to it. Nevertheless, perhaps now is an opportune moment to express my appreciation for the people who have helped me reach this stage.

Firstly, I would like to thank my supervisors, Guinevere Kauffmann and Simon White, for giving me the opportunity to study at the MPA and for their continuous support and advice. Guinevere and Simon, among all the things I have learned from you, the scientific thinking style is the most precious and I am very grateful for that.

My special thanks to Dylan Nelson and Rob Yates, who were not only great advisors but also very good friends, supporting me at all stages of my Ph.D. at the MPA. Thank you for your support, including your advice and your relentless patience.

Furthermore, I would like to thank Eiichiro Komatsu for his support and helpful advice as a member of my thesis committee. I also thank Bruno Henriques for the valuable discussions that benefited my research. In addition, I want to thank the members of my Ph.D. thesis examination committee, Guinevere Kauffmann, Joseph Mohr, Volker Springel, and Jörg Schreiber, for agreeing to be on the examination committee and for very useful discussions during my defense session.

At the MPA, I had the opportunity to learn from several people. I appreciate the many fruitful discussions with Volker Springel, Thorsten Naab, Rüdiger Pakmor, and the other members of the galaxy formation and computational astrophysics groups. I am thankful for all our chats on the Wednesday Galaxy Group Meetings and during lunchtime.

Moreover, I want to thank the MPA secretaries Gabriele Kratschmann and Maria Depner for their constant willingness to help. Gabi and Maria, you went beyond your duty without hesitation to help and support me. This kindness will not be forgotten. I also thank Cornelia Rickl, Sonja Gründl, Annette Hilbert, Hannelore Hämmerle, and Mirna Balicevic for their consistent support.

Furthermore, I want to thank Andreas Weiss and Goran Toth for always being helpful and keeping the computers running. Additionally, thanks to those people at the MPA and